Optical and Semiconductor Devices Group

Department of Electrical and Electronic Engineering

Imperial College London

Real-Time Control of 2D Lissajous Fibre Scanners and Multi-Wavelength Scanning System

Author: Qiyu Xiong

Supervised by: Prof. Oleksiy Sydoruk and Prof. Richard R. A. Syms

A thesis submitted for the degree of

Doctor of Philosophy

December 2025

Abstract

The design, control, and setup of the two-dimensional (2D) Lissajous fibre scanners were investigated, with focus on real-time control and multi-wavelength operation. The first contribution is a dynamically programmable real-time controller for 2D Lissajous scanning. A dual-core cantilever is fabricated by dip-coating two cylindrical single-mode fibres to obtain two orthogonal bending modes with a frequency ratio close to 2. The cantilever is driven by a single piezoelectric actuator at 45°, and backscattered light is captured through cladding mode detection in a dual numerical aperture confocal scheme. Optical feedback is provided by an amplitude-coded reflecting aperture, allowing low- and high-mode timing pulses to be separated using window detectors. The low-frequency mode is locked to resonance using a phase-locked loop (PLL), while the high mode is driven off-resonance using a voltage-controlled oscillator. Additional PLLs, voltage-controlled phase shifters, and divide-by-N circuits correct amplitude imbalance and synchronise the phases, enabling programmable generation of Lissajous figures with variable scan density. This represents the first demonstration of real-time, dynamically reconfigurable Lissajous scan using intermittent feedback alone. Based on this platform, the second contribution introduces a broadband Lissajous scanner based on photonic crystal fibres (PCFs) and multi-wavelength mode-stripping detection. PCFs are dip-coated in polymer using an additional sealed-tip process to maintain the air holes. Mode-stripping detection is characterised using a monochromator and RGB photodiodes, enabling efficient multi-wavelength operation. A PCF-based scanner is constructed using RGB laser sources, with a colour-coded aperture providing distinguishable feedback for real-time control under both blue-only and multiplexed white-light illumination. The system demonstrates fluorescence imaging of USAF test targets and biological samples, as well as calibrated full-colour imaging. Together, these results establish a compact, programmable, and broadband 2D fibre-scanning microscope capable of real-time operation. The combination of a real-time controller and multi-wavelength detection provides a pathway towards future miniature scanners with multispectral functionality.

Declaration of Originality

I declare that the research contained in this thesis is the product of my own work. The use of supporting literature by other authors has been clearly indicated and appropriately referenced. This work, or any part thereof, has not been previously submitted for any academic or professional qualification.

Qiyu Xiong

Declaration of Copyright

The copyright of this thesis rests with the author. Unless otherwise indicated, its contents are licensed under a Creative Commons Attribution-Non-Commercial 4.0 International Licence (CC BY-NC). Under this licence, you may copy and redistribute the material in any medium or format. You may also create and distribute modified versions of the work. This is on the condition that: you credit the author and do not use it, or any derivative works, for a commercial purpose. When reusing or sharing this work, ensure you make the licence terms clear to others by naming the licence and linking to the licence text. Where a work has been adapted, you should indicate that the work has been changed and describe those changes. Please seek permission from the copyright holder for uses of this work that are not included in this licence or permitted under UK Copyright Law.

Acknowledgement

I would like to thank my supervisors, Prof. Richard Syms and Prof. Oleksiy Sydoruk, for their guidance and help throughout my PhD.

I would like to thank my parents, my parents-in-law, and my sister for their support, both financially and emotionally. They provided everything I needed to pursue this PhD without having to worry about other things, and I could not have succeeded without them.

I would like to thank my wife, Mengxuan Chi, for being by my side. She supported me with all her heart and stayed with me through the toughest times. More importantly, when I felt lost about the direction of my life, she helped me find the meaning and the purpose. She gave me the courage and confidence to keep going.

Finally, I would like to thank all my colleagues and friends. We shared many ideas and always encouraged each other.

List of Publications

This thesis is supported by the following publications:

Q. Xiong, O. Sydoruk, R. R. A. Syms, "Dynamically programable real-time controller for a 2D scanning fibre microscope," Opt. Express 32, 46400-46414 (2024)

Q. Xiong, O. Sydoruk, R. R. A. Syms, "Multi-wavelength Lissajous fibre scanner using photonic crystal fibres," Opt. Express 33, 53117-53127 (2025)

Contents

Abstract ii

Declaration of Originality iii

Declaration of Copyright iv

Acknowledgement v

List of Publications vi

Chapter 1: Introduction 1

1.1 Fibre Dynamics 1
1.2 Imaging Optics 13
1.3 Tracking of Fibre Motion 19
1.4 Control Systems 21
1.5 Multi-wavelength Detection 25
1.6 Thesis Outline 28

Chapter 2: Fibre Dynamics and Open-Loop Analysis 31

2.1 Intermittent Feedback 31
2.2 Real-Time Control 33
2.2.1 1D Control 33
2.2.2 2D Control 37
2.3 Conclusion 52

Chapter 3: Real-Time Controller 54

3.1 Controller Design 54
3.2 Simulation Setup 58
3.3 Experimental Fibre Fabrication 62
3.4 Experiment Setup 67
3.5 Performance 76
3.6 Conclusion 82

Chapter 4: 2D Lissajous Fibre Scanning System 84

4.1 Scanning System Setup 84
4.2 Experimental Scan Lines 87
4.3 System Calibration 89
4.3.1 Setup Error 89
4.3.2 Controller Error 90
4.4 Image Reconstruction 93
4.4.1 Sampling 93
4.4.2 Transient and Steady-State Imaging 97
4.4.3 Other Samples 99
4.5 Conclusion 100

Chapter 5: Multi-Wavelength Lissajous Fibre Scanner using Photonic Crystal Fibres 101

5.1 Fibre Fabrication 101
5.1.1 Theoretical Resonant Frequency Ratio 102
5.1.2 Dip-Coating 104
5.2 Multi-wavelength Mode-Stripping Detection Measurement 107
5.3 Scanning System 110
5.3.1 Scanner Setup 110
5.4 Multi-Wavelength Image Reconstruction 114
5.4.1 Fluorescence Imaging 115
5.4.2 Full-Colour Imaging 117
5.5 Conclusion 120

Chapter 6: Summary and Future Work 121

6.1 Summary 121
6.2 Further Work 122

References 128

Chapter 1: Introduction

This thesis is concerned with developments in fibre-based optical scanning. This chapter introduces the dynamics of vibrating fibres for optical scanning, the theoretical principles underlying general and fibre-based imaging, and the challenges associated with tracking the fibre during operation. It also outlines the control theories relevant to real-time control for the fibre scanners and highlights the difficulties in achieving multi-wavelength detection in fibre-scanning systems.

1.1 Fibre Dynamics

This section introduces the main types of optical scanners and outlines the advantages of fibre-based designs. We then present the mechanical theory underlying Lissajous fibre scanners and highlight the benefits of Lissajous scanning patterns.

Optical Scanner Overview

Optical scanners are widely employed in microscopy [1-4], endoscopy [5-7], optical coherence tomography (OCT) [8-11], optical sensing [12-14], and display technologies [15-19], owing to their compact structure and versatile functionality. In these systems, an illumination beam is directed towards the target, and the backscattered or reflected light is collected and processed to extract imaging information. Scanning is achieved by introducing controlled motion into one or more optical components. Figure 1.1 shows typical optical scanners based on moving lenses [20-22], diffraction gratings [23], micro-fabricated scanning mirrors [24-26] or moving waveguides [27-31].

Optical scanners exploit a range of beam-steering mechanisms, each relying on a distinct physical principle. In Figure 1.1(a), a moving-lens scanner translates a lens relative to the light source, altering the alignment of the collimated beam and thereby changing its output direction. In Figure 1.1(b), a grating-based scanner uses the principle of diffraction: a microfabricated grating is oscillated or rotated to deflect the incident beam through different angles, producing a sweep across the field of view (FOV). In Figure 1.1(c), a scanning-mirror system uses a micro-electromechanical-

systems (MEMS) mirror that tilts on a micro-hinge, reflecting the beam in two dimensions as the mirror oscillates. Finally, in Figure 1.1(d), a moving waveguide (either in integrated optic or fibre optic form) uses the waveguide itself as the moving element. Here a flexible fibre cantilever is excited into vibration, causing its distal tip to swing and steer the emitted beam. In practice, the scanner types shown in Figure 1.1(a-c) typically require complex fabrication processes, precise assembly, and specialised actuation mechanisms, making them more costly and difficult to integrate. Fibre-based scanners, by contrast, are compact, lightweight, and inexpensive, as they use simple transducers to excite the fibres. These advantages have made fibre scanners the most widely adopted configurations for miniaturised imaging systems.

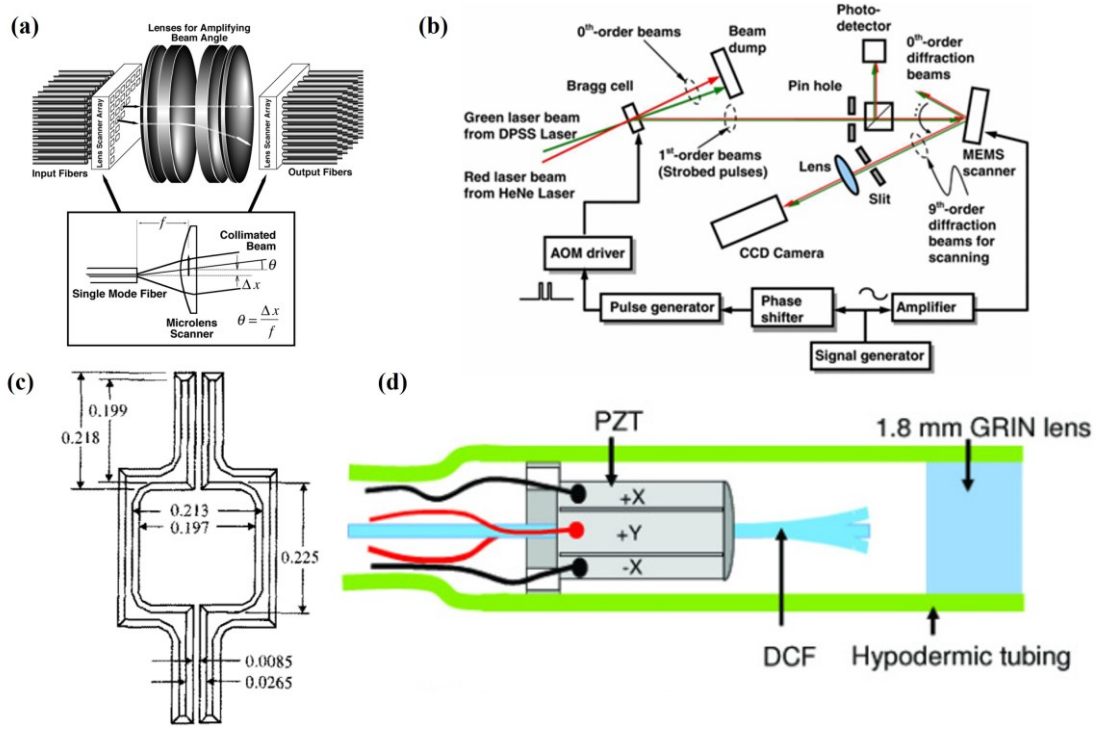


Fig. 1.1 Optical scanners based on (a) moving lens [22], (b) diffraction grating [23], (c) scanning mirror [24] and (d) moving waveguide [28].

General Mechanical Theory

We therefore start by reviewing the theory underlying the displacement of a vibrating beam. The Euler-Bernoulli equation describes the relationship between the beam's deflection and the applied load [32-33]. For a homogeneous beam, the governing equation can be derived from the Euler-Lagrange equation and written as:

$$EI\frac{\partial^4 W}{\partial x^4} = -\rho A\frac{\partial^2 W}{\partial x^2} + q(x) \tag{1.1}$$

where E, I, ρ and A denote the Young's modulus, second moment of area, density, and cross-sectional area of the beam, respectively. $W(x,t)$ is the transverse deflection of the beam in the z-direction at axial coordinate x and $q(x)$ is the external load. In the absence of external loading, Eqn. (1.1) reduces to the free-vibration equation. Its solution can be expressed using a Fourier decomposition of the form:

$$W(x,t) = Re\left[\widehat{W}(x)e^{-i\omega_n t}\right] \tag{1.2}$$

where ω_n are the natural frequencies of vibration. The general solution is:

$$\widehat{W} = A_1\cosh(\beta_n x) + A_2\sinh(\beta_n x) + A_3\cos(\beta_n x) + A_4\sin(\beta_n x) \tag{1.3}$$

where $A_{1,2,3,4}$ are constants and

$$\beta_n = \left(\frac{\rho A\omega_n^2}{EI}\right)^{\frac{1}{4}} \tag{1.4}$$

Each solution corresponds to a vibration mode, and the associated displacement function is referred to as the mode shape. When one end of the beam ($x = 0$) is fixed, the beam of length L forms as a cantilever. Applying the boundary conditions, non-trivial solutions exist only when the following characteristic equation is satisfied:

$$\cosh(\beta_n L)\cos(\beta_n L) + 1 = 0 \tag{1.5}$$

Solving Eqn. (1.5) numerically gives the natural frequencies:

$$\omega_n = \frac{a_n}{L^2}\sqrt{\frac{EI}{\rho A}} \tag{1.6}$$

where $a_1 = 3.516$ is the constant corresponding to the first mode. Solutions to the undamped forced-vibration problem show unbounded displacement when the driving frequency matches a natural frequency; the beam therefore resonates. Figure 1.2 shows the mode shapes of vibrating beams under different boundary conditions. Figure 1.2(a) shows the first four mode shapes for a vibrating cantilever beam. If both ends are free, a free-free beam is formed. In this case, the boundary conditions yield:

$$\cosh(\beta_n L)\cos(\beta_n L) - 1 = 0 \tag{1.7}$$

and the natural frequencies are given by the same expression as Eqn. (1.6), but with different values of a_n. Figure 1.2(b) illustrates the first four free-free mode shapes.

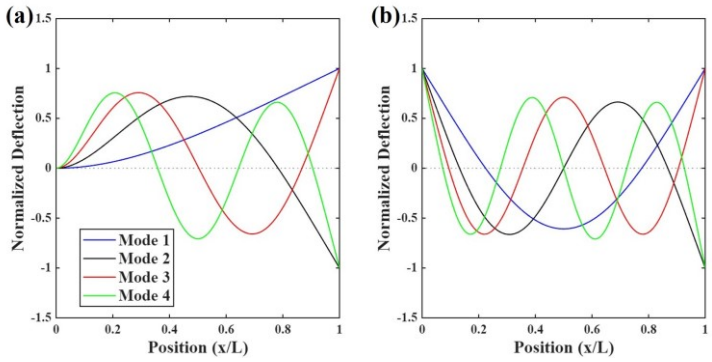


Fig. 1.2 Shapes of the first four modes for (a) cantilever and (b) free-free beams.

In Eqn. (1.6), the second moment of area of a beam about the x- and y-axes depends on the shape of its cross-section and is defined as:

$$I_{xx} = \iint_A y^2 dxdy \qquad I_{yy} = \iint_A x^2 dxdy \tag{1.8}$$

For a circular cross-section of radius r centred at the origin $(0,0)$, as shown in Figure 1.3(a), the second moment of area is:

$$I_{xx} = I_{yy} = \frac{\pi r^4}{4} \tag{1.9}$$

If the circle is shifted upward by a distance d, as shown in Figure 1.3(b), I_{yy} remains the same and I_{xx} can be calculated using the parallel axis theorem:

$$I'_{xx} = I_{xx} + \mathrm{A}d^2 = \mathrm{A}\left(\frac{r^2}{4} + d^2\right) \tag{1.10}$$

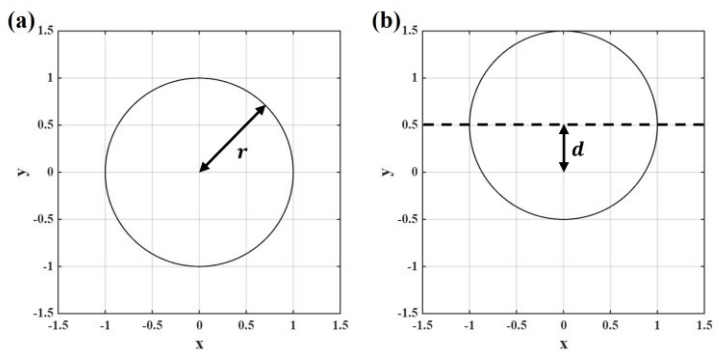


Fig. 1.3 Second moment of area of a circle of radius r with centre at (a) $(0,0)$ and (b) $(0,d)$.

Vibrating Fibre Cantilever

A vibrating fibre with one end fixed is a cantilever beam. Although accurate, Euler beam-bending theory can be computationally complicated. Fortunately, simpler models exist and are sufficiently accurate. For example, under a time-varying drive $F(t)$, the fibre tip motion can be described by a classical mass-spring-damper model, and governed by the second-order differential equation (SDE):

$$m\frac{d^2y(t)}{dt^2} + r\frac{dy(t)}{dt} + ky(t) = F(t) \tag{1.11}$$

where $y(t)$ denotes the displacement of the fibre tip, and m, r, and k are the equivalent mass, damping, and spring constant, respectively. Rearranging and defining the angular resonant frequency $\omega_0 = \sqrt{k/m}$ and the damping ratio $\zeta = r/(2m\omega_0)$ we obtain:

$$\frac{d^2y(t)}{dt^2} + 2\zeta\omega_0\frac{dy(t)}{dt} + \omega_0^2 y(t) = \frac{F(t)}{m} \tag{1.12}$$

When excited by a piezoelectric transducer (PT), the drive becomes $A\sin(\omega t)$, where A and ω denote the amplitude and angular frequency, respectively. Equation 1.12 can often be a sufficient model for a particular mode, provided the resonant frequency and damping coefficient are matched to those estimated from Euler theory or experiment.

For example, to simulate fibre tip motion under a harmonic drive, we may assume the governing equation:

$$\frac{d^2y(t)}{dt^2} + 2\zeta\omega_0\frac{dy(t)}{dt} + \omega_0^2 y(t) = A\sin(\omega t) \tag{1.13}$$

To demonstrate its use, Eqn. (1.13) was implemented in a SIMULINK (MathWorks) model as shown in Figure 1.4. Figure 1.4 shows the SIMULINK block diagram used to numerically solve the SDE. Here, the driving signal is provided by a sinusoidal function generator block with variable amplitude, frequency and phase, and integrator blocks are used instead of derivative blocks to avoid abrupt changes that may cause numerical instability. The displacement is measured and processed in MATLAB (MathWorks).

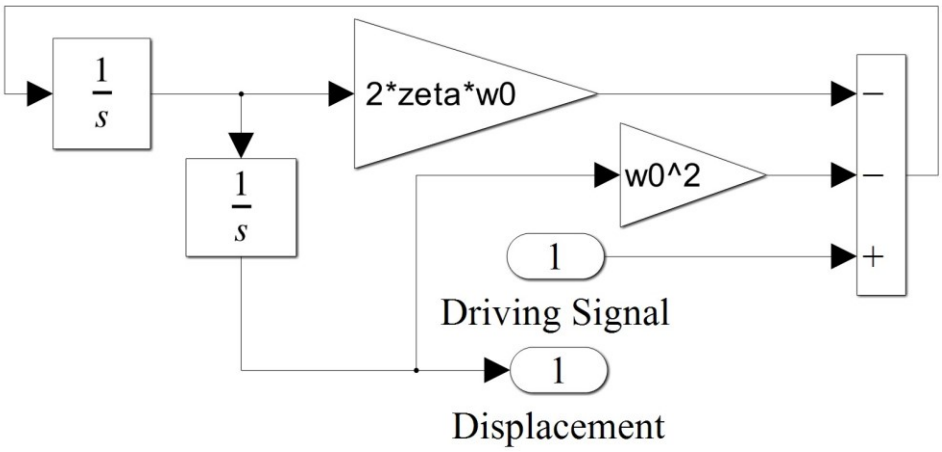


Fig. 1.4 Block diagram of the SIMULINK model used for the numerical solution of the lumped-element model of fibre tip motion.

Figure 1.5 shows simulated steady-state responses of the fibre displacement under sinusoidal excitation at different driving frequencies. These clearly result in different displacement amplitudes, while the vibration frequency of the fibre tip remains identical to the driving frequency. A phase variation is also evident: Figure 1.5(a) shows a −90° phase shift at resonance, whereas Figures 1.5(b) and 1.5(c) correspond to larger and smaller phase differences relative to the resonant condition.

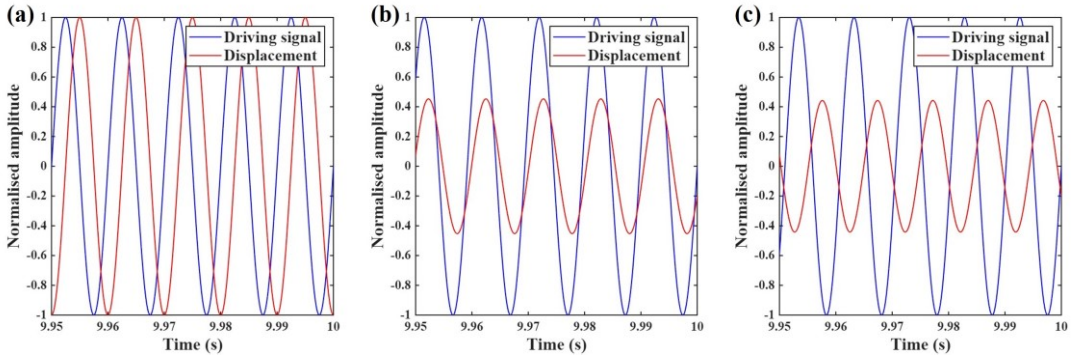


Fig. 1.5 Simulated steady-state responses of the driving signal (blue line) and fibre displacement (red line) for (a) $\omega = \omega_0$, (b) $\omega < \omega_0$ and (c) $\omega > \omega_0$.

These results may be verified analytically as follows. The frequency response can be derived by assuming a harmonic drive $v(t)$ as

$$v(t) = \mathrm{A}e^{j2\pi ft} \tag{1.14}$$

where $f = \omega/(2\pi)$ is the driving frequency. The displacement response is

$$y(t) = \mathrm{B}(f)e^{j2\pi ft} \tag{1.15}$$

where $B(f)$ denotes the frequency-dependent amplitude of the displacement response. Substituting Eqns. (1.14-1.15), along with the first and second derivatives of $y(t)$, into Eqn. (1.13), and using $\omega_0 = 2\pi f_0$, the complex frequency response is obtained:

$$B(f) = \frac{A}{f_0^2 - f^2 + 2j\zeta f f_0} \tag{1.16}$$

from which the amplitude and phase responses follow:

$$|B(f)| = \frac{A}{\sqrt{(f_0^2 - f^2)^2 + 4\zeta^2 f^2 f_0^2}} \tag{1.17}$$

$$arg[B(f)] = \phi(f) = -\tan^{-1}\left(\frac{2\zeta f f_0}{f_0^2 - f^2}\right) \tag{1.18}$$

Thus, the amplitude and phase variations observed in Figure 1.5 are described by Eqns. (1.17-1.18). At resonance ($f = f_0$), the steady-state amplitude and phase are:

$$|B(f_0)| = \frac{A}{2\zeta f_0^2} \tag{1.19}$$

$$\phi(f_0) = -\frac{\pi}{2} \tag{1.20}$$

Hence, the amplitude response reaches its maximum at resonance, where the phase shift is $-\pi/2$, independent of the damping ratio.

Figure 1.6 shows the theoretical and simulated frequency responses of a harmonically driven fibre cantilever, including amplitude and phase behaviour. A frequency of 100 Hz is selected for simulation because typical fibre cantilevers from previous works have a length of 3-5 cm, generating a resonant frequency of approximately 60-140 Hz. In Figure 1.6(a), the amplitude response reaches its maximum at the resonant frequency, indicated by the black dashed line, and decreases rapidly away from resonance. To achieve a large FOV in a fibre scanner, the system should therefore be driven near resonance. In Figure 1.6(b), the phase response decreases sharply and approximately linearly around resonance, approaching 0 and $-\pi$ at frequencies far below and far above resonance, respectively. Figure 1.6(c) shows that the phase remains constant at the resonant frequency regardless of the damping ratio.

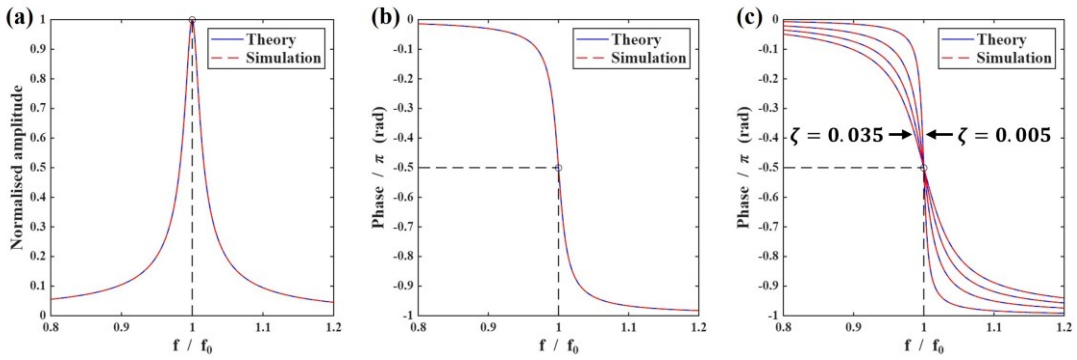


Fig. 1.6 Theoretical and simulated (a) amplitude response and (b) phase response of a harmonically driven fibre cantilever ($f_0 = 100Hz,\ \zeta = 0.01$); (c) phase responses for different damping ratios ranging from 0.005 to 0.035.

The transient response is generally more complicated. Figure 1.7 shows simulated switch-on transient responses of the fibre displacement for different driving frequencies. In Figure 1.7(a), the driving frequency matches the resonant frequency. The fibre displacement exhibits sinusoidal vibration following the driving signal, with an exponentially increasing amplitude during the switch-on transient. The envelope of the displacement can be approximated, by inspection, as

$$y_{env}(t) = \pm\left(1 - e^{-\omega_0 \zeta t}\right) \tag{1.21}$$

In Figures 1.7(b-c), the system operates off resonance, resulting in a reduced steady-state amplitude and an underdamped transient response. Eqn. (1.21) shows that the transient duration is governed by the resonant frequency and the damping ratio, representing the time required for the fibre to reach steady-state motion. These results confirm that the fibre response, although predictable, depends strongly on the drive.

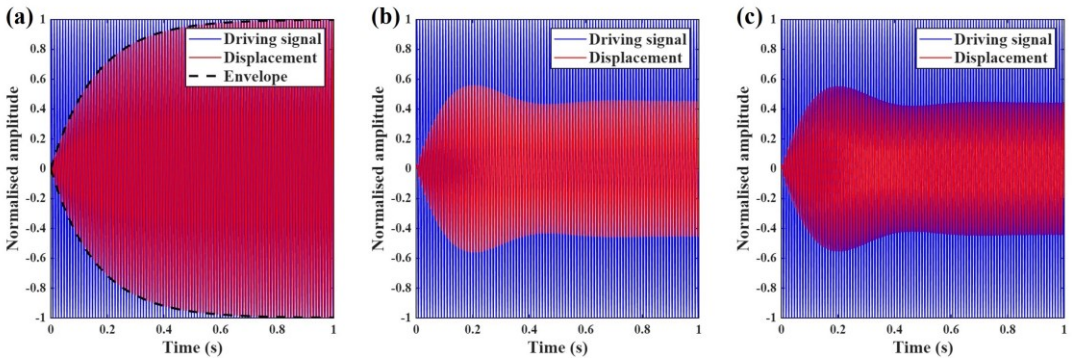


Fig. 1.7 Simulated switch-on transients of the driving signal (blue line) and fibre displacement (red line) for (a) $\omega = \omega_0$, (b) $\omega < \omega_0$, and (c) $\omega > \omega_0$. The displacement envelope (black line) is shown in (a).

Scanning Patterns

When the tip of a fibre cantilever follows a prescribed trajectory, specific scanning patterns can be generated. A one-dimensional (1D) scanning pattern is ideally produced by driving the fibre along a single axis, ideally forming a straight line. Owing to its simplicity and limited practical applications, the 1D scanning pattern is not demonstrated here. However, it is important to note that coupling between orthogonal bending mode resonances makes it difficult to achieve straight-line motion in practice. Figure 1.8 shows the three common two-dimensional (2D) scanning patterns that are widely used in optical imaging systems: raster scanning [34-38], spiral scanning [39-41], and Lissajous scanning [42-43].

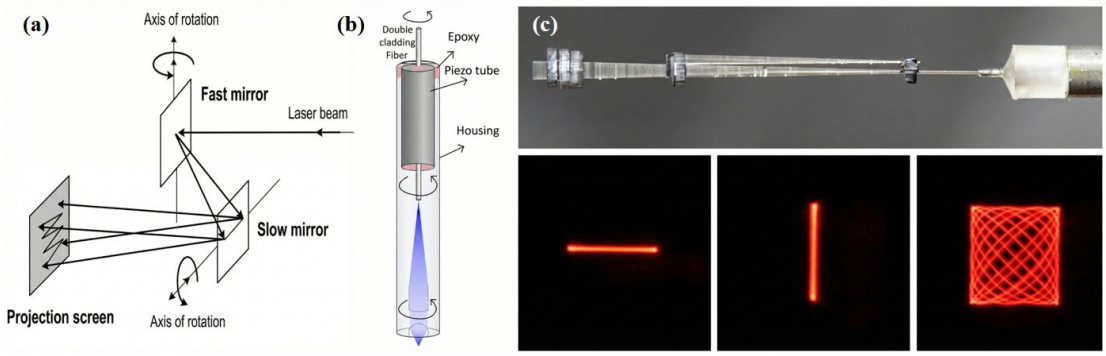


Fig. 1.8 Fibre scanners with (a) raster [34], (b) spiral [39] and (c) Lissajous [42] scanning patterns.

Figure 1.8(a) shows a raster scanner, in which a fast axis and a slow axis are driven by triangular waveforms at different frequencies, as depicted in Figure 1.9(a). Figure 1.9 shows the displacement waveforms, scanning trajectory with sampling points, and corresponding sampling-point distribution for raster scanning. The amplitude of the fast axis is typically modulated by the slow axis, producing the characteristic line-by-line coverage. Because this motion is non-harmonic, its off-resonance amplitude response is negligibly small, as described by Eqn. (1.17). In addition, a triangular waveform contains an infinite number of harmonic components in its Fourier decomposition, which cannot be reproduced by a resonant beam system. As a result, raster scanning is unsuitable for resonant fibre cantilevers and is instead implemented using mechanical systems such as MEMS scanning mirrors. The resulting trajectory with sampled points, shown in Figure 1.9(b), exhibits a distinct zigzag pattern that is effective for capturing

horizontal features but less suited to representing vertical structures. The point distribution of a raster scan, illustrated in Figure 1.9(c), is broadly uniform across the field, with reduced sampling density near the edges because the spacing between successive horizontal extrema increases toward the outer region.

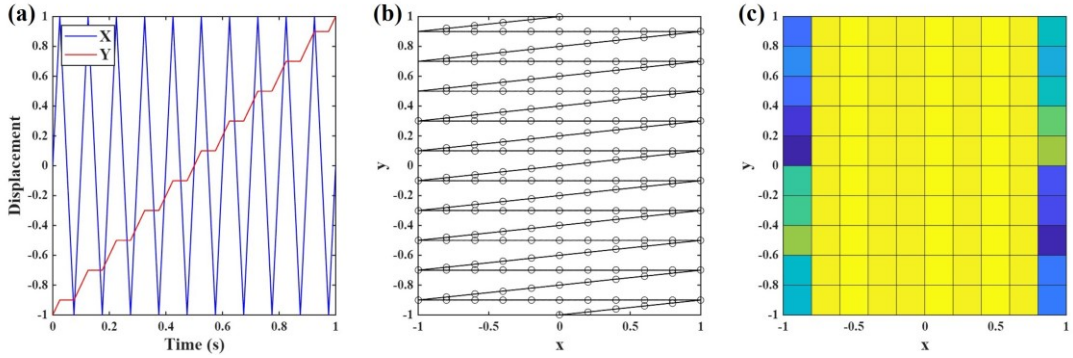


Fig. 1.9 (a) x- and y- displacement, (b) trajectory and sampling points, and (c) distribution of sampling points for raster scan.

To exploit the resonant behaviour of the fibre and achieve a maximal FOV, two additional scanning patterns are more commonly used. Figure 1.8(b) shows a spiral scanner. Figure 1.10 shows the displacement waveforms, scanning trajectory with sampling points, and corresponding sampling-point distribution for spiral scanning. The scanning trajectory of the x- and y-displacements of the fibre satisfy:

$$\begin{bmatrix} x \\ y \end{bmatrix} = \mathrm{A}(t) \begin{bmatrix} \sin(2\pi f t) \\ \cos(2\pi f t) \end{bmatrix}, \tag{1.22}$$

Here the two orthogonal motions have identical frequencies and a 90° phase difference. The amplitude is modulated by another sinusoidal function $A(t) = \sin(2\pi f_l t)$ with a lower frequency $f_l = 0.5$, as shown in Figure 1.10(a), and the resulting trajectory with sampling points, presented in Figure 1.10(b), forms a spiral pattern with decreasing separation between consecutive lines as the trajectory progresses from the central region toward the outer region. One approach to correcting the uneven spacing is to use a triangular function for amplitude modulation. However, as mentioned above, a triangular waveform cannot easily be reproduced by a resonant beam system. In addition, the triangular amplitude modulation contains non-differentiable corners that cannot be physically realised in a practical driving signal, necessitating smoothing of these transitions.

The spiral pattern is naturally compatible with resonant fibres and is one of the simplest 2D scanning schemes. However, because it relies on a single drive frequency, the two orthogonal axes are susceptible to mechanical coupling, leading to scan-line distortion and increased sensitivity to environmental disturbances and mechanical imperfections. In addition, the distribution of sampling points, shown in Figure 1.10(c), exhibits significantly higher density near the centre, decreasing with radial distance. This non-uniform distribution results in spatial variations in both resolution and illumination intensity across the FOV.

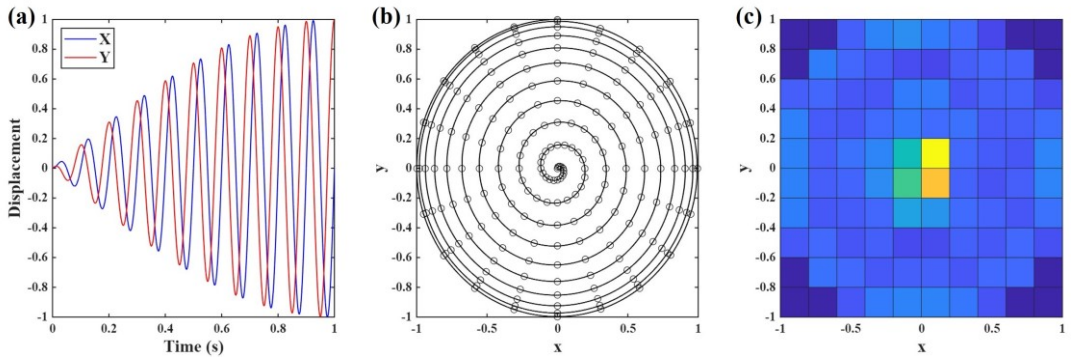


Fig. 1.10 (a) x- and y- displacement, (b) trajectory and sampling points, and (c) distribution of sampling points for spiral scan.

Figure 1.8(c) shows a Lissajous scanner. The curves were first recognised in the 19th century through observations of the motion of the Earth as viewed from the Moon [44], and similar trajectories were described mathematically by analysing the motion of a pendulum suspended from two orthogonal pivot points [45]. The concept later gained prominence through optical displays by Lissajous in which light was reflected from mirrors attached to two tuning forks vibrating at different frequencies, producing figures that are now known as Lissajous patterns [44]. These curves are determined by the frequency ratio and relative phase of the two orthogonal harmonic motions, and numerous apparatuses have since been developed to illustrate their properties [47]. Currently, the Lissajous curve has been used in atomic force microscopy (AFM) [48-49] and magnetic particle imaging (MPI) [50-51], where dual-frequency excitation enables dense spatial coverage and high scanning speeds. Its ability to generate quasi-uniform sampling using two harmonics makes it suitable for fibre scanners.

Figure 1.11 shows the displacement waveforms, scanning trajectory with sampling points, and corresponding sampling-point distribution for Lissajous scanning. Compared with spiral and raster scans, the Lissajous pattern requires no amplitude modulation of the driving signals of the PTs and can be achieved using resonant fibres. The trajectory is defined by:

$$\begin{bmatrix} x \\ y \end{bmatrix} = \begin{bmatrix} \sin(2\pi f_x t) \\ \cos(2\pi f_y t) \end{bmatrix} \tag{1.23}$$

where f_x and f_y are the vibration frequencies along the x- and y-axes, respectively. The individual motions are shown in Figure 1.11(a), and the resulting trajectory with sampling points, shown in Figure 1.11(b), forms a symmetric Lissajous figure. The sampling-point distribution in Figure 1.11(c) exhibits a nearly square and largely uniform illumination profile, with slightly higher density near the four corners.

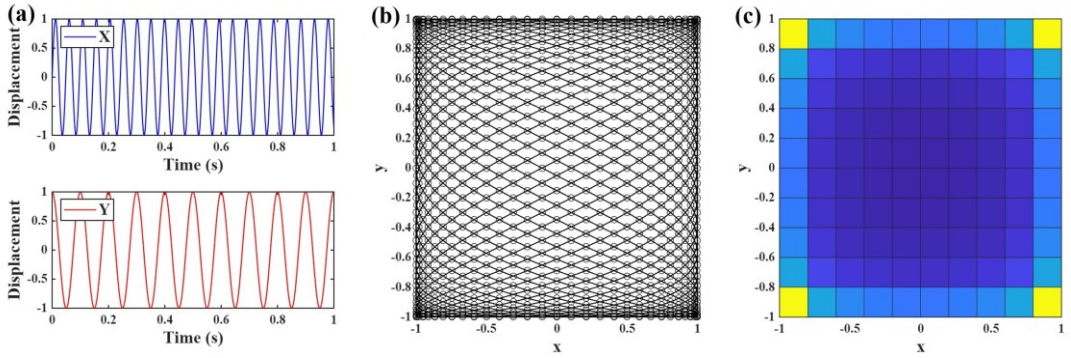


Fig. 1.11 (a) x- and y- displacement, (b) trajectory and sampling points, and (c) distribution of sampling points for Lissajous scan. ($f_x = 20.67Hz,\ f_y = 10Hz$)

Because the fibre is driven at two distinct resonant frequencies, the Lissajous pattern is naturally suited to fibres with asymmetric structures, which inherently support non-degenerate orthogonal bending modes. The use of two independent resonances reduces mechanical coupling, enabling high-speed, high-density scanning with high spatial uniformity. Since the vibration frequencies in the two orthogonal directions are distinct, and assuming $f_x > f_y$, their rational ratio r can be expressed as:

$$r = \frac{f_x}{f_y} = m + \frac{1}{n} \tag{1.24}$$

where m and n are positive integers. When $m = 1$, the two orthogonal vibration modes may become cross-coupled, causing the Lissajous trajectory (red line) to deviate from the ideal trajectory (blue line), as shown in Figure 1.12(a). In Figure 1.12(b), when n is an even integer, the resulting trajectory (red line) exhibits non-symmetric behaviour at the left and right edges, as indicated by the black dashed box. Conversely, when n is odd, a symmetric trajectory (blue line) is obtained. Figure 1.12(c) shows that increasing the value of n leads to a higher scan density, as illustrated by the blue trajectory compared with the black trajectory. Therefore, to achieve a symmetric and densely sampled Lissajous scanning pattern, the following conditions should be satisfied: $m \geq 2$, n is odd, and n is as large as practicable.

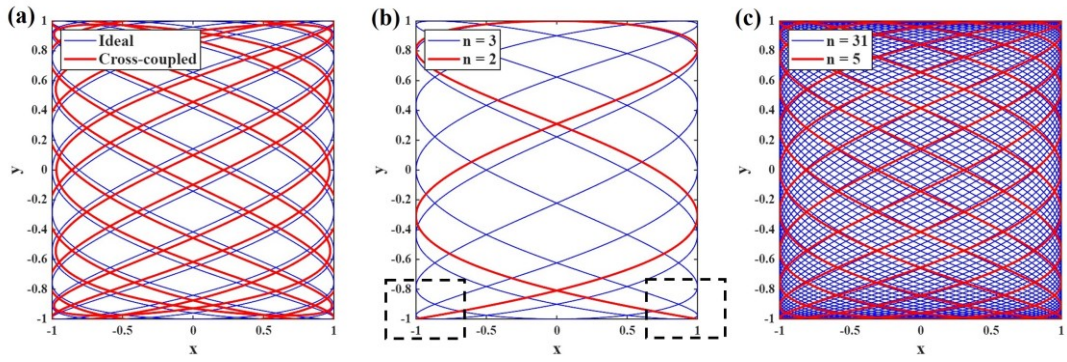


Fig. 1.12 Lissajous scanning pattern for (a) ideal and cross-coupled cases, (b) odd and even values of n and (c) large and small values of n.

1.2 Imaging Optics

This section introduces the imaging optics required in a fibre scanner, including lens-based imaging, confocal detection, dual numerical aperture (NA) operation, and the fibre fabrication methods.

Imaging Principles

Figure 1.13(a) shows the general arrangement for imaging. The key optical element in the system is an imaging lens. Its primary parameters are the focal point F and the focal length f. The focal point is defined as the position at which parallel incoming rays converge after passing through the lens, while the focal length is the distance between this point and the centre of the lens. The fibre motion, indicated by the downward-pointing arrow on the right, generates a diverging beam that is transformed by the lens.

One ray passes through the centre of the lens without deviation, while another enters parallel to the optical axis and is refracted to pass through the focal point. These two rays intersect at the position indicated by the upward-pointing arrow on the left, forming a magnified and inverted version of the scanning pattern by simple geometric optics. The relationship between object distance u, image distance v, and focal length f is described by the thin-lens equation:

$$\frac{1}{v}+\frac{1}{u}=\frac{1}{f} \tag{1.25}$$

The magnification M of the imaging systems is then given by:

$$M=\frac{v}{u} \tag{1.26}$$

In a fibre scanning system, the fibre tip motion is therefore projected onto the imaging plane as a magnified version of its trajectory.

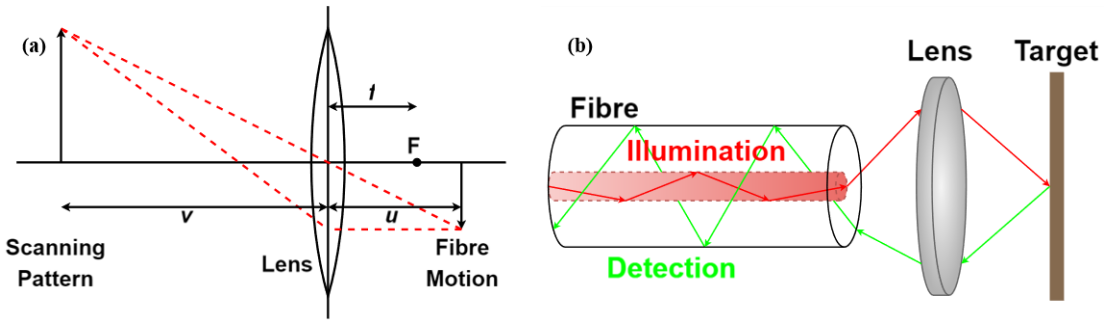


Fig. 1.13 Schematic diagrams for the principles of (a) imaging and (b) dual NA confocal detection.

Figure 1.13(b) shows the principle of fibre-based confocal detection. The illumination beam is guided through the fibre core, shown as the red region at the centre of the fibre. Because the refractive index of the core is higher than that of the surrounding cladding, light is confined by total internal reflection (TIR). The NA describes the maximum acceptance angle for light coupling into the core under TIR:

$$NA=\sqrt{n_{core}^2-n_{clad}^2} \tag{1.27}$$

where n_{core} and n_{clad} are the refractive indices of the core and cladding, respectively. Light emerging from the core is focused by the lens onto the target, and the backscattered light from the sample is refocused by the same lens onto the fibre's

end face. Because the core has much higher numerical aperture, most of the returning light is captured as cladding modes. Importantly, the distances from the lens to both the core and the cladding are identical at the fibre facet; both lie on the same focal plane. As a result, the backscattered light is efficiently coupled into the cladding, enhancing detection efficiency and image contrast. This configuration constitutes a dual NA confocal detection scheme, which achieves higher efficiency by removing the constraints from the core's NA. The received power in the core and cladding depends on the square of their numerical apertures [52], and the maximal signal gain obtained by this approach is:

$$G = \frac{NA_L^2 - NA_F^2}{NA_L^2} \tag{1.28}$$

where the subscripts L and F refer to lens and fibre. By utilising the fibre's cladding rather than its narrow core for signal collection, the system accesses a much larger NA (increasing from the core's $NA \approx 0.12$ to the lens-limited $NA \approx 0.37$), thereby improving imaging efficiency.

Other aspects are also important. For example, the absolute spatial resolution of a fibre-based scanning system, whether used for imaging or precise beam delivery, is fundamentally limited by the spot size at the sample plane, which is constrained by diffraction in accordance with Abbe's diffraction limit [53]. Specifically, the smallest resolvable feature size d depends on the wavelength λ and the NA of the system:

$$d = \frac{\lambda}{2NA} \tag{1.29}$$

This relationship indicates that shorter wavelengths or higher numerical apertures yield finer resolution. Consequently, even an ideal fibre scanner is inherently diffraction-limited: its maximum resolving power is restricted by the wave nature of light and the NA of the fibre-lens system, consistent with the classical Abbe criterion [54]. However, the distribution of sampling points along the trajectory normally forms a coarser and more important scan-limited resolution limit.

Optical Fibre Fabrication

Optical fibres can be broadly categorised into two types: single-mode fibres (SMFs) and multimode fibres (MMFs). Although their cross-sections will be illustrated later, it is sufficient here to note that MMFs possess a significantly larger core diameter than SMFs. Combined with the refractive-index contrast between the core and cladding, this allows MMFs to support multiple modes, whereas SMFs guide only a single fundamental mode. MMFs are generally unsuitable for high-resolution fibre scanners because interference between the modes produces complex speckle patterns. In practice, a well-defined Gaussian beam launched into an MMF emerges with a chaotic intensity distribution, leading to a broad, poorly defined focal spot and severely limiting spatial resolution. In contrast, an SMF supports only the fundamental mode, whose transverse intensity profile is close to Gaussian and can be focused down to the diffraction-limited spot size defined by Eqn. (1.29). For this reason, various types of SMFs have been widely employed in fibre-scanning systems and are discussed in the following sections, while the use of MMFs in specialised applications will be considered later.

As mentioned earlier, the Lissajous pattern is naturally suited to fibres with asymmetric structures. Based on Eqn. (1.6), the natural frequencies depend on the second moment of area, which is determined by the cross-sectional shape and the position of the bending axes. Therefore, when the cross-section is asymmetric, the resonant frequencies in the two orthogonal directions can be different. For Lissajous fibre scanners, the scanning pattern is produced by driving the fibre at two distinct frequencies corresponding to its orthogonal bending axes. A variety of commercial off-the-shelf (COTS) fibres have been used, including regular SMFs [55-56] and various polarisation-maintaining fibres (PMFs) [57-63], as shown in Figure 1.14. Figure 1.14(a) shows the cross-section of a conventional SMF. Light is guided by the small circular core at the centre, which is surrounded by a cladding of slightly lower refractive index, enabling single mode guidance through total internal reflection. However, the circular symmetry of SMFs leads to identical orthogonal bending modes, meaning that the two resonant frequencies coincide. This degeneracy makes SMFs unsuitable for Lissajous

scanning, which requires two distinct resonant frequencies. Figures 1.14(b-c) show two representative PMF designs: elliptical-core fibres and polarisation-maintaining and absorption-reducing (PANDA) type fibres. In these fibres, light is guided by an asymmetric or stress-induced birefringent core, producing linearly polarised modes that are useful for specific applications. Their asymmetry also introduces distinct orthogonal bending resonances, which in principle makes them compatible with Lissajous scanning. However, in practice, the frequency separation is typically small, so the two modes remain strongly mechanically coupled, leading to significant distortion in the Lissajous pattern.

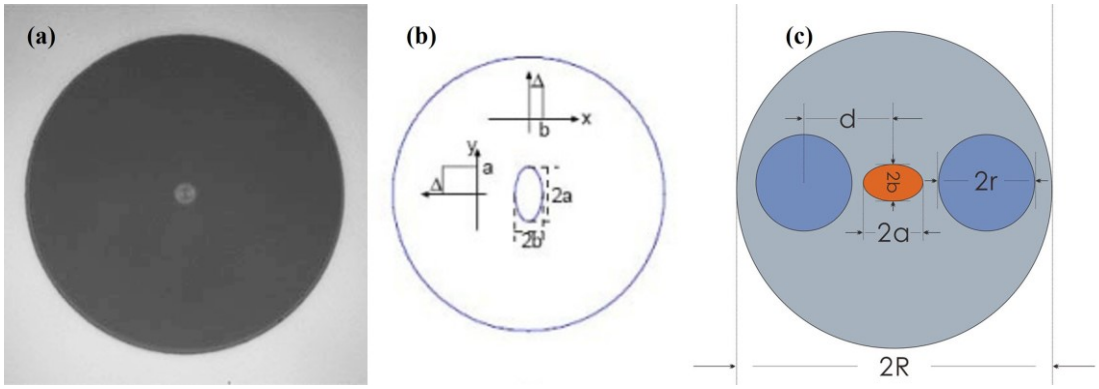


Fig. 1.14 Cross-sections of (a) a regular single mode fibre (Thorlabs), (b) an elliptical-core fibre [58] and (c) a polarisation-maintaining and absorption-reducing type fibre [62].

As noted earlier, the Lissajous pattern is governed by the ratio of the two resonant frequencies. Therefore, in addition to achieving distinct orthogonal resonances, it is essential that this ratio can be precisely controlled. To further increase the frequency separation and enable accurate tuning of the ratio, two approaches have been proposed in the literature. The first involves polishing a standard SMF to form a D-shaped cross-section, producing what is known as a D-type fibre [64-65]. As shown in Figure 1.15(a), removing material from one side of the cladding introduces strong geometric asymmetry, and the resulting frequency ratio can be adjusted by controlling the polish. However, the achievable frequency separation remains modest, and the polishing process is labour-intensive, making it inefficient and difficult to reproduce. A second method, shown in Figure 1.15(b), involves attaching additional components to the fibre to create an uneven stiffness distribution along the two orthogonal axes [66-68]. This

approach can yield resonant frequency ratios approaching 1.5, significantly reducing mechanical coupling and enabling more robust control of the Lissajous trajectory. However, these composite structures require manual assembly and are difficult to scale for mass production. Moreover, the tailored stiffness distribution is typically optimised only for a specific cantilever length, limiting the ability to vary the absolute resonant frequencies without simultaneously altering the frequency ratio.

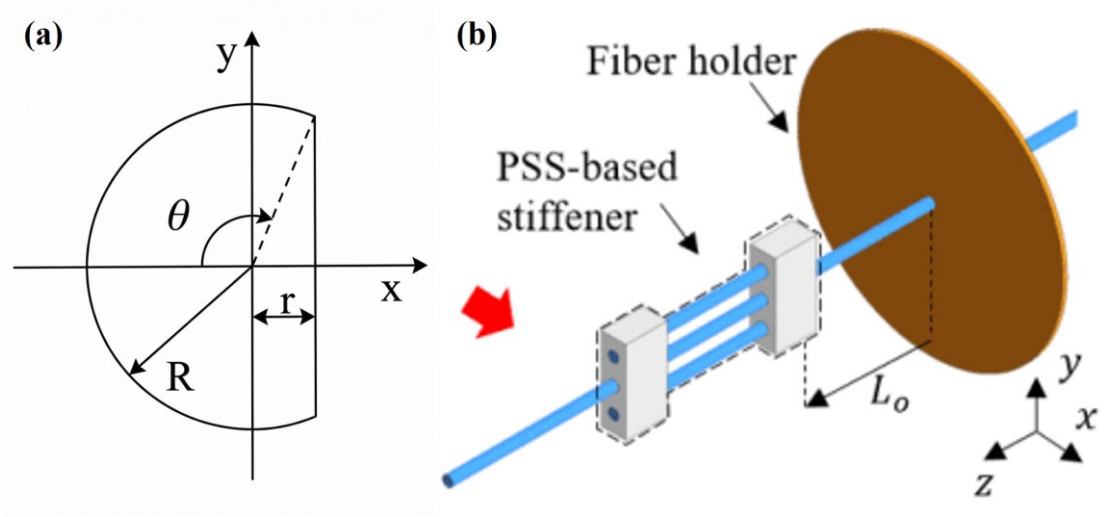


Fig. 1.15 (a) Cross-section of a D-type fibre [65] and (b) schematic of a single-mode fibre under asymmetric stiffness modulation [68].

To the best of our knowledge, the most effective approach to date is the dip-coating method [69]. In this technique, two SMFs are bonded together using a polymer fillet formed during the dip-coating process, creating a dual-core composite structure. Figure 1.16(a) shows the resulting cross-section. The resonant-frequency ratio is governed by the geometry of the bonded region and the amount of polymer deposited between the fibres, and is typically close to 2, effectively eliminating mechanical coupling between the orthogonal bending modes. Because dip-coating is a mature and controllable fabrication technique, the process parameters, and hence the frequency ratio, can be tuned precisely. In addition, the method is efficient, reproducible, and well suited to mass production. Furthermore, unlike stiffness-modulated fibre designs, the dip-coated structure maintains a nearly constant frequency ratio regardless of the cantilever length. We also investigated the possible dip-coating of more than two fibres; however, we found that using more fibres distorts the Lissajous curve, which cannot be fixed in

further processing. In addition, the decoupling effect became marginal. Therefore, two fibres were chosen for optimal scan line generation.

As demonstrated to date, the method has some limitations. In particular, it deposits the polymer fillet layer by layer. This results in discrete resonant frequency ratios, which limits the tuning range. Furthermore, this process involves immersing the fibre in liquid polymer, making it unsuitable for photonic crystal fibres (PCFs) and photonic bandgap (PBG) fibres and thereby limiting its compatibility with future fibre design.

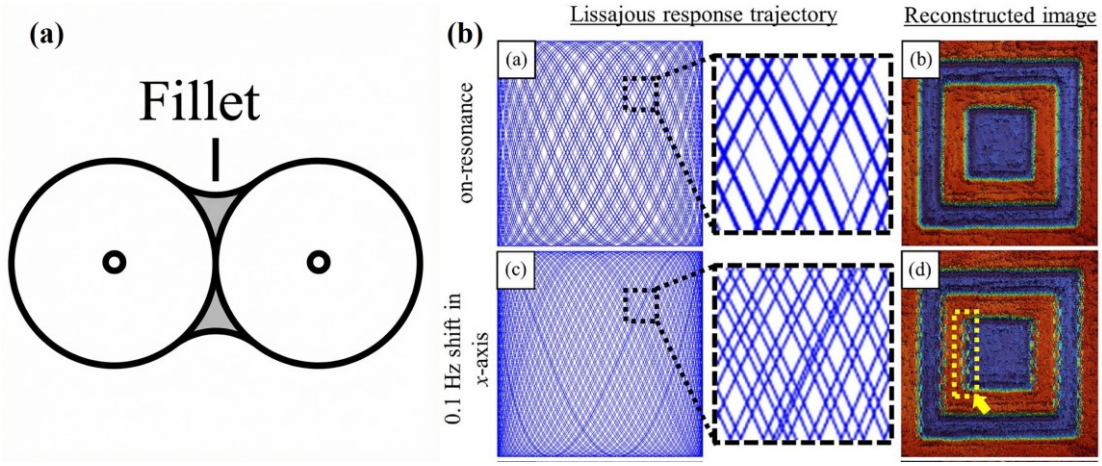


Fig. 1.16 (a) Cross-section of a dip-coated fibre [69] and (b) the difference of Lissajous trajectories with frequency and phase errors and the resulting reconstructed images [70].

1.3 Tracking of Fibre Motion

During image reconstruction, the backscattered light collected in the cladding, together with the estimated position of the fibre tip, forms a 2D map of the intensity distribution. The sampling strategy for reconstructing this distribution will be discussed in detail later; here, we focus on how the fibre tip position is tracked and why this information is essential for 2D Lissajous scanning. Accurate knowledge of the tip position is crucial for image reconstruction: without it, the positional data may deviate from the ideal trajectory, and the scan pattern may drift due to external disturbances. Figure 1.16(b) shows how the Lissajous trajectory changes when the frequency in the x-direction is altered by only 0.1 Hz [70]. The enlarged region inside the black dashed box highlights a clear deviation from the ideal trajectory. The resulting distortions in the reconstructed image are marked by the yellow dashed box. This example shows that even small errors

in frequency or phase can significantly affect the scanning pattern. Therefore, continuous monitoring of the fibre tip position and real-time control of frequency and phase are essential for stable and accurate Lissajous scanning. In fact, errors may be clearly seen in the Lissajous pattern shown earlier in Figure 1.8(c).

A range of fibre-control and trajectory-tracking algorithms have been proposed to stabilise or correct the scanning pattern [71-74]. One approach is to use feedback control with a position-sensitive detector (PSD) placed at the fibre tip. In such schemes, a state-space controller typically combines a feedforward element, which generates the nominal dual-frequency drive signals, with a feedback loop that compensates for deviations from the intended motion in real time. However, the function of the PSD is restricted to trajectory measurement to pre-calibrate the fibre scanners. Consequently, the system becomes unobservable and uncontrollable during normal imaging operation [75-76]. As a result, these approaches do not provide true real-time control. To enable real-time tip-position tracking, another approach is to attach micro-metallic components to the fibre tip and surround it with a conductive cylindrical housing, thereby generating capacitive feedback signals as the fibre moves [77-78]. However, this method suffers from two major limitations. First, the capacitive response is strongly nonlinear, making the system difficult to model and complicating controller design. Second, the capacitance must be pre-calibrated, which renders the technique highly sensitive to environmental disturbances such as temperature drift, humidity changes, and small mechanical misalignments. A fully observable configuration has also been demonstrated in which PSDs are used during active scanning. Rather than relying on pre-calibration, the emitted optical power is diverted using a beamsplitter for tip tracking [79]. Alternatively, specially designed PSDs, such as the transmissive device shown in Figure 1.17(a), allow the excitation beam to pass through while simultaneously measuring the tip position [80]. Although these approaches maintain observability, they require a significant fraction of the optical power for the PSD to operate reliably. This reduces the signal-to-noise ratio (SNR) of the imaging channel and increases susceptibility to environmental noise.

Figure 1.17(b) shows another method using aperture-based optical feedback. A metal aperture is positioned in front of the fibre tip such that, when the fibre reaches its displacement extremities, a portion of the emitted beam is reflected backwards [81-82]. This produces a pulse train whose peaks correspond to the turning points of the fibre motion. Under this scheme, the system becomes only partially observable [83-84], but appropriate signal-processing filters can be designed to extract the harmonic components and reconstruct the periodic underlying motion, thereby providing full observability in principle. However, the development of this method remains incomplete. Existing demonstrations have implemented feedback control only for 1D scanning [81], and no effective design has yet been realised for 2D operation. Additionally, programmable 2D Lissajous fibre scanners capable of trajectory definition have not yet been developed [85-86].

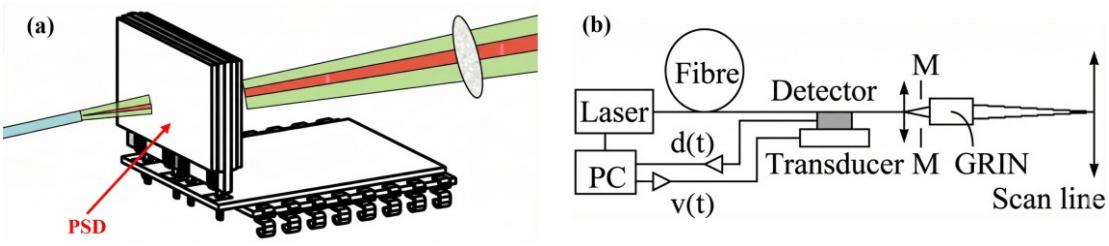


Fig. 1.17 Fibre tracking using (a) a position-sensitive detector [80] and (b) an aperture [81].

1.4 Control Systems

This section introduces the principles of general closed-loop feedback control and the use of Costas loops or phase-locked loops (PLLs) for controlling harmonic systems. Methods for generating ratioed frequencies are also discussed.

Closed-loop Feedback

Closed-loop feedback control uses negative feedback to force a system's output to follow a desired input [87]. In Figure 1.18(a), the reference input $r(t)$ and the measured output $y(t)$ are compared at a summing junction to produce an error signal $e(t) = r(t) - y(t)$. The controller acts on this error and drives the system such that the new output increasingly matches the reference. A portion of the output is fed back through a sensor to the summing junction with negative sign, causing the loop to

continuously push the output toward the reference value. In steady state, the feedback signal equals the target, and the error ideally approaches zero. In the time domain, the loop dynamics govern how the output evolves in response to a change in input. For example, a sudden change in the reference (such as a step) produces a non-zero error, and the controller responds by adjusting the system until the output converges to the new value. In many simple cases, the output rises exponentially toward the reference. For a unit-step input $u(t)$, a first-order closed-loop system produces:

$$y(t) = \left(1 - e^{-\frac{t}{\tau}}\right) u(t) \tag{1.30}$$

so that $y(\infty) = 1$. During this transient response, the output may overshoot or oscillate depending on the loop design: a critical-damped loop converges smoothly (black solid line), whereas under-damped (blue solid line) or over-damped (red solid line) loops exhibit overshoot or sluggish settling as displayed in Figure 1.18(a). As shown in Figure 1.7, even when the input signals are sinusoidal, the envelope of the switch-on transient follows the exponential convergence described by Eqn. (1.30).

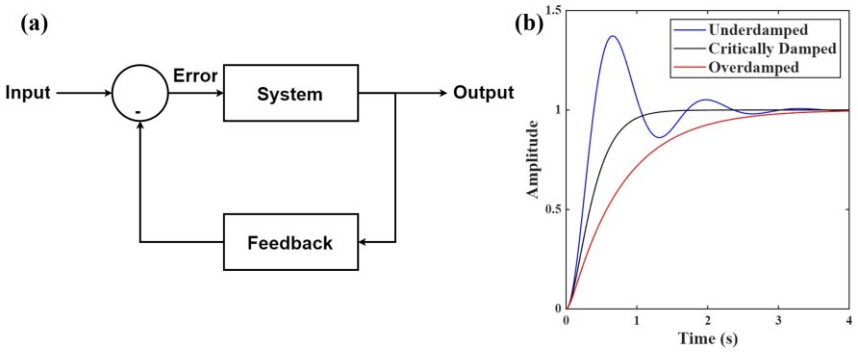


Fig. 1.18 (a) Block diagram of a closed-loop feedback system and (b) example transient responses.

Three key parameters characterise the performance of a closed-loop system: steady-state error, stability, and convergence rate. The steady-state error, defined as:

$$e(\infty) = \lim_{t \to \infty} \left(\mathrm{r}(t) - y(t)\right) \tag{1.31}$$

quantifies the long-term offset between the desired and actual outputs. In an ideal controller, the steady-state error is zero, although in practice a small nonzero value is typically tolerated to ensure robust and stable operation. Stability refers to whether the

output eventually settles to a steady value following a change or disturbance. A stable system gradually approaches the desired output, potentially with decaying oscillations. By contrast, an unstable system exhibits responses that diverge or oscillate indefinitely. Achieving stability requires careful tuning of the feedback gain: too little gain yields slow or inaccurate tracking, while excessive gain causes overshoot, persistent oscillation, or instability. Proper gain selection balances accuracy, speed, and robustness, ensuring that the system converges smoothly with minimal error.

For a 2D Lissajous scanner, both the frequency and the phase of the orthogonal bending modes must be precisely controlled, which requires a different control system. In communication systems, Costas loops or PLL are widely used to recover time-varying signals, such as those in binary phase-shift keying (BPSK) modulation, by locking both the frequency and phase of a local oscillator to those of an incoming signal [88-90]. Figure 1.19 shows a typical Costas loop architecture. The input signal is multiplied by two locally generated sinusoids: one from a voltage-controlled oscillator (VCO), and the other produced by passing the same VCO output through a Hilbert transform to introduce a 90-degree phase shift. After multiplication, the lower branch generates an error term that encodes the frequency and phase mismatch between the VCO and the input signal [91-92]. This error is passed through a loop filter, which adjusts the VCO parameters until the mismatch is eliminated. Once locked, the recovered demodulated signal is obtained from the upper branch.

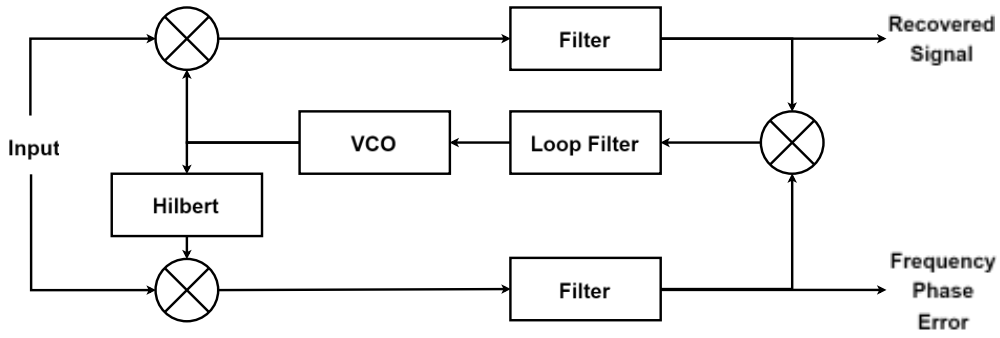


Fig. 1.19 Block diagram of a Costas loop.

Key performance parameters include the pull-in range and lock-in range, which define the frequency intervals over which acquisition and phase locking can occur. The pull-in range, also known as the capture range, refers to the maximum frequency error

for which the loop can eventually achieve lock, starting from an initially unlocked state. By contrast, the lock-in range is the narrower frequency band over which the loop, once locked, can continue to track changes without losing phase lock. Ensuring that the system's starting frequencies fall within the capture range is critical for acquisition, especially in 2D Lissajous scanning where precise synchronisation of orthogonal modes is essential.

Ratioed Frequency Generation

Here, we introduce several circuits capable of generating frequency ratios, including digital frequency dividers (divide-by-N circuits) [93-97] and frequency synthesisers [98-100]. Figure 1.20(a) shows a typical fractional divide-by-N circuit. The clock signal is processed by digital logic to produce a fractional frequency-divided output. Although such circuits can generate precise ratios, the ratio is fixed by the preset digital configuration, making adjustment difficult. Frequency synthesisers, shown in Figure 1.20(b), combine two integer counters with a Costas loop. The input and output frequencies are divided by integers A and B to produce the same intermediate frequency, which is then synchronised by the loop. In steady state, the output frequency becomes B/A times the input. However, these synthesisers require additional programming effort to configure the counters, and their convergence rate is slow.

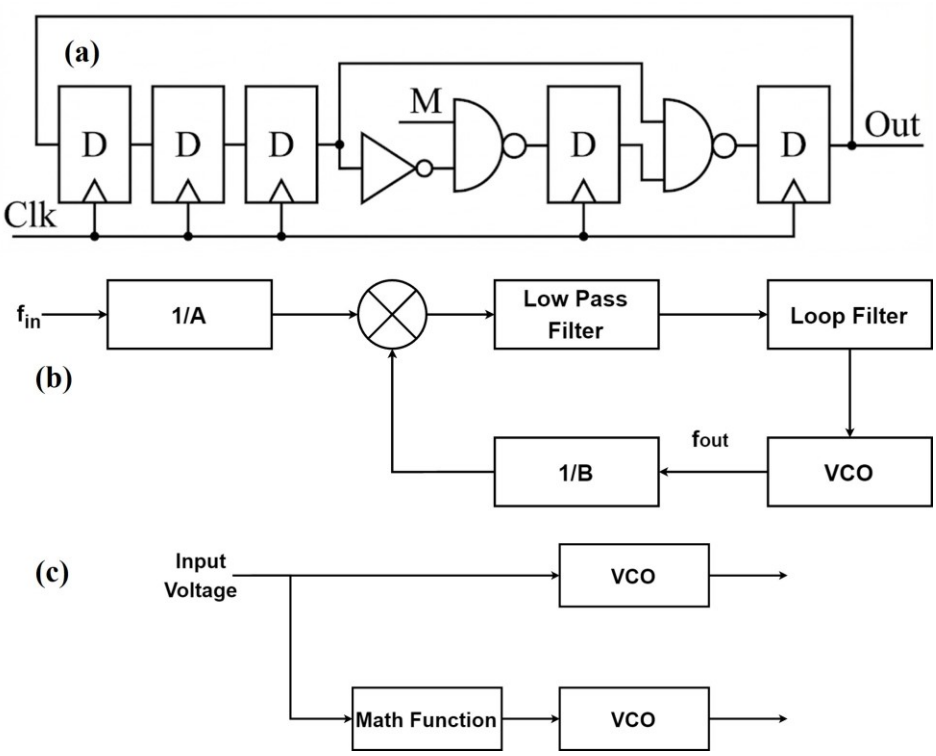


Fig. 1.20 (a) Digital frequency divider [95], (b) frequency synthesiser and (c) VCOs.

In dual-frequency generation, distinct excitation frequencies must be applied simultaneously to excite the two bending modes of the fibre. Therefore, the ability to manipulate and adjust the generated frequencies dynamically is essential for achieving real-time control. To accomplish this, two VCOs are used with ratioed voltage inputs. A mathematical function block, constructed from arithmetic units such as adders and multipliers, determines the output frequency ratio, as illustrated in Figure 1.20(c). This circuit allows the frequency ratio to be controlled simply by changing the input voltage and enables dynamic adjustment of the generated signals.

1.5 Multi-wavelength Detection

In addition to the challenges associated with real-time control, achieving stable multi-wavelength operation for full-colour imaging introduces further complexities. This section introduces the mechanisms currently used for multi-wavelength light detection and the different types of fibres employed in multi-wavelength systems. In addition, chromatic aberration in multi-wavelength optical systems is discussed.

Light Detection

In fibre-based confocal detection, illumination is delivered through the fibre core as described earlier, while the backscattered light at various wavelengths is collected through the cladding [52], via external optics [101], or using auxiliary fibres [102] for image reconstruction. Recent advances have enabled spectral separation using dichroic mirrors and optical filters [103-104]. Dichroic mirrors operate through thin-film interference: multiple dielectric layers are engineered such that specific wavelength bands are reflected while others are transmitted, allowing efficient separation of excitation and emission paths in multi-wavelength systems. Optical filters, such as bandpass, long-pass, or short-pass filters, use similar multilayer structures designed to transmit only a defined spectral range while rejecting the remainder. Together, these components provide precise wavelength selection and routing of backscattered signals, which is essential for high-resolution, multi-channel fibre-based imaging. This capability has expanded the range of applications, enabling Raman endoscopy [105], fluorescence imaging [106], OCT [107], and full-colour endoscopy [108-110]. Nevertheless, existing colour fibre-scanner designs still require complex optical assemblies, often bulky, lossy, and difficult to align, which limits their efficiency and the practicality of compact systems.

Optical Fibres for the Multi-Wavelength Scanner

Several types of fibres have been employed in multi-wavelength scanning systems. Although SMFs support only the fundamental mode and can produce small focal spots, they operate over a narrow wavelength range [111-112], making them unsuitable for broadband or multi-wavelength operation. MMFs, shown in Figure 1.21(a), have a much larger core and therefore support many spatial modes. Interference between these modes leads to a broadened and unstable output field, resulting in a larger and poorly defined spot size [113-114]. For this reason, MMFs are unsuitable for beam delivery, although they can be used to collect backscattered light. In some designs, auxiliary MMFs have been arranged around the illumination fibre to improve backscatter reception [115]; however, this increases the diameter of the probe and compromises miniaturisation. Backscattered light is also commonly collected from the core of MMFs

and routed using beamsplitters or fibre couplers together with wavelength-selective filters [116-118]. This approach suffers from low optical efficiency and requires complex fibre-based components.

A potential solution lies in hollow-core photonic bandgap (HC-PBG) fibres [119-120] and PCFs [121-122]. PCFs, shown in Figure 1.21(b), guide light using a solid silica core surrounded by a microstructured cladding of periodically arranged air holes [123-126]. This architecture fixes the effective refractive-index contrast over a broad spectral range, allowing the fibre to remain endlessly single-mode and therefore suitable for broadband beam delivery. HC-PBG fibres, illustrated in Figure 1.21(c), guide light within an air-filled core surrounded by a photonic bandgap cladding [127-128]. The periodic air-hole pattern creates a spectral bandgap in which no cladding modes can propagate, so only a single defect mode in the core is supported. When operated within this bandgap, the fibre naturally maintains single-mode guidance over a wide wavelength range. In addition, because the core is air-filled rather than silica, HC-PBG fibres can handle significantly higher optical powers, enabling applications such as direct laser writing and high-power endoscopic imaging. However, the approximately circular cross-sections of both PCFs and HC-PBG fibres limit the available scanning patterns to single-frequency spiral trajectories. Existing fibre-tailoring approaches, such as asymmetric stiffness modulation and conventional dip-coating are either difficult to assemble or incompatible with holey fibres.

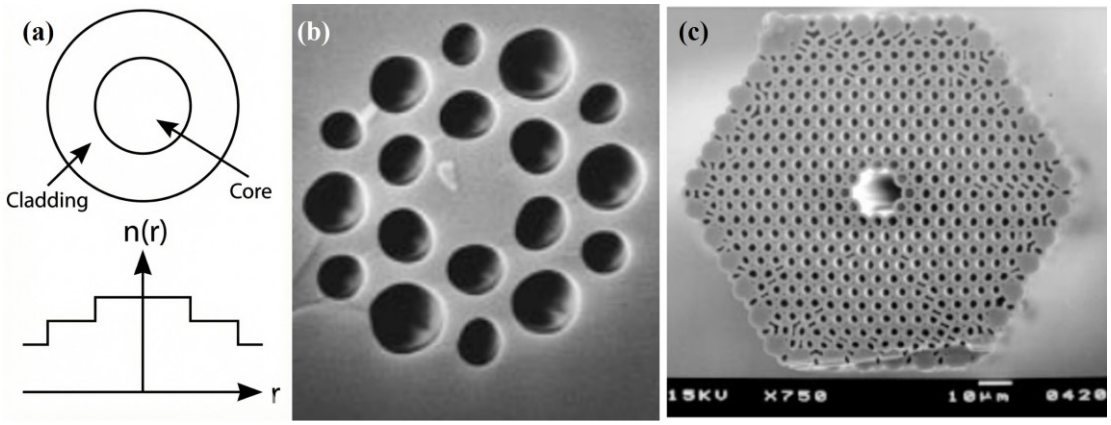


Fig. 1.21 Cross-sections of (a) multi-mode fibre, (b) photonic crystal fibre [126] and (c) photonic bandgap fibre [128].

Chromatic Aberration

Lens selection is another important consideration in colour scanning systems. Figure 1.22(a) shows a singlet lens refracts different wavelengths at slightly different angles due to material dispersion, resulting in longitudinal chromatic aberration [129]. Each wavelength therefore focuses on a different axial position, producing an extended and blurred focal region when broadband or multi-wavelength illumination is used. In contrast, Figure 1.22(b) shows an achromatic doublet lens, which consists of two elements made from glasses with different dispersions, typically a crown-flint combination. By carefully designing the curvatures and refractive properties of the two elements, the focal positions of multiple wavelengths, for example, red, green, and blue, are brought to the same axial plane, substantially reducing chromatic aberration. This yields a sharper and more uniform focus across the spectral range, which is essential in multi-wavelength scanning systems where precise spatial alignment of each channel is required for accurate imaging and spectral discrimination. Further reduction of focal-point shift can be achieved using achromatic triplets. These operate on the same principle but employ an additional lens element, allowing correction of higher-order dispersion effects and resulting in even lower chromatic aberration. However, such lenses are expensive and difficult to fabricate.

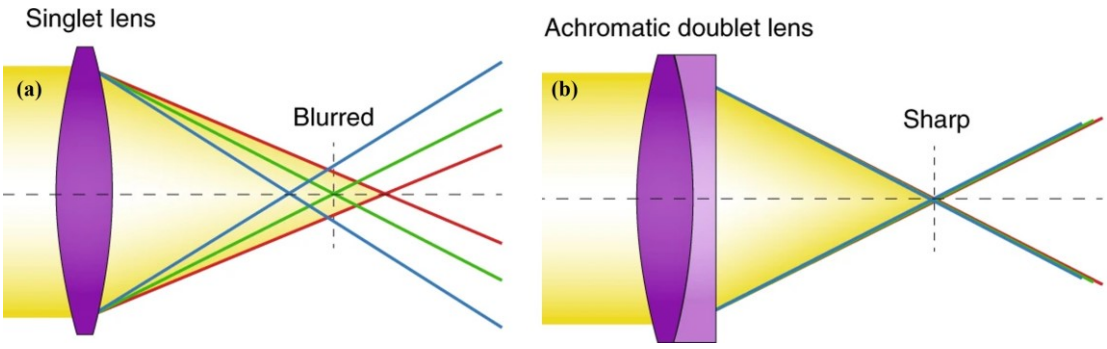


Fig. 1.22 Ray diagrams of (a) singlet lens and (b) achromatic doublet [129].

1.6 Thesis Outline

The discussion above highlights the current difficulties and challenges associated with Lissajous fibre scanners. In summary, the fibre motion cannot be tracked directly because the fibre is made of silica; the fibre motion cannot be actively modified to

follow an ideal Lissajous trajectory, and the scan-line density and frame rate are not programmable. In addition, the existing dip-coating method currently provides insufficient control of the frequency ratio of the two orthogonal bending modes. Finally, there are currently no efficient multi-wavelength scanning systems based on a dual-NA confocal detection mechanism; all existing systems suffer from low optical efficiency.

This thesis addresses these challenges. We present a control solution applicable to many commercially available fibres, which requires only a coated aperture for feedback and electronic circuitry for control. Dip-coating is used to form a composite fibre with a suitable resonant-frequency ratio from a pair of cylindrical fibres [69]. The composite is arranged as a cantilever and excited at 45° to its principal axes. Illumination and detection of backscattered signals are carried out using a dual numerical-aperture confocal scheme [52], with the guided core mode used for illumination and cladding modes used for detection. Feedback signals are generated by a reflecting aperture placed between the cantilever and the lens, which creates timing pulses at the scan extremities [81]. These pulses are amplitude-coded, allowing the feedback signals to be separated by thresholding. The electronics then lock the low- and high-mode drives to the desired frequencies, phases, and amplitudes. Because of the intermittent nature of the feedback and the requirement to generate synchronised drive signals, the controller design is more complex than that of a continuous single-frequency system. However, the relatively low operating frequencies allow standard building blocks, such as digital-to-analogue converters (DACs), VCOs, PLLs, voltage-controlled phase shifters (VCPSs), and frequency dividers, to be used without significant parasitic effects. Care is still required to minimise phase errors, but the result is a programmable locking system that enables a dynamic trade-off between scan-limited resolution and frame rate.

To enable broadband illumination and multi-wavelength mode-stripping detection, a fibre scanner based on endlessly single-mode PCFs is developed. A cantilever is fabricated by a modified dip-coating method to achieve a resonant frequency ratio suitable for Lissajous scanning [69]. Optical feedback is provided by a colour-coded aperture [81], enabling real-time control, and the colour coatings are modified to

support switching between imaging modes. Laser inputs are combined using a wavelength-division multiplexer (WDM), with their current sources controlled by a PC. The output from the WDM is butt-coupled to the PCF, and residual cladding modes are eliminated using a mode stripper. An achromatic doublet is positioned in front of the fibre tip for imaging. The backscattered signal carried by the cladding modes is collected by an RGB photodiode (PD) via an index-matched optical adhesive. Signals from all three channels are transmitted to the controller, with the blue-channel reflection used for real-time control. The colour coatings are designed such that control can operate under either monochromatic blue illumination or broadband illumination.

The remainder of this thesis is organised as follows. Chapter 2 develops the theory for real-time control of 1D and 2D fibre scanners. A tailored apertured mirror is introduced to provide intermittent optical feedback, forming the basis for frequency, phase, and amplitude control. Chapter 3 presents the design and realisation of the real-time controller for 2D Lissajous scanning, including fabrication of the dual-core cantilever, SIMULINK block diagrams, circuit implementation, and the controller initialisation procedure. Controller performance is evaluated with emphasis on nonlinearity, time delay, and stability. Chapter 4 describes the complete optical scanning system. Symmetric Lissajous trajectories and amplitude coding are demonstrated, system misalignments are calibrated and corrected, and image reconstruction is performed under both transient and steady-state conditions. Chapter 5 introduces a PCF-based Lissajous scanner with integrated mode stripping and multi-wavelength detection. The dip-coated dual-cylinder structure is fabricated and characterised, and a 2D scanner is demonstrated using RGB laser sources and a colour-coded aperture. Real-time switching between fluorescence and full-colour imaging is demonstrated and validated using multiple targets and biological specimens. Finally, Chapter 6 concludes the thesis by summarising the contributions and outlining future developments in resolution enhancement, broadband optical feedback, reflective dispersion-free scanning systems, and HC-PBG fibres.

Chapter 2: Fibre Dynamics and Open-Loop Analysis

To control any fibre scanner, feedback signals are required as a reference for the fibre position. Since the fibre itself is typically made of an amorphous material (silica), it is difficult to fabricate any form of integrated sensor. Figure 1.17(b) shows an alternative feedback method based on intermittent optical scattering from an aperture that has been proposed to overcome this difficulty [81]. This aperture is designed for 1D scanning, and the associated software-based controller has very slow convergence. In addition, the aperture doubles the feedback frequency, complicating the controller design. In this Chapter, we first explain how the optical feedback system operates and review the basic control principle for 1D scanning. Optical feedback is then extended to support 2D displacement, and a theoretical framework for the operation and control of a real-time 2D Lissajous fibre scanner is presented. Using the intermittent feedback signals, open-loop analysis for frequency, phase, and amplitude locking is developed for 2D scanning. This analysis provides the foundation for the experimental implementation and system integration for the negative feedback closed-loop controller described in Chapter 3.

2.1 Intermittent Feedback

Figure 2.1 shows the method of generating optical feedback for 1D and 2D scanning. In each case, a metal reflector is used to generate intermittent feedback signals. In Figure 2.1(a), a fibre cantilever is excited by a PT, producing a straight scanning line (red) whose positive extremities reach a metal reflector. Because the reflector has much higher reflectivity than the target, the reflected light (green) is significantly stronger than the backscattered light. This reflected signal is detected by the mode-stripping PD.

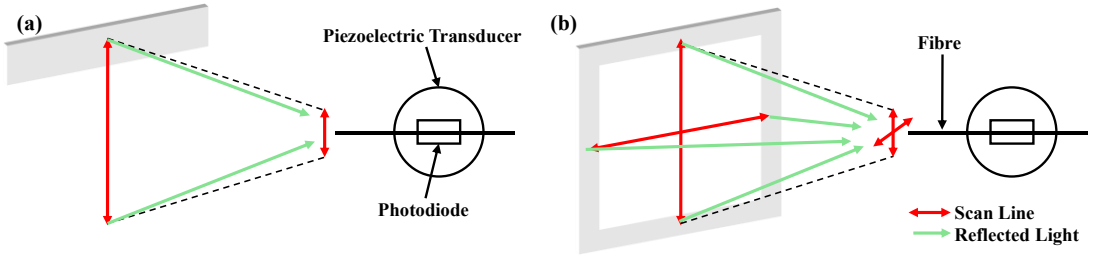


Fig. 2.1 Optical feedback principle for a) 1D and 2D scan control

Figure 2.1(b) shows how this may be extended to 2D scanning using a square aperture. Unlike 1D scanning, two orthogonal motions in the x- and y-directions are excited using a single PT. The reflected feedback signal from both directions is detected by a single PD, which makes it necessary to distinguish between the two contributions to track the 2D fibre position. These challenges are addressed later, after introducing the 1D control theory.

Figure 2.2(a) shows the pulse signal generated from the SIMULINK simulation in Figure 1.4. The driving signal (blue line) excites the fibre cantilever, and the steady-state fibre motion follows the drive with a phase shift. We assume that the half-width of the apertured mirror has a relative value T when compared with the scan amplitude, as indicated by the black dashed line. The illumination beam will clearly be scattered by the aperture back into the fibre whenever the normalised displacement exceeds T, generating feedback pulses (black line). The midpoints of these pulses coincide with the peaks of the fibre displacement, preserving the phase information of the motion. This feedback signal is then passed through low-pass filters to extract the fundamental harmonic component, which is used as a reference for the fibre position.

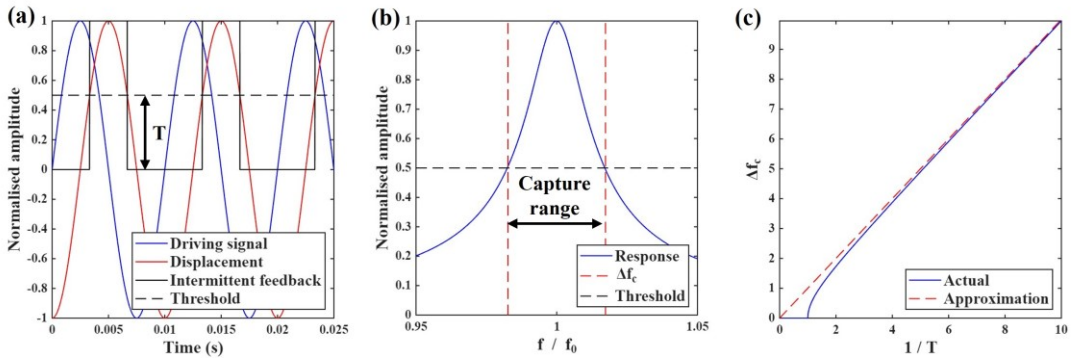


Fig. 2.2 (a) Timing signals in 1D feedback control; (b) amplitude response and capture range ($f_0 = 100Hz,\ \zeta = 0.01,\ T = 0.5$), and (c) capture range versus the inverse of threshold.

Figure 2.2(b) shows the capture range, within which the vibration amplitude of the fibre, calculated from Eqn. (1.17) (blue line), is larger than the threshold T (black dashed line). The frequency range $\Delta f_c = (f_c - f_0)/f_0$ over which intermittent feedback can be generated is referred to as the capture range, as indicated by the red dashed lines. Since the fibre cantilever has a low damping ratio, the cut-off frequency

can be approximated as $f_c \approx f_0$. From Eqns. (1.17) and (1.19), the capture range depends only on the damping ratio ζ and the threshold T, and can be written as:

$$\Delta f_c = \zeta \sqrt{\frac{1}{T^2} - 1} \tag{2.1}$$

Figure 2.2(c) shows this relationship using the blue curve. The capture range increases as the threshold T decreases. When T is larger than the normalised resonant amplitude, intermittent feedback no longer occurs, as indicated by the blue line when $T^{-1} < 1$. For the case $1/T \gg 1$ (i.e., small threshold), the capture range can be approximated by a linear relationship, $\Delta f_c \approx \zeta/T$ as shown by the red dashed line.

2.2 Real-Time Control

In this section, we first introduce the control theory used in the software-based controller for a 1D fibre scanner [81]. The theory is then extended to 2D scanning, where the aperture is modified to support 2D Lissajous fibre scanning. We provide a theoretical explanation to show that the fibre can be driven at a specific frequency ratio, its position can be tracked in real time, and the scanning pattern can be controlled using only the driving signals and intermittent feedback.

2.2.1 1D Control

The control of 1D scanning has two parts: frequency control and amplitude control. For a vibrating cantilever that produces intermittent feedback, the system is first locked to its resonant frequency, and then the amplitude is stabilised to the desired duty cycle.

Frequency Lock

The resonant fibre has a constant 90° phase shift relative to the driving signal. Therefore, when the fibre operates at its resonant frequency, the fibre trajectory can be predicted by applying a 90° phase shift to the drive. In this section, we provide a theoretical explanation to lock the frequency from phase response based on the principles of Costas loops and phase locked loops [88-90].

Figure 2.3 shows the block diagram for open-loop analysis of the frequency lock. The driving signals v are generated from MATLAB across a range of frequencies, which are then passed to the SDE in SIMULINK. The fibre response y is passed through a threshold function in MATLAB to produce the intermittent feedback I. The multiplier will mix the intermittent feedback with the driving signal to generate the multiplier output M, whose DC component is then extracted by an LPF.

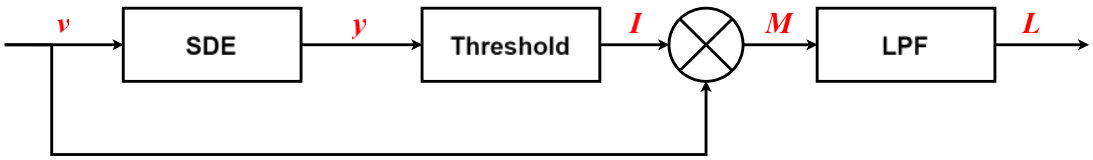


Fig. 2.3 Block diagram for open-loop analysis of frequency lock.

Figure 2.4(a) shows that the fibre displacement (red line) can be treated as a sinusoidal signal whose amplitude and phase depend on the driving frequency, relative to the driving signal (blue line). The driving signal and the fibre displacement can therefore be written as:

$$v(t) = A\sin(2\pi ft) \tag{2.2}$$

$$y(t) = |B(f)|\sin\big(2\pi ft - \phi(f)\big) \tag{2.3}$$

where A is the driving amplitude, $|B(f)|$ is the frequency-dependent displacement amplitude, and $\phi(f)$ is the phase shift between the two signals. The intermittent feedback signal (black line) is generated when the fibre displacement exceeds a threshold. This signal can be approximated using a Fourier series as:

$$I(t) \approx D(f)R + \frac{2R}{\pi}\sum_{N=1}^{\infty}\frac{\sin[D(f)N\pi]}{N}\cos\left[N\left(2\pi ft - \frac{\pi}{2} + \phi(f)\right)\right] \tag{2.4}$$

where R is the reflectivity of the aperture, and $D(f)$ denotes the duty cycle. Since the duty cycle depends on the normalised displacement amplitude and the feedback threshold, and if feedback exists ($T < |B(f)|$), it can be written as:

$$D(f) = \frac{1}{\pi}\cos^{-1}\left(\frac{T}{|B(f)|}\right) \tag{2.5}$$

In Figure 2.4(a), the Fourier approximation (green dashed line) shows excellent agreement with the simulated feedback signal, confirming the validity of the model. Figure 2.4(b) shows the multiplier output $M(t)$ (black line), obtained by mixing the driving signal and the feedback signal. Its Fourier approximation is shown by the green dashed line. When $M(t)$ is passed through a DC-extracting LPF, the signal is:

$$L(f) = \frac{RA}{\pi} \sin[D(f)\pi] \cos[\phi(f)] \tag{2.6}$$

Figure 2.4(c) shows the LPF output as a stable DC value (here, zero). Eqn. (2.6) shows that LPF output is independent of time and depends only on the driving frequency.

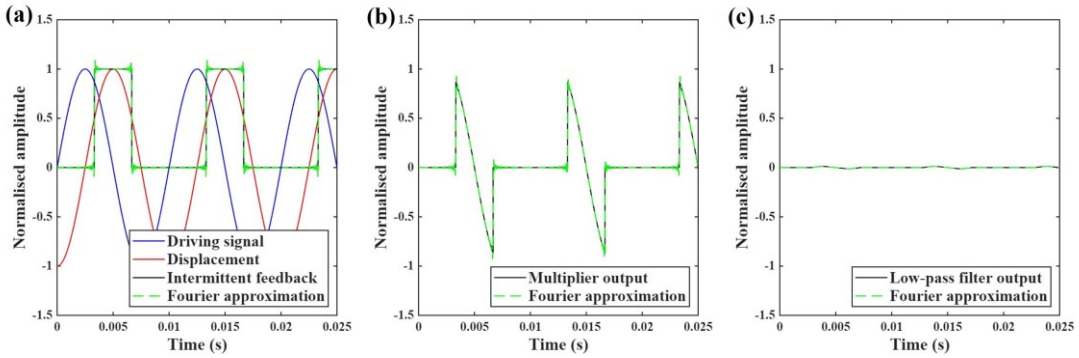


Fig. 2.4 Simulated (a) timing signals, output of (b) the multiplier and (c) the low-pass filter with Fourier approximation.

Figure 2.5(a) shows the variation of the duty cycle defined in Eqn. (2.5). The theoretical result is plotted as a blue line and shows good agreement with the simulation result from SIMULINK (cyan dashed line). In Figure 2.5(a), the term $\sin[D(f)\pi]$ also shows close agreement between the theoretical prediction (red solid line) and the simulation result (green dashed line). Figure 2.5(b) shows the excellent agreement between the theoretical curve (blue solid line) and the simulation (cyan dashed line) of the phase term $\cos[\phi(f)]$, confirming the offset-removal effect of the cosine function. Figure 2.5(c) presents the LPF output after multiplication. The theoretical (blue solid line) and simulated (cyan dashed line) curves overlap almost completely. The multiplier and LPF therefore serve as a phase detector [91-92]. Within the capture range, the LPF response is zero at the resonant frequency. In addition, the output is positive when the driving frequency is below resonance and negative when it is above resonance. This

change in sign with frequency enables the design of a negative feedback controller that can lock the fibre cantilever to its resonant frequency.

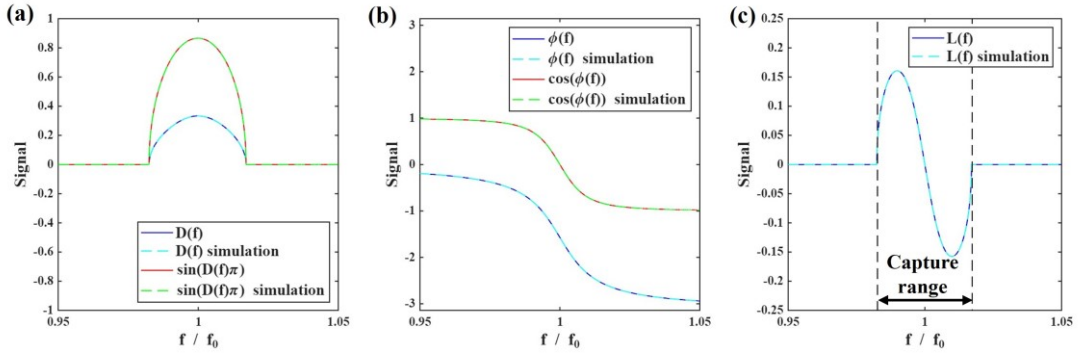


Fig. 2.5 Theoretical and simulated frequency response of (a) duty cycle, (b) phase and (c) low-pass filter output. ($f_0 = 100Hz,\ \zeta = 0.01,\ T = 0.5,\ R = 1$)

Amplitude Lock

After frequency locking, the amplitude of the fibre vibration is controlled to maximise the proportion of light available for backscattering. The intermittent feedback signal consists of pulses that correspond to the extremities of the fibre tip motion. From Eqn. (2.5), the duty cycle of this feedback signal is related to the displacement amplitude. Therefore, by adjusting the duty cycle, the vibration amplitude can be controlled as well. Figure 2.6 shows the block diagram for open-loop analysis of the amplitude lock. Unlike the frequency locker, the intermittent feedback is passed through a LPF directly to extract the DC term DR, which is then divided by R to generate the duty cycles.

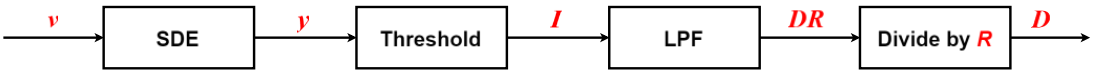


Fig. 2.6 Block diagram for open-loop analysis of amplitude lock.

Figure 2.7(a) shows the extracted term DR when the feedback signal is passed through an LPF. The theoretical result (blue solid line) shows excellent agreement with the Fourier approximation (cyan dashed line). Since the reflectivity of the apertured mirror is known, the duty cycle can be calculated. In Eqns. (2.5), the displacement amplitude is normalised. Assuming that the fibre is locked at its resonant frequency, the relationship between the duty cycle and the driving amplitude is:

$$D(A) = \frac{1}{\pi}\cos^{-1}\left(\frac{2\zeta T f_0^2}{A}\right) \tag{2.7}$$

Figure 2.7(b) shows the relationship between $L(A) = D(A)R$ and the simulation results, with good agreement between theory and simulation. The function is monotonically increasing, which allows a negative-feedback control system to be implemented. Figure 2.7(c) shows the results by passing the LPF output through a differential amplifier with a constant offset $L_0 = D_0 R$. The zero-crossing point, indicated by the black dashed line, corresponds to the driving amplitude at which the fibre cantilever produces intermittent feedback with a duty cycle of D_0.

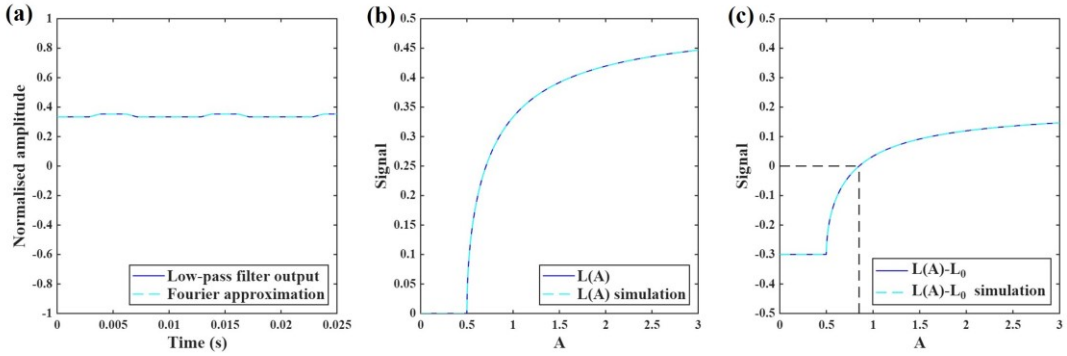


Fig. 2.7 (a) Simulated output of the low-pass filter with Fourier approximation; Theoretical and simulated response of (a) low-pass filter output and (b) differential amplifier output. ($f_0 = 100Hz$, $\zeta = 0.01,\ T = 0.5,\ R = 1,\ L_0 = 0.3$)

2.2.2 2D Control

Unlike 1D scanners, a 2D Lissajous scanner involves vibration in two orthogonal directions at different frequencies. The previous slit aperture is therefore unsuitable, as it cannot generate feedback for both directions. In this section, a new aperture design is introduced, and the control theory developed for 1D scanning is extended to 2D Lissajous scanning. In addition to resonant frequency locking, further theory is presented to generate a symmetric Lissajous pattern with a square FOV.

Fibre Dynamics and Aperture Design

The fibre cantilever must have two separate resonant frequencies that correspond to bending in two perpendicular directions. The structural design and fabrication process used to achieve this is discussed in Chapter 3. In this chapter, we assume that the fibre

has two distinct resonant frequencies with a ratio close to 2. To simplify the analysis, the following assumptions about the fibre dynamics are made:

1. The vertical bending mode has a lower resonant frequency (low mode), while the horizontal bending mode has a higher resonant frequency (high mode).
2. The controller always operates near the resonant frequencies.
3. Both bending modes have low damping ratios.
4. The motions in the two perpendicular directions are completely decoupled.

The low damping ratios are assumed here because we assumed the fibre scanner to operate in air. If the fibre scanners operate in liquid, the damping ratio will increase. For low damping ratios, the resonant peaks of orthogonal bending modes are very narrow so that they can be completely decoupled. However, the narrow high mode resonant peak reduces the selection range of scan line density because the amplitude will decrease significantly off-resonance and will not be able to generate feedback.

The driving signals can be written as cosine functions:

$$v_{h,l}(t) = A_{h,l}\cos\left(2\pi f_{h,l}t\right) \tag{2.8}$$

where $A_{h,l}$ and $f_{h,l}$ are the driving amplitudes and frequencies of the high and low modes, respectively. The two signals are combined using a summing amplifier to generate a dual-frequency excitation for the fibre cantilever. The cantilever is mounted at 45° relative to its principal axes. Because the two modes are decoupled, each mode mainly responds to the driving frequency that is closest to its own resonant frequency. Under harmonic excitation, the fibre cantilever shows the standard second-order complex frequency response for each mode:

$$B_{h,l}\left(f_{h,l}\right) = \frac{A}{f_{h0,l0}^2 - f_{h,l}^2 + 2j\zeta_{h,l}f_{h,l}f_{h0,l0}} \tag{2.9}$$

where $f_{h0,l0}$ are the two resonant frequencies and $\zeta_{h,l}$ are the corresponding damping ratios. The normalised amplitude response and phase response are then given by:

$$Y_{h,l}(f_{h,l}) = \frac{2A\zeta_{h,l}f_{h0,l0}^2}{\sqrt{\left(f_{h0,l0}^2 - f_{h,l}^2\right)^2 + 4{\zeta_{h,l}}^2 f_{h,l}^2 f_{h0,l0}^2}} \tag{2.10}$$

$$\phi_{h,l}(f_{h,l}) = -\tan^{-1}\left(\frac{2\zeta_{h,l}f_{h,l}f_{h0,l0}}{f_{h0,l0}^2 - f_{h,l}^2}\right) \tag{2.11}$$

Figure 2.8(a) shows the phase response by the blue line and its linear approximation in red dashed line. Within the capture range, the phase response is approximately linear. This allows Eqn. (2.11) to be simplified as:

$$\phi_{h,l}(f_{h,l}) = -\frac{\pi}{2} - \frac{f_{h,l} - f_{h0,l0}}{\zeta_{h,l}f_{h0,l0}} \tag{2.12}$$

This linear approximation agrees well with Eqn. (2.11) near resonance.

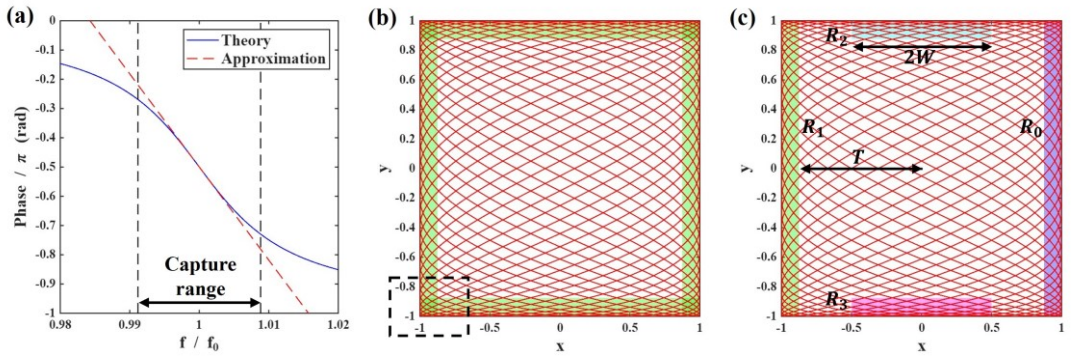


Fig. 2.8 (a) Exact and linearly approximated phase response ($f_0 = 100Hz,\ \zeta = 0.01,\ T = 0.75$); configuration of a (b) conventional and (c) amplitude-coded apertured mirror.

To enable 2D optical feedback, a suitable aperture is required. Figure 2.8(b) shows a previous design in which all four sides have equal reflectivity [69]. This design has two main limitations. First, equal reflectivity produces feedback pulses with the same amplitude, making the signals from different directions impossible to separate. Second, as highlighted by the black dashed box, the fibre displacement reaches its extremities simultaneously at the corners, causing feedback signals to overlap in time. To overcome these problems, Figure 2.8(c) shows a new aperture design. In this design, four reflective regions with different coatings $R_{0,1,2,3}$ are used to create feedback pulses with different amplitudes. This amplitude-coded feedback allows individual signals to be separated using simple level-triggering. As a result, different extremities of the fibre

motion can be selected for different control functions. In addition, the top and bottom reflectors are designed with a width of $2W < 1$, which prevents overlap of the feedback signals in the time domain. The fabrication and experimental implementation of this modified aperture are discussed in the next chapter. The following section explains how this apertured mirror is used for real-time control of the 2D Lissajous fibre scanner and its effect on the overall control theory.

Low-Mode Frequency Lock

Operation of the low-mode frequency lock follows the block diagram shown in Figure 2.3. The low-mode frequency is first locked at its resonant frequency. The normalised fibre displacements of the two modes can be regarded as cosine signals with frequency-dependent phase shifts relative to the driving signals in Eqn. (2.8) as:

$$y_{h,l}(t) = B_{h,l}\cos\left(2\pi f_{h,l}t + \phi_{h,l}\right) \tag{2.13}$$

For frequency locking of the low mode, only the reflector located at the top of the aperture is used (y-reflector). Because the low-mode feedback is limited by the finite width of this reflector, intermittent feedback is only generated under two conditions:

a. The vertical displacement exceeds the positive threshold: $y_l > T$.

b. The horizontal displacement remains within the reflector width: $y_h < |W|$.

The threshold function in MATLAB generates intermittent feedback when both conditions are met. If a unit-amplitude pulse is generated when condition a. is satisfied and remains zero otherwise, a pulse train with the same frequency as the low-mode driving signal is produced. The corresponding duty cycle and its Fourier approximation are given by:

$$D_a(f_l) = \frac{1}{\pi}\cos^{-1}\left(\frac{T}{B_l(f_l)}\right) \tag{2.14}$$

$$F_a(t) \approx D_a + \frac{2}{\pi}\sum_{N=1}^{\infty}\frac{\sin[D_a N\pi]}{N}\cos[N(2\pi f_l t + \phi_l)] \tag{2.15}$$

Similarly, if a unit-amplitude pulse is generated when condition b. is satisfied and remains zero otherwise, a pulse train is produced. Since these pulses occur near the

zero-crossings of the horizontal displacement, two pulses are generated per cycle, resulting in a frequency-doubled signal. The duty cycle and Fourier approximation are:

$$D_b(f_h) = \frac{2}{\pi}\sin^{-1}\left(\frac{W}{B_h(f_h)}\right) \tag{2.16}$$

$$F_b(t) \approx D_b + \frac{2}{\pi}\sum_{M=1}^{\infty}\frac{\sin[D_b M\pi]}{M}\cos\left[2N\left(2\pi f_h t + \phi_H + \frac{\pi}{2}\right)\right] \tag{2.17}$$

Since the low-mode intermittent feedback is generated only when both conditions are satisfied at the same time, the overall feedback signal can be written as the product of Eqns. (2.15) and (2.17), multiplied by the reflector reflectivity:

$$I_l(t) = R_2 F_a(t) F_b(t) \tag{2.18}$$

Following the same procedure as in the 1D case, Eqn. (2.18) is multiplied by the low-mode drive in Eqn. (2.8) and passed through a DC-extracting LPF. The output is then:

$$L_l(f_l) = \frac{R_2 A_l D_b}{\pi}\sin[D_a(f_l)\pi]\cos[\phi_l(f_l)] \tag{2.19}$$

Eqn. (2.19) is analogous to Eqn. (2.6), except for the additional factor D_b, which depends on the reflector width and the high-mode parameters. The key behaviour remains the same: the LPF output L_l becomes zero at the resonant frequency, where $\phi_l = -\pi/2$. Therefore, a closed-loop control system can be constructed to lock the low-mode driving frequency to resonance by forcing L_l to zero.

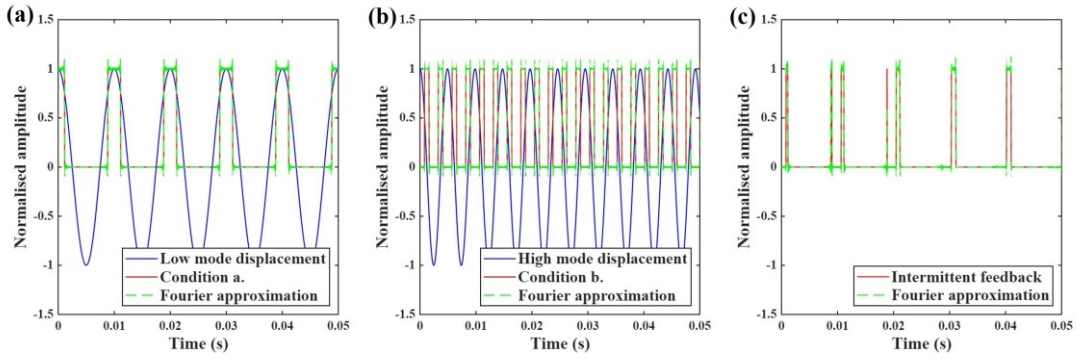


Fig. 2.9 Pulses of (a) condition a., (b) condition b. and (c) low mode intermittent feedback with Fourier approximation. ($W = 0.5,\ T = 0.75$)

Figure 2.9 shows the pulse signals corresponding to condition a., condition b., and the resulting intermittent feedback, together with their Fourier approximations. In

Figure 2.9(a), pulses are generated at the extremities of the low-mode displacement (blue solid line), and the theoretical waveform (red solid line) agrees well with the approximation (green dashed line). In Figure 2.9(b), pulses are generated when the high-mode displacement (blue solid line) remains within the reflector width, again showing good agreement between theory (red solid line) and approximation (black dashed line). After multiplication, Figure 2.9(c) shows the intermittent feedback signal, which appears irregular in the time domain (red solid line). However, it matches the Fourier approximation closely (green dashed line), confirming the validity of the analytical model and demonstrating that the feedback signals can be effectively separated into two independent pulse trains.

High-Mode Frequency Generation

To generate a Lissajous scan pattern, the vibration frequencies must follow the ratio defined in Eqn. (1.24). After the low-mode frequency-locking process above, the low mode operates at its resonant frequency. The high mode must then oscillate at a specific frequency to satisfy this ratio. In practice, it is impossible to construct fibre cantilevers with two resonant frequencies that satisfy this ratio exactly, due to unavoidable fabrication uncertainties. The relationship between the resonant frequencies of the two modes with these uncertainties can therefore be written as:

$$\left(2+\frac{1}{n}\right) f_{l0} = f_{h0} \pm \Delta f_h \tag{2.20}$$

where Δf_h represents the frequency error, and $m = 2$ is assumed. As a result, when the low mode is locked at resonance, the high mode must be driven slightly off resonance. In addition, to allow different values of n to be selected, the high-mode frequency must be adjustable to specific non-resonant values. The high-mode frequency is generated using two identical VCOs, each controlled by a DC voltage. For a VCO, the output frequency is related to the input DC voltage by:

$$f_V = k v_{DC} + f_0 \tag{2.21}$$

where k is the sensitivity of the VCO (determined by the capacitance), and f_0 is the free-running frequency offset. After the low mode is locked, the two VCOs operate as:

$$f_{l0} = kv_{lDC} + f_0 \tag{2.22}$$

$$f_h = f_{h0} \pm \Delta f_h = kv_{hDC} + f_0 \tag{2.23}$$

Combining these expressions gives:

$$v_{hDC} = \left(2 + \frac{1}{n}\right) v_{lDC} + \left(1 + \frac{1}{n}\right) \frac{f_0}{k} \tag{2.24}$$

Therefore, by applying simple scaling and offset operations to the DC control voltages, the high-mode driving frequency can be generated from the low-mode frequency for different values of n. This approach allows flexible control of the scanning line density and frame rate in the Lissajous scanning system.

High-Mode Displacement Estimation

To generate a symmetric Lissajous scan pattern, the fibre trajectory should ideally follow Eqn. (1.23). In practice, phase errors are often introduced due to imperfections in signal generation or system response. When a phase error exists, Eqn. (1.23) becomes:

$$\begin{bmatrix} x \\ y \end{bmatrix} = \begin{bmatrix} \sin(2\pi f_x t + \phi_x) \\ \cos(2\pi f_y t) \end{bmatrix} \tag{2.25}$$

where ϕ_x is the phase error in the x-direction. Figure 2.11(a) shows the effect of this error. When $\phi_x = 0$, the trajectory (black line) is perfectly symmetric. When a phase error of ±6° is introduced, the trajectories (red and blue dashed lines) become asymmetric, leading to mismatched scan points and non-uniform resolution across the FOV. This demonstrates that the Lissajous scanning pattern is highly sensitive to phase errors between the two vibration modes.

Because scan density and symmetry depend strongly on phase, accurate phase control is required. At this stage, the low mode is locked at its resonant frequency and therefore has a fixed phase response. The high mode, however, operates at a non-resonant frequency and has an unknown phase response ϕ_h. There are two main sources of phase error:

1. A phase offset ϕ_V between two VCO-generated driving signals.
2. A phase shift ϕ_h introduced by the non-resonant response of the high mode.

Since the low-mode frequency is already locked, these two effects modify the high-mode driving signal and fibre displacement, which can be written as:

$$v_h(t) = A_h \cos(2\pi f_h t + \phi_V) \tag{2.26}$$

$$y_h(t) = B_h \cos(2\pi f_h t + \phi_V + \phi_h) \tag{2.27}$$

where the aggregate phase error is given by $\phi_x = \phi_V + \phi_h$. To correct this error, the high-mode driving signal should be shifted by $-\phi_V - \phi_h$. In this section, the phase ϕ_h is addressed, while the aggregate phase error ϕ_x is solved later. Because ϕ_h is unknown, the actual fibre displacement cannot be obtained directly from the high-mode driving signal. Instead of calculating ϕ_h explicitly, the high-mode driving signal is phase-shifted by $-\phi_h$ so that it represents the actual fibre motion.

Figure 2.10 shows the block diagram for open-loop analysis of high-mode displacement estimation. The high-mode intermittent feedback I_h is multiplied with the phase-shifted high-mode driving signal v_{hPS}, and the result is passed through a LPF to generate open-loop response L_{hPS}.

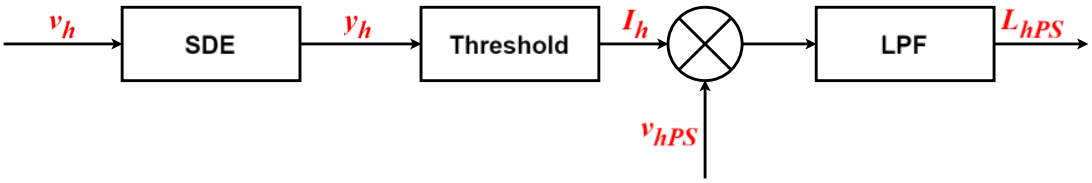


Fig. 2.10 Block diagram for open-loop analysis of high-mode displacement estimation.

Intermittent feedback is generated when the horizontal displacement exceeds the threshold T at the positive extremity, with reflectivity R_0. This produces a pulse train at the same frequency as the high-mode vibration. The duty cycle and Fourier approximation of this feedback signal are given by:

$$D_h(f_h) = \frac{1}{\pi}\cos^{-1}\left(\frac{T}{B_h(f_h)}\right) \tag{2.28}$$

$$I_h(t) \approx R_0 D_h + \frac{2R_0}{\pi}\sum_{N=1}^{\infty}\frac{\sin[D_h N\pi]}{N}\cos[N(2\pi f_h t + \phi_V + \phi_h)] \tag{2.29}$$

Figure 2.11(b) shows the high-mode fibre displacement (blue solid line), the intermittent feedback (red solid line), and its Fourier approximation (green dashed line).

Good agreement is observed between theory and simulation. The high-mode driving signal is then passed through a VCPS implemented using all-pass filters. The phase shift is controlled by a voltage-controlled resistor (VCR), enabling closed-loop phase adjustment. The phase-shifter range is set from -2π to 2π, which covers the expected range of ϕ_h from 0 to $-\pi$. The phase-shifted driving signal is:

$$v_{hPS}(t) = A_h \cos(2\pi f_h t + \phi_V + \phi_{hPS}) \tag{2.30}$$

where ϕ_{hPS} is the applied phase shift. By multiplying Eqn. (2.30) with the intermittent feedback signal in Eqn. (2.29) and passing through a DC-extracting LPF, we get:

$$L_{hPS}(\phi_{hPS}) = \frac{R_0 A_h}{\pi} \sin[D_h \pi] \cos[\phi_{hPS} - \phi_h] \tag{2.31}$$

The LPF output converges to zero when $\phi_{hPS} - \phi_h = \pi/2$. This allows a closed-loop control system to be implemented that maintains a constant $\pi/2$ phase difference between the phase-shifted driving signal and the actual fibre motion. After integration, DC removal, and inversion, the estimated high-mode fibre displacement is obtained as:

$$v_{hE}(t) = \frac{A_h}{2\pi f_h} \cos(2\pi f_h t + \phi_V + \phi_h) \tag{2.32}$$

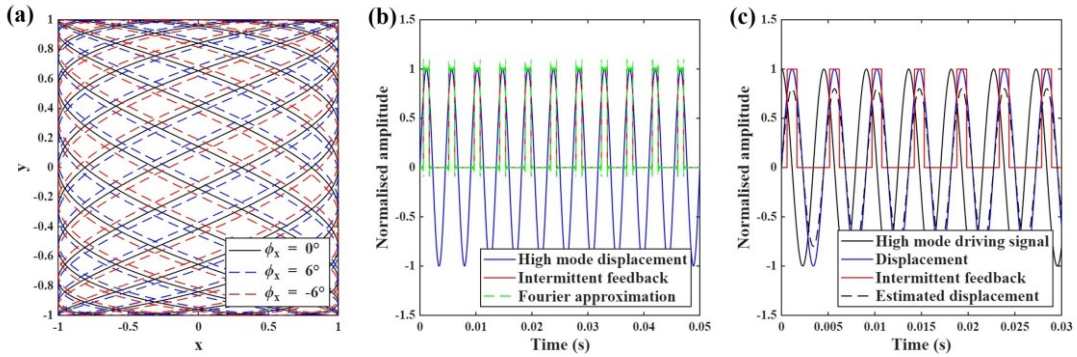


Fig. 2.11 (a) Lissajous scanning pattern with and without phase error; (b) high mode intermittent feedback with Fourier approximation; and (c) timing signals for high mode fibre displacement estimation. ($T = 0.75$)

Figure 2.11(c) shows that the estimated displacement (black dashed line) aligns closely with both the intermittent feedback (red solid line) and the actual fibre motion (blue solid line). The detailed SIMULINK block diagram for this control loop will be shown in the next Chapter. Although Eqns. (2.32) and (2.27) differ in amplitude, their frequency and phase components are identical. Therefore, the estimated signal can be

used as a reliable reference for the high-mode displacement. In the following analysis, the amplitude term is omitted for clarity, although it is retained in the equations to remain consistent with the actual controller design.

Phase Synchronisation

With the 2D fibre motion now tracked in real time, the remaining task is to correct the phase difference between the driving signals generated by the two VCOs. Because the two vibration modes operate at different frequencies, it is not possible to maintain a fixed phase relationship directly. To address this, we exploit the repetitive nature of the Lissajous scanning pattern. Due to its periodicity, the scan trajectory repeats itself with a period of n/f_{l0} and passes through the same points in each cycle. If the time at which the trajectory passes through a specific point is known, the entire trajectory can be determined. If the scan passes through the point (0,1) at a certain time t_0, the resulting trajectory is symmetric for all subsequent times. By defining $\tau = t - t_0$, the motion of the fibre tip can then be expressed as:

$$\begin{bmatrix} x \\ y \end{bmatrix} = \begin{bmatrix} \sin(2\pi f_h \tau) \\ \cos(2\pi f_{lo} \tau) \end{bmatrix} \tag{2.33}$$

The goal is therefore to adjust the driving signals so that the fibre passes through the point (0,1) at the same time, which corrects the phase error between the two VCOs. For the motion described by Eqn. (1.23), the trajectory passes through (0,1) at $t = 0$. Since the low mode is locked at its resonant frequency with a fixed phase, the zero-crossings of the low-mode drive coincide with the extrema of the fibre displacement. As a result, within each cycle, a pair of zero-crossings from the low-mode drive and the high-mode displacement should occur at the same time. Conversely, if these zero-crossings are aligned, the resulting Lissajous trajectory is symmetric. To achieve this, both signals are converted into square waves whose edges correspond to their zero-crossings. These square waves are then synchronised to correct the phase between the two driving signals.

Figure 2.12 shows the block diagram for open-loop analysis of phase synchronisation. The estimated high-mode displacement v_{hE} and the phase-shifted low-mode driving signal v_{lPS} are passed through triggers with active high and low to

generate square waves S_h and S_l. These waves are divided to S_{hFD} and S_{lFD} with a common frequency (CF). The low-mode frequency-divided square wave is DC-removed, integrated, and multiplied with the high-mode frequency-divided square. The output is passed through a LPF to produce the open-loop response L_{lPS}.

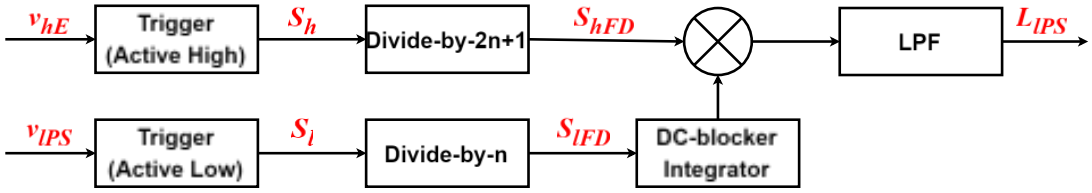


Fig. 2.12 Block diagram for open-loop analysis of phase synchronisation.

The low-mode drive from Eqn. (1.23) can be written as:

$$v_l(t) = A_l \cos\left(2\pi f_{l0} t + \frac{\pi}{2}\right) \tag{2.34}$$

Figure 2.13(a-b) show the resulting signals if the x-displacement is converted into an active-low square wave with a trigger level at zero, and the y-displacement in Eqn. (1.23) is converted into an active-high square wave. The rising edges of the two square waves (black solid lines) occur at the same time $t = 0$. Based on this observation, an ideal and symmetric Lissajous curve can be generated by ensuring that one pair of rising edges from these two square-wave signals is aligned in time.

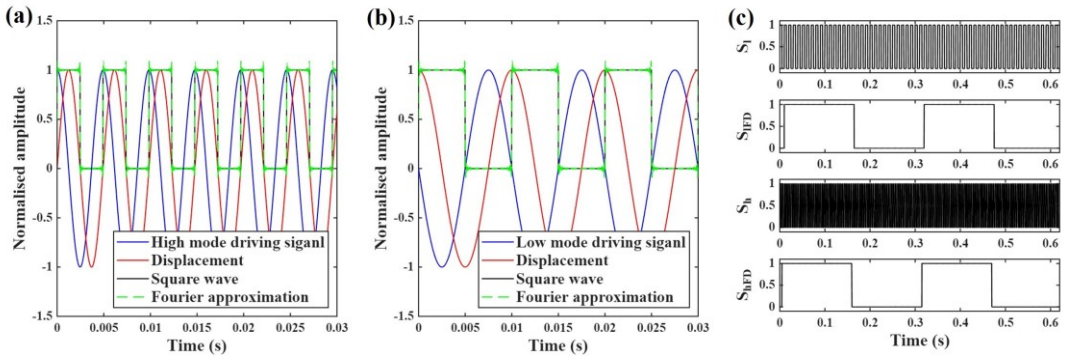


Fig. 2.13 Square wave generation for (a) high mode and (b) low mode with Fourier approximation; (c) frequency divided square waves for two modes.

We now define the expressions of the square waves shown in Figure 2.13(a-b) and describe how their rising edges can be aligned. These signals are expressed as:

$$S_l(t) \approx \frac{1}{2} + \frac{2}{\pi}\sum_{N=1}^{\infty}\frac{\sin\left[\frac{N\pi}{2}\right]}{N}\cos\left[N\left(2\pi f_{l0}t - \frac{\pi}{2}\right)\right] \tag{2.35}$$

$$S_h(t) \approx \frac{1}{2} + \frac{2}{\pi}\sum_{M=1}^{\infty}\frac{\sin\left[\frac{M\pi}{2}\right]}{M}\cos[M(2\pi f_h t + \phi_V + \phi_h)] \tag{2.36}$$

where $S_l(t)$ and $S_h(t)$ represent the square waves of the low and high mode, respectively. Because the two modes operate at different frequencies, the time intervals between their rising edges are not constant. This problem can be solved using a positive-edge-triggered frequency divider. The divider is triggered simultaneously by the first pair of rising edges from both signals and then divides the frequencies by n and $2n + 1$, respectively. As a result, two new square waves are produced that preserve their original phase relationship while sharing the same frequency f_{l0}/n. The implementation of this frequency-division scheme and the programmable selection of different values of n are discussed in Chapter 3. Here, we introduce the basic principle.

Figure 2.14 shows the configuration of the divide-by-N frequency divider [96-97], and Figure 2.15 shows the simulated signals from a divide-by-3 divider. This design achieves odd frequency division with a 50% duty cycle by the following steps:

1. Input: The input square wave is shown in the first row of Figure 2.15.
2. Counters: Counter (0) generates pulses at 0, as shown in the second row, and Counter (N−1) generates pulses when the count reaches N−1. For the divide-by-3 example, the counter sets after reaching 2, as shown in the third row.
3. Flip-Flops: The input (rising edge triggered) and Counter (0) (active-low) are connected to Flip-Flop 1 (FF1) to produce the waveform in the fourth row. Similarly, the input (falling edge triggered) and Counter (N−1) (active-high) are connected to Flip-Flop 2 (FF2), generating the waveform in the fifth row.
4. Output: The signals from FF1 and FF2 are combined using an XOR gate to generate the frequency-divided output, as illustrated in the sixth row.

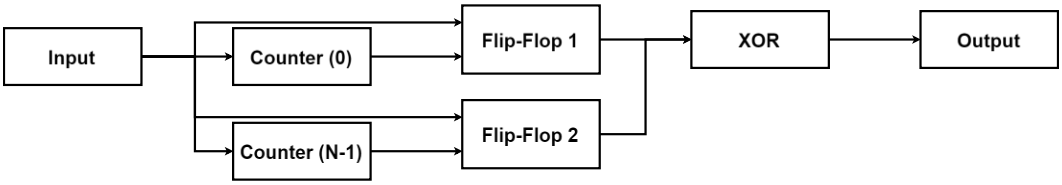


Fig. 2.14 Configuration of divide-by-N frequency divider.

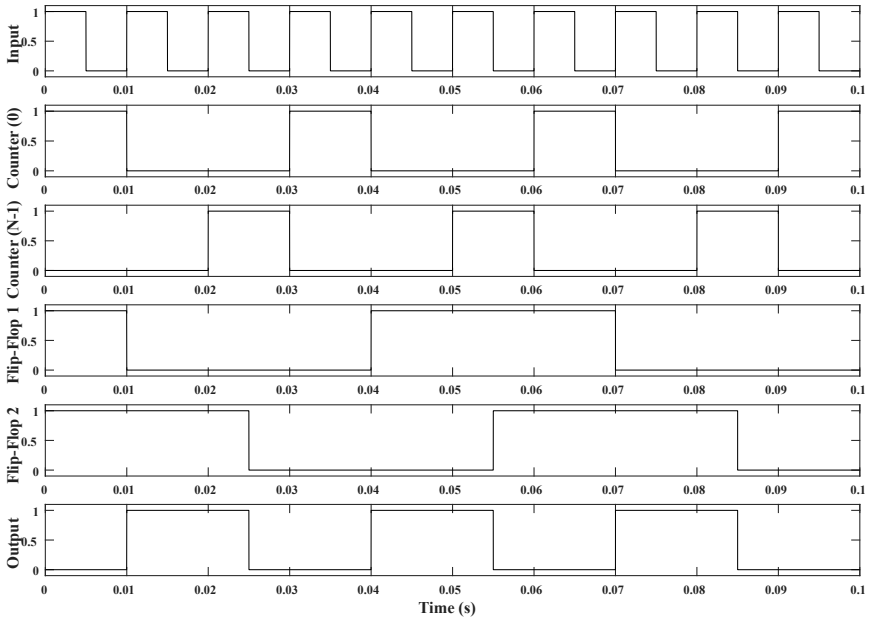


Fig. 2.15 Simulated signals of a divide-by-3 frequency divider.

This circuit produces a stable 50% duty cycle for odd-integer frequency division, making the output signals suitable for phase synchronisation in the real-time control system. Figure 2.13(c) shows that after applying frequency division to Eqns. (2.35-2.36), two square waves from the two modes, S_{lFD} and S_{hFD}, are generated with the same frequency. The original square waves, shown in the first and third rows, are divided to obtain the signals displayed in the second and fourth rows, respectively.

We now align the rising edges of the frequency-divided square waves. From Figure 2.13(c), although the phase in Eqns. (2.35-2.36) is preserved after frequency division, they are affected by the trigger of the FFs. Since each FF produces an output only after completing one full input cycle, the output signal is delayed by one period. As a result, even when both dividers are triggered at the same time, the first rising edge of the low-mode signal may appear later than that of the high-mode signal. This causes the relative phase between the two signals to vary over a wide range, from $-2(2+1/n)\pi$ to 2π. Because phase is a relative quantity, the low-mode signal can be phase-shifted to reduce

the range of phase error that needs to be corrected. This simplifies the circuit design. The corresponding phase conversion relationship is given by:

$$\phi_l = -\frac{n}{2n+1}(\phi_V + \phi_h) \tag{2.37}$$

which reduces the phase error range to $-n\pi/(2n+1)$ to 2π. The frequency divided square waves corresponding to Eqns. (2.35-2.36) can thus be written as:

$$S_{lFD}(t) \approx \frac{1}{2} + \frac{2}{\pi}\sum_{N=1}^{\infty}\frac{\sin\left[\frac{N\pi}{2}\right]}{N}\cos\left[N\left(2\pi\frac{f_{l0}}{n}t - \frac{2\pi}{n} - \frac{\pi}{2}\right)\right] \tag{2.38}$$

$$S_{hFD}(t) \approx \frac{1}{2} + \frac{2}{\pi}\sum_{M=1}^{\infty}\frac{\sin\left[\frac{M\pi}{2}\right]}{M}\cos\left[M\left(2\pi\frac{f_{l0}}{n}t - \frac{\phi_l}{n} - \frac{3\pi}{4n+2} - \frac{\pi}{2}\right)\right] \tag{2.39}$$

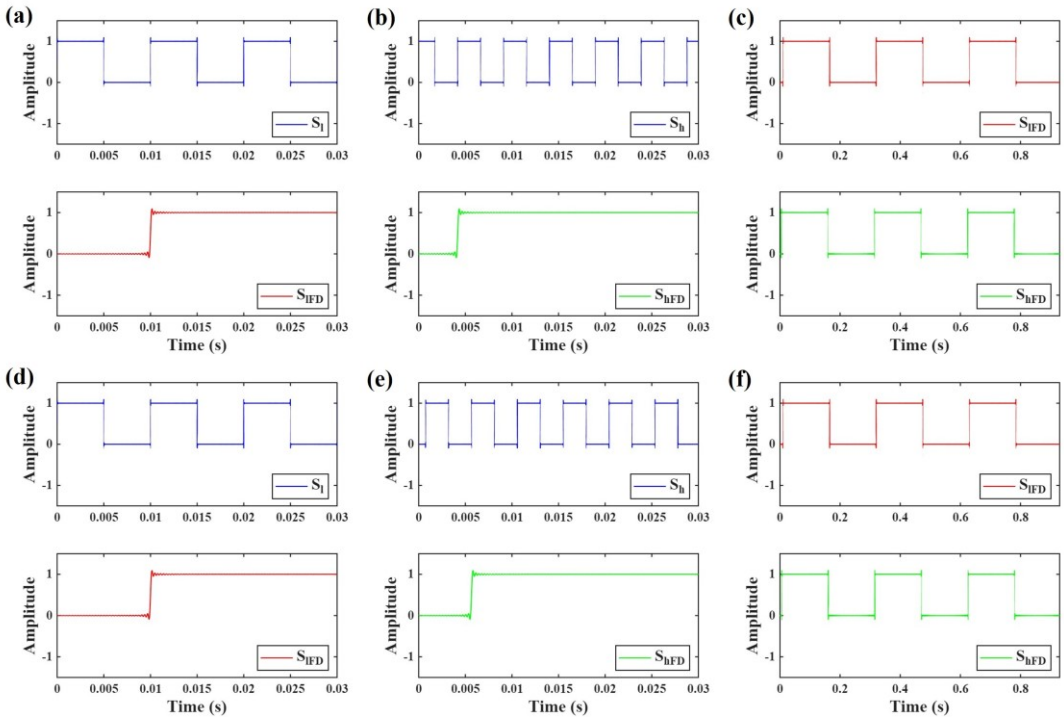


Fig. 2.16 Square wave and frequency divided square wave of (a, d) low mode and (b, e) high mode at the start and (c, f) frequency divided square waves for 3 complete cycles with (a-c) $\phi_V + \phi_h = -0.4\pi$ and (d-f) $\phi_V + \phi_h = -0.6\pi$.

Figure 2.16 shows the original square waves and their frequency-divided counterparts for different phase errors. From Figures 2.16(a-b) and (d-e), after phase calibration during the frequency-division process, the rising edges of the low- and high-

mode square waves are aligned. Figures 2.16(c) and (f) show that the frequency-divided square waves have the same frequency even when different phase errors are present.

We now apply a phase shift to the low-mode drive so that the frequency-divided square waves in Eqns. (2.38-2.39) are aligned. The output of the VCPS is:

$$v_{lPS}(t) = A_l \cos\left(2\pi f_{l0} t + \phi_{lPS} + \frac{\pi}{2}\right) \tag{2.40}$$

where ϕ_{lPS} is the applied phase shift. With this phase shift, Eqn. (2.38) becomes:

$$S_{lFD}(t) \approx \frac{1}{2} + \frac{2}{\pi}\sum_{N=1}^{\infty} \frac{\sin\left[\frac{N\pi}{2}\right]}{N} \cos\left[N\left(2\pi \frac{f_{l0}}{n} t + \frac{\phi_{lPS}}{n} - \frac{2\pi}{n} - \frac{\pi}{2}\right)\right] \tag{2.41}$$

To generate the required 90° phase shift for locking, the DC component of Eqn. (2.41) is removed, and the signal is integrated to produce a triangular wave. By mixing this triangular wave with Eqn. (2.39) and passing the result through an LPF, the output is:

$$L_{lPS}(\phi_{lPS}) = -\frac{n}{\pi^3 f_{l0}} \sum_{N=1}^{\infty} \frac{\sin^2\left[\frac{N\pi}{2}\right]}{N^3} \sin\left[N\left(-\frac{\phi_l}{n} - \frac{3\pi}{4n+2} - \frac{\phi_{lPS}}{n} + \frac{2\pi}{n}\right)\right] \tag{2.42}$$

When the sine functions become zero, the LPF output converges to zero. This allows a closed-loop system to lock ϕ_{lPS}. The corresponding phase shift is given by:

$$\phi_{lPS} = 2\pi - \phi_l - \frac{3\pi}{2}\frac{n}{2n+1} \tag{2.43}$$

The fibre displacements of the two modes can then be written as:

$$y_l(t) = B_l \cos\left(2\pi f_{l0} t - \phi_l - \frac{3\pi}{2}\frac{n}{2n+1}\right) \tag{2.44}$$

$$y_h(t) = B_h \cos\left(2\pi f_h t - \frac{2n+1}{n}\phi_l\right) \tag{2.45}$$

In Eqns. (2.44-2.45), the conditions $y_l = 1$ and $y_h = 0$ are met simultaneously at,

$$t = \frac{\phi_l + \frac{3\pi}{2}\frac{n}{2n+1}}{2\pi f_{l0}} \tag{2.46}$$

This shows that the fibre displacements of the two modes pass through the point (0,1) simultaneously. We can therefore conclude that the resulting motion forms a symmetric Lissajous scanning pattern.

Amplitude Control

At this stage, the low mode is locked at its resonant frequency, and the high mode frequency is locked to maintain the fixed ratio required for Lissajous scanning. Phase errors have also been corrected. We now focus on amplitude control of the fibre displacements. In practice, setup errors can affect the performance of amplitude control. Here, ideal alignment is assumed. Amplitude control serves two main purposes:

1. To ensure a square FOV.
2. To maximise the proportion of backscattered light relative to reflected light.

The duty cycle can be obtained from Eqns. (2.19) and (2.29) by passing the feedback signals through a DC-extracting LPF and dividing the output by the reflectivity. While the high-mode duty cycle is given in Eqn. (2.28), the low-mode duty cycle is:

$$D_l(f_l) = \frac{2}{\pi^2}\cos^{-1}\left(\frac{T}{B_l(f_l)}\right)\sin^{-1}\left(\frac{W}{B_h(f_h)}\right) \tag{2.47}$$

Since the high mode operates close to resonance, we can approximate $B_l \approx 1$. When the amplitudes in the two orthogonal directions are equal, the ratio of the duty cycles is:

$$\frac{D_l}{D_h} = \frac{2}{\pi}\sin^{-1}(W) \tag{2.48}$$

which is a constant value. In practice, the duty cycle in one direction is actively controlled according to Eqn. (2.7), while the duty cycle in the orthogonal direction is locked to the value defined by Eqn. (2.48). This approach ensures a square FOV and allows the target duty cycle to be set to a relatively low value, thereby maximising the proportion of backscattered signals and improving overall optical efficiency.

2.3 Conclusion

An intermittent feedback mechanism was used to provide a reference for the fibre displacement, and an amplitude-coded aperture was introduced for the real-time control of 2D Lissajous fibre scanners. The frequency- and amplitude-locking schemes previously developed for a 1D fibre scanner were reviewed and extended to the 2D Lissajous scanner using this modified aperture. The low-mode frequency was locked

using its constant phase response at resonance, while the non-resonant high-mode frequency was generated using two VCOs driven by DC control voltages. The high-mode displacement was estimated using a phase-shifted driving signal, and the two vibration modes were synchronised using frequency dividers to produce a symmetric Lissajous scanning pattern. Finally, a square FOV was achieved by maintaining a fixed ratio between the duty cycles of the two modes. Overall, this chapter establishes an open-loop theoretical foundation for the design of a real-time negative feedback closed-loop controller for 2D Lissajous fibre scanners and provides the basis for the experimental implementation described in the following chapters.

Chapter 3: Real-Time Controller

This chapter presents the design of a real-time controller for a 2D Lissajous fibre scanner. The chapter introduces the closed-loop controller design, which is based on Costas loops and PLLs [88-92]. SIMULINK models are developed, and each functional block is explained with reference to the theoretical controller design. The dip-coating [69] process is used to produce a cantilever suitable for generating a symmetric Lissajous scanning pattern. The experimental real-time controller and its initialisation procedure are then described, including the circuit implementation and the role of each hardware component. Finally, the theoretical, simulated, and experimental performances of both open- and closed-loop systems are analysed using nonlinear delayed differential equations (NDDEs) [130-131]. The controller performance is evaluated in terms of non-linearity, time delay, and critical gain.

3.1 Controller Design

In Chapter 2, the theoretical analysis showed that a real-time controller can be designed for a 2D Lissajous fibre scanner to generate a symmetric and square FOV. In this section, the controller design for five subsystems is introduced, including low-mode frequency locking, high-mode frequency generation, high-mode displacement estimation, phase synchronisation, and amplitude control. Figures 3.1-3.5 show the block diagrams of these five subsystems, illustrating the basic structure of the overall controller. The aim of this section is to demonstrate that each subsystem can operate as required, rather than to describe detailed hardware implementation. Based on these theoretical block diagrams, corresponding simulation models and experimental setups are developed, with additional consideration of practical, real-world effects.

Figure 3.1 shows the block diagram of the low-mode frequency lock subsystem, which uses a Costas loop [88-92] to lock the frequency based on the phase difference. A DC control voltage is applied to a VCO to generate the driving signal v_l, which excites the scanner and produces the corresponding displacement y_l. The reflecting aperture provides intermittent optical feedback, from which the level trigger extracts

the low mode feedback signal I_l based on reflectivity variations. A multiplier combines the driving and feedback signals, and its output is processed by a LPF that extracts the DC component containing the phase information L_l. The LPF output is then integrated and fed back to a subtractor to form a negative-feedback integral control loop. As the LPF output converges to zero when the low mode reaches its resonant frequency, this subsystem effectively locks the low mode oscillation to resonance.

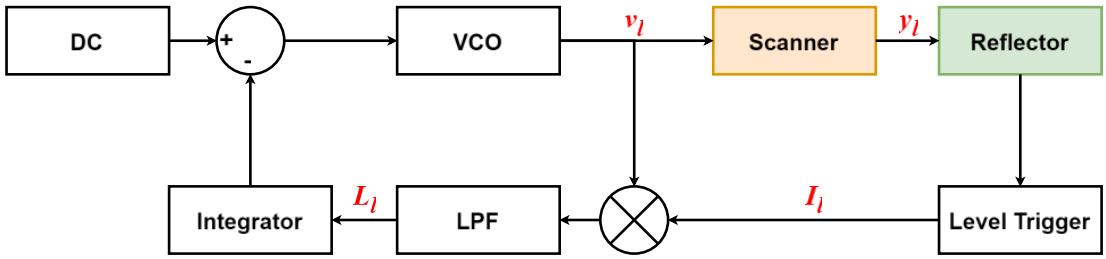


Fig. 3.1 Block diagram for low-mode frequency lock.

Figure 3.2 shows the block diagram of the high mode frequency generation subsystem. Once the low-mode frequency lock is established, the control voltage v_{lDC} drives the upper VCO to generate a sinusoidal excitation signal at the low mode resonant frequency f_{l0}. This voltage is then multiplied by a factor of $2 + 1/n$ and summed with a voltage corresponding to $(1 + 1/n)\, f_0/k$, in accordance with the relationship defined in Eqn. (2.24), to produce the high mode frequency f_h from the lower VCO. The VCO sensitivity and free-running frequency should be measured in advance to set the voltage. By adjusting these control voltages, the value of n can be varied, thereby enabling programmable control of the scan-line density and frame rate.

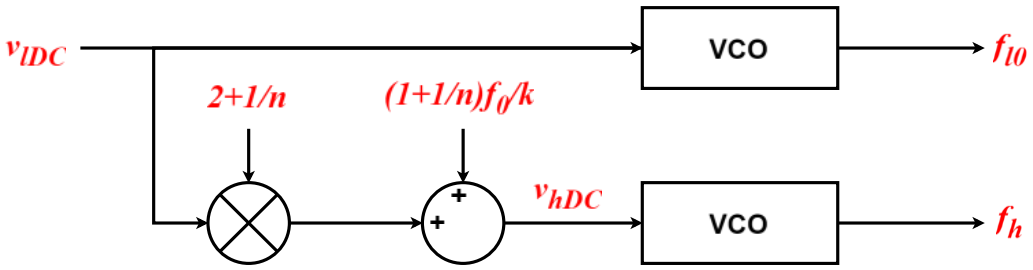


Fig. 3.2 Block diagram for high-mode frequency generation.

Figure 3.3 shows the block diagram of the high mode displacement estimation subsystem. The high mode drive v_h generated by a VCO excites the scanner,

producing a high mode displacement y_h. The intermittent feedback from the reflector is processed by a level trigger to extract the high mode feedback I_h. The high mode drive is then passed through a phase shifter (PS) to generate v_{hPS}, which is multiplied by the feedback signal and filtered through a LPF to extract the DC phase term L_{hPS}. Together with an initial bias voltage for the PS, the LPF output passes through an integrator and subtractor to form a negative-feedback integral control loop. The loop converges when the phase difference between the high mode displacement and the phase-shifted driving signal approaches 90°. Subsequently, the integrator and a DC blocker compensate for this 90° phase shift, producing the estimated high-mode displacement v_{hE}, which shares the same phase component as the actual displacement.

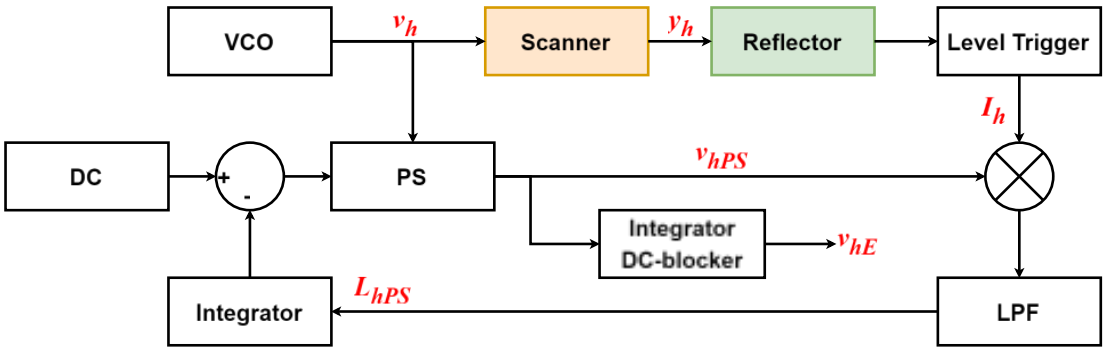


Fig. 3.3 Block diagram for high-mode displacement estimation.

Figure 3.4 shows the block diagram of the phase synchronisation subsystem. The estimated high mode displacement v_{hE} is first processed by an active-high trigger to generate the high mode square wave S_h, which is then passed through a divide-by-$(2n+1)$ frequency divider to produce the signal S_{hFD}. Meanwhile, the low mode driving signal v_l from the VCO is passed through a PS to obtain the phase-shifted signal v_{lPS}. An active-low trigger converts this signal into the low mode square wave S_l, which is subsequently divided by n using a frequency divider to produce S_{lFD}. The divided signal is passed through a DC blocker and an integrator to generate the triangular waveform T_{lFD}. This triangular wave is then multiplied by the high mode divided square wave, and the resulting signal is low pass filtered to extract the phase information L_{lPS}. An integrator and a subtractor, together with a DC control voltage

applied to the PS, form a closed-loop control system that drives the LPF output towards zero, thereby synchronising the two frequency-divided square waves.

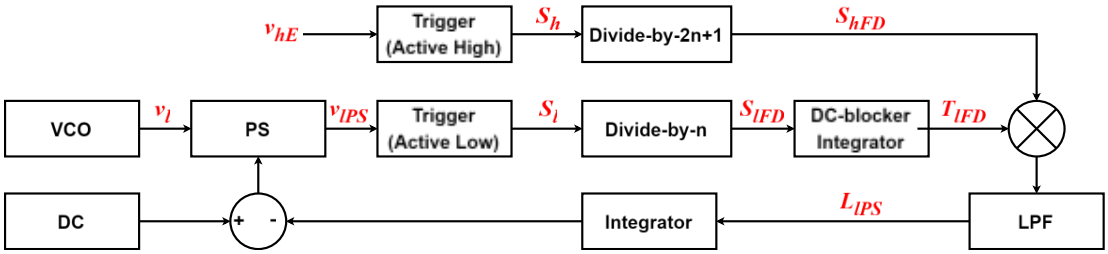


Fig. 3.4 Block diagram for phase synchronisation.

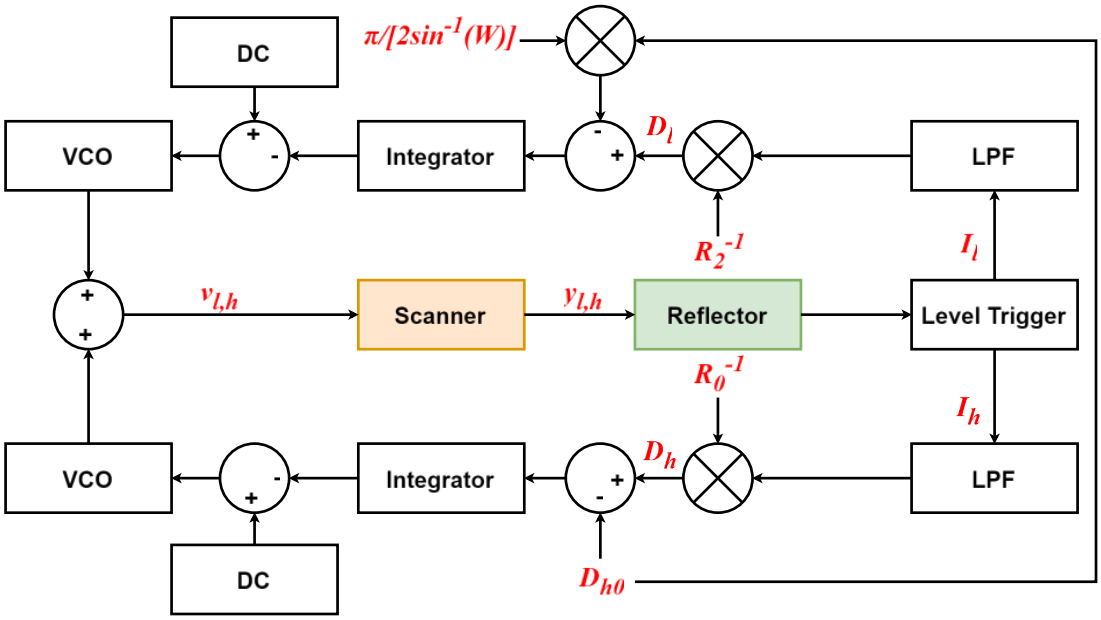


Fig. 3.5 Block diagram for amplitude control.

Figure 3.5 shows the block diagram of the amplitude control subsystem. The driving signals for the two vibration modes, generated by two VCOs, are combined to form a dual-frequency excitation signal $v_{l,h}$, which drives the PT to excite the scanner and produce the corresponding displacements $y_{l,h}$. The reflector, together with the level trigger, provides intermittent feedback signals for the low and high modes, denoted as I_l and I_h, respectively. LPFs and multipliers, with the other inputs being the inverse of the reflectivity, are used to derive the duty cycle values D_l and D_h. For the high mode, a subtractor referenced to a constant voltage D_{h0}, followed by an integrator, forms a closed-loop control system that adjusts the amplitude of the high mode driving signal to maintain a constant duty cycle. To achieve a square FOV, the

low mode duty cycle is compared with a constant input corresponding to the ratio $\pi/[2\sin^{-1}(W)]$. The subsequent subtractor and integrator constitute another closed-loop controller that regulates the amplitude of the low mode driving signal, ensuring that the duty cycle is locked at the desired value and the resulting FOV remains square.

3.2 Simulation Setup

Based on the subsystem block diagrams, corresponding simulation models are developed in SIMULINK, a block-based environment for simulating and analysing multi-domain systems. In this section, the simulation models of the key subsystems are presented to support the design of the experimental controller circuits. The high-mode frequency generation subsystem is not included in the simulation, because its behaviour is defined by analytical relationships and does not require dynamic modelling.

Figure 3.6 shows the SIMULINK model of the low-mode frequency lock subsystem, which consists of 13 components. Moving anticlockwise around the loop, these include three constant blocks, a summing block, a gain block, a low-mode VCO, a high-mode VCO, a scanner, a reflector, a phase detector, a clock, a switch, and an integrator. The internal structures of the main sub-blocks, including the VCOs, the reflector, and the phase detector, are shown in Figure 3.7. The simulation is carried out with the low mode initially operating off resonance, while the amplitudes of both vibration modes are set high enough to produce detectable feedback signals.

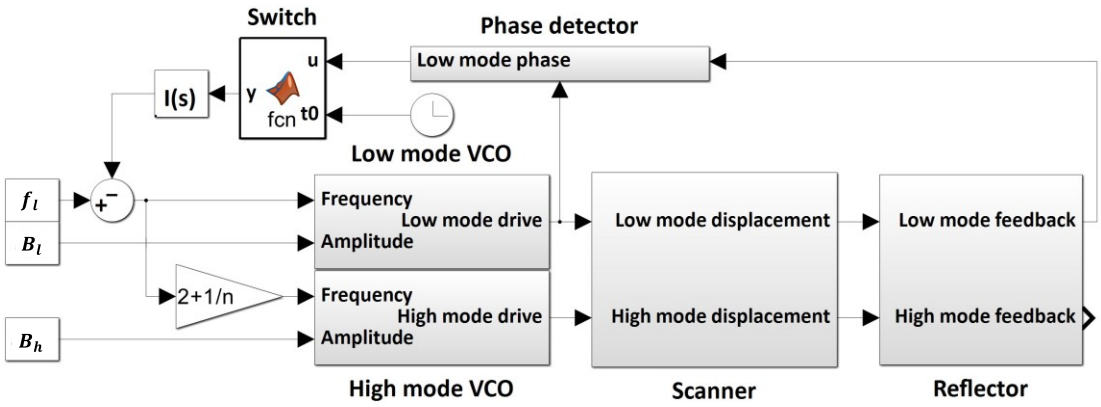


Fig. 3.6 SIMULINK model for low-mode frequency lock.

The first constant sets the initial low-mode frequency, which is chosen to be off resonance. The second and third constants define the amplitudes of the driving signals. The summing block provides negative feedback for the control loop. The gain block, with a value of $2 + 1/n$, sets the required relationship between the low- and high-mode frequencies for Lissajous scanning. Figure 3.7(a) shows the low-mode VCO, which takes the frequency and amplitude as inputs and generates a sinusoidal driving signal. The high-mode VCO has the same structure. The scanner models the fibre motion using a SDE with fixed damping ratios and resonant frequencies, as shown in Figure 1.4. Since the two vibration modes are assumed to be decoupled, the high-mode displacement is treated independently. Figure 3.7(b) shows the reflector, which is implemented as a MATLAB function. Its inputs are the low-mode displacement, high-mode displacement, width, threshold, and reflectivity. The width and threshold are chosen to ensure that feedback is generated, while the reflectivity sets the amplitude of the low-mode feedback signal. Figure 3.7(c) shows the phase detector, which consists of a multiplier followed by a second-order Butterworth LPF with a cutoff frequency of 2 Hz. The clock records the simulation time, and the switch, implemented as a MATLAB function, defines when the control loop is activated. Finally, the integral controller is implemented using an integrator to provide the feedback action.

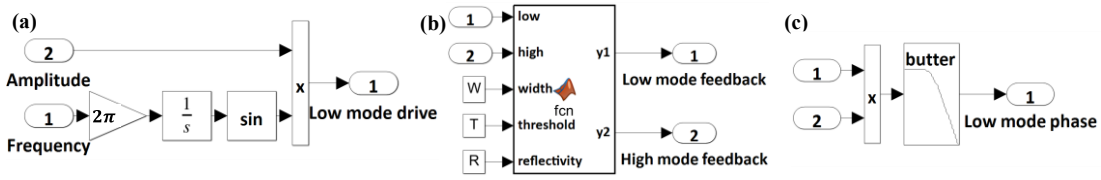


Fig. 3.7 SIMULINK sub-blocks for model in Figure 3.6.

Figure 3.8 shows the SIMULINK model of the high-mode displacement estimation subsystem, which consists of 16 components. Moving clockwise, these include three constants, a gain, a low mode VCO, a high mode VCO, a scanner, a reflector, a phase detector, a clock, a switch, an integral controller, a 90° PS, a variable time delay, a summing block, and an initial delay. Most of the components have been described previously. Figure 3.8 shows the configuration of the 90° PS. The simulation is carried out under the following conditions: the low mode operates at resonance, the high mode

is non-resonant, and the driving signal amplitudes are large enough to generate feedback. The key element in this model is the variable time-delay block, which introduces a controllable delay to the high-mode driving signal. The initial delay is used to represent the phase-lead and phase-lag behaviour of the phase shifter. Figure 3.8 shows that the 90° PS integrates the input signal and removes the DC offset using a summing block and a Butterworth LPF, thereby producing a zero-phase output.

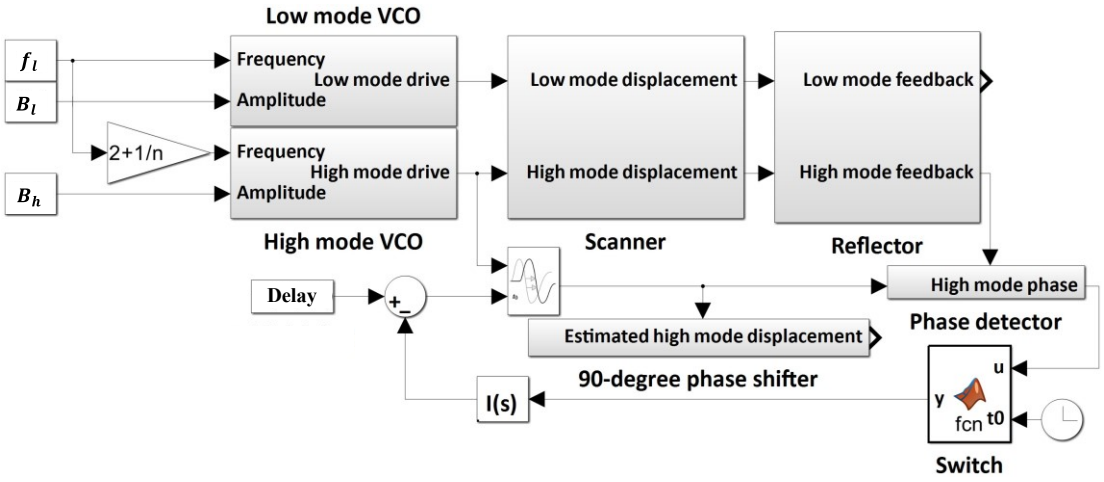


Fig. 3.8 SIMULINK model of high-mode displacement estimation.

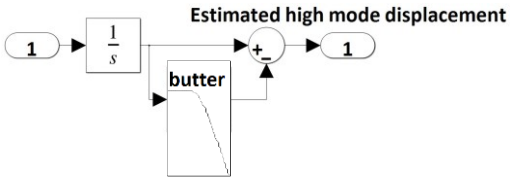


Fig. 3.9 SIMULINK sub-block for model in Figure 3.8.

Figure 3.10 shows the SIMULINK model of the phase synchronisation subsystem, which contains 21 components. Moving clockwise around the loop, these include three constant blocks, a gain block, a low-mode VCO, a high-mode VCO, a scanner, two relays, a clock, a switch, two integral divide-by-N circuits, a 90° PS, a phase detector, an additional clock, a second switch, an integral controller, a summing block, an initial delay, and a variable time-delay block. Figure 3.11 shows the configuration of the integral divide-by-N circuit, based on a previous design [96-97]. The circuit takes a square wave as input and generates a square wave that preserves the positive edges. This is achieved using digital components such as counters, flip-flops (FFs), and logic gates. The DC offset of the low-mode frequency-divided square wave is then removed

using the same method described earlier. Compared with earlier simulations, this model includes two switches. Switch 1 ensures that the frequency-divided square waves start with a controlled phase error by activating the integral divide-by-N circuits at the same time. Switch 2 performs the same function as in the previous subsystem.

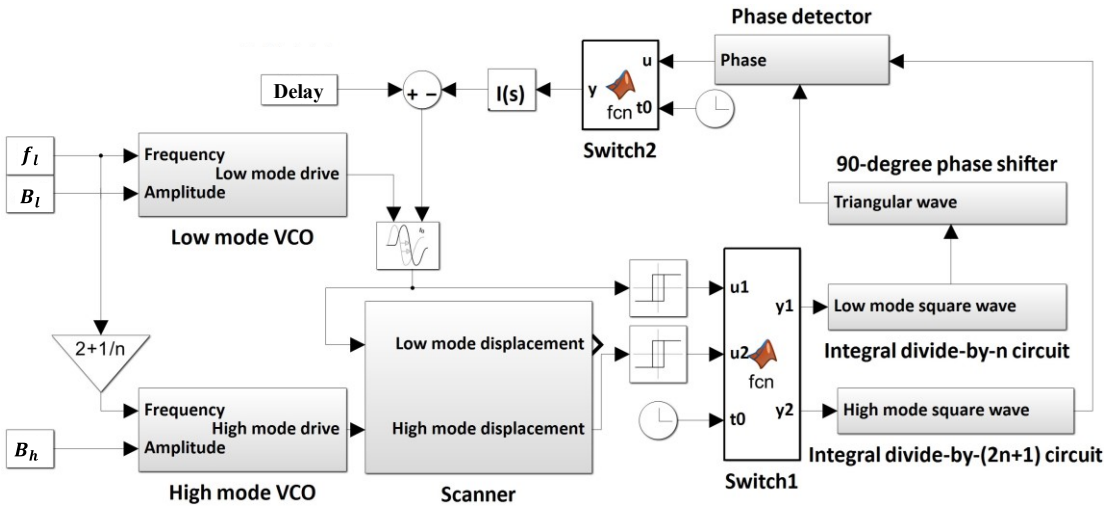


Fig. 3.10 SIMULINK model of phase synchronisation.

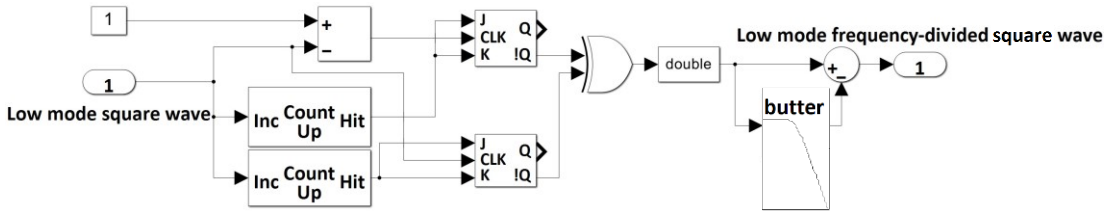


Fig. 3.11 SIMULINK sub-block for model in Figure 3.10.

Figure 3.12 shows the SIMULINK model of the amplitude control subsystem, which consists of 21 components. From left to right, these include three constants, a gain, two summing junctions, a low mode VCO, a high mode VCO, two integral controllers, two switches, a scanner, two clocks, a constant, two additional summing blocks, a gain, a reflector, and two duty cycle detectors for the two modes. Figure 3.13 shows the configuration of the duty cycle detector sub-block. The key elements in this subsystem are the constant block D_{h0} and the gain factor $2\sin^{-1}(W)/\pi$, which are used to equalise the displacement amplitudes and adjust the duty cycle to the reference value D_{h0}. The duty cycle detector shown in Figure 3.13 employs a Butterworth LPF to extract the DC offset and subsequently divides it by the reflectivity.

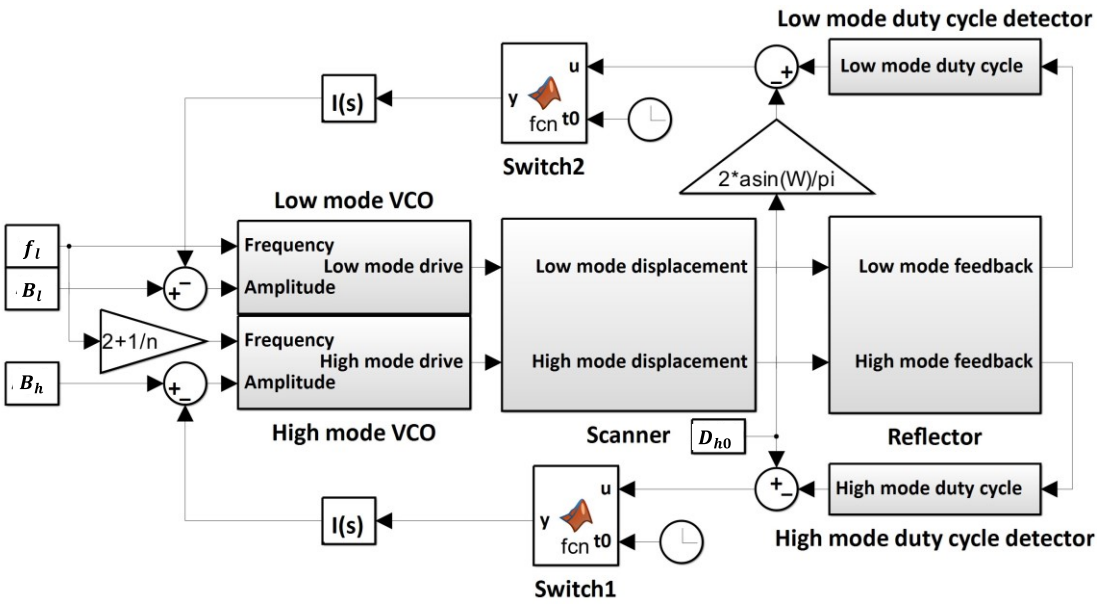


Fig. 3.12 SIMULINK model of amplitude control.

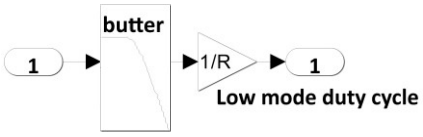


Fig. 3.13 SIMULINK sub-block for model in Figure 3.12.

3.3 Experimental Fibre Fabrication

Fibre cantilevers are needed to demonstrate Lissajous scanning experimentally. However, as previously discussed, conventional fibres are unsuitable. In this section, a dip-coating method [69] is used to convert standard SMFs into a dual-core structure, producing a resonant frequency ratio of approximately 2. The resulting fibres are robust, stable and can be fabricated with high reproducibility. Their performance can be evaluated based on measured resonant frequency ratios.

Theoretical Resonant Frequency Ratio

Figure 3.14 shows the theoretical cross-sections of dual-core fibres, with the core and cladding regions indicated by red arrows. The cross-sections are based on a COTS SMF (SM600, Thorlabs). Since the fibre cantilevers have the same length and are made of the same material, the resonant frequency ratio between the two orthogonal vibration modes can be derived from Eqn. (1.6) as:

$$\frac{f_x}{f_y} = \sqrt{\frac{I_{yy}}{I_{xx}}} \tag{3.1}$$

We assume that small variations in the mechanical properties of the glass defining the core can be neglected. For a cylindrical fibre with radius r, the second moments of area in the two orthogonal directions are identical, as given by Eqn. (1.9), resulting in a unity resonant frequency ratio. Figure 3.14(a) shows the dual-core configuration formed by attaching two fibres together. In this case, the second moments of area can be calculated using the parallel axis theorem and Eqn. (1.10) as [69]:

$$I_{xx} = 2\left(\frac{\pi r^4}{4}\right) \tag{3.2}$$

$$I_{yy} = 2\left(\pi r^4 + \frac{\pi r^4}{4}\right) \tag{3.3}$$

which yields a ratio of $\sqrt{5}$ $(n = 3)$, generating sparse scan lines. Figure 3.14(b) shows a polymer fillet added between the two fibres, filling the groove region to overcome this limitation. Let the Young's moduli of the fibre and polymer be E_f and E_p, respectively, and define $R = E_p/E_f$. The modified frequency ratio becomes [69]:

$$\frac{f_x}{f_y} = \sqrt{\frac{5 + R\dfrac{16 - 5\pi}{2\pi}}{1 + R\dfrac{16 - 3\pi}{6\pi}}} \tag{3.4}$$

For $R = 1$, the ratio decreases to below 2, implying that fibres with higher integer n values (greater than 3) can be achieved by adjusting the amount of polymer fillet.

Figure 3.14(c) shows the principle of dual-frequency excitation achieved using a single PT. The drive is applied at 45° with respect to the principal axes (green arrow) and can therefore be decomposed into two orthogonal components (red arrows). Owing to the low damping ratio and mechanical decoupling of the cantilever, it predominantly responds to excitation components close to its respective resonance frequencies. As a result, the fibre can simultaneously vibrate along two perpendicular directions. The details of the setup and the effect will be discussed in Chapter 4.

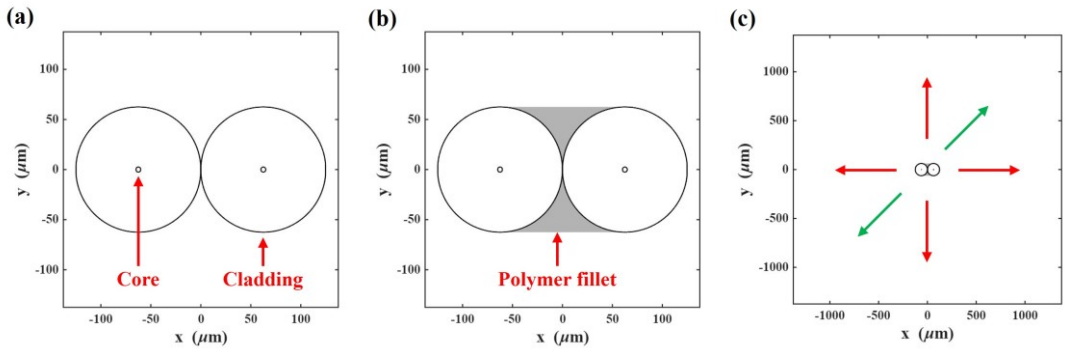


Fig. 3.14 Theoretical cross-sections of dual-core fibres (a) before and (b) after dip-coating with a polymer fillet; (c) excitation (green) for orthogonal fibre tip motion (red).

Dip-coating

A dip-coating technique was used to bond two cylindrical fibres together to form a dual-core structure. The SMFs (8/125 μm; BICC) naturally have a ribbon-like geometry, which makes them easy to pair into a double-fibre configuration suitable for dip-coating. Figure 3.15(a) shows the experimental setup for dip-coating, while Figure 3.15(b) shows its schematic design. The coater is driven by a DC power supply connected to a motor, with the rotation speed controlled by the applied voltage. The motor drives a gear assembly that adjusts the rotational speed. This gear set is mechanically connected to two rubber wheels that form a clamping mechanism, between which the fibre ribbon (red dashed line and thick black solid line) is held. As the wheels rotate, the fibre is pulled upward or downward through a tube containing the polymer solution. In this experiment, polymethyl methacrylate (PMMA; 950 PMMA A6, MicroChem) was used as the coating material, with a Young's modulus of $E = 3.1 \times 10^9 Nm^{-2}$. Other polymers, such as poly butyl methacrylate (PBMA) or sol-gel glass, may also be used.

Figure 3.15(c) shows the complete dip-coating procedure. In step (i), a pair of SMFs is separated from the fibre ribbon and stripped to obtain approximately 10 cm of bare fibre. Both ends are then cleaved to allow accurate alignment. In step (ii), the fibres are dip-coated using the apparatus shown in Figure 3.15(a). During this process, the two fibres are bonded together and a PMMA layer is deposited around the bare fibre sections. Different DC drive voltages are applied to set different pulling speeds, which control the polymer fillet formed between and around the fibres. The coated cantilever is then heated at 100 °C for 20 minutes to solidify the PMMA. In step (iii), the cantilever

is cleaved to obtain a clean cross-section without residual polymer. Figure 3.15(d) shows the cross-section of a typical dip-coated dual-core fibre cantilever with polymer fillet in the middle groove.

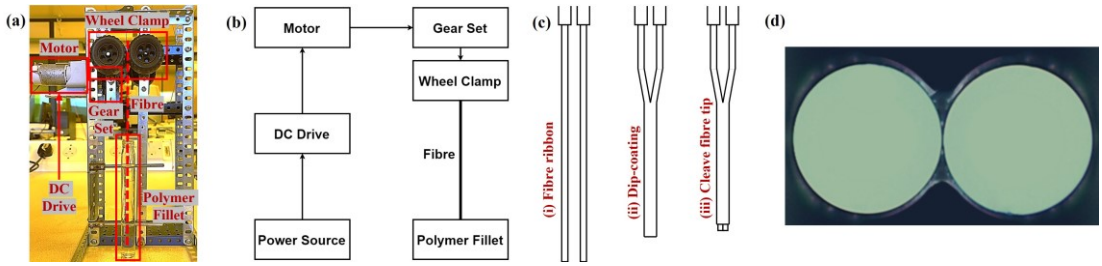


Fig. 3.15 (a) Device for dip-coating; (b) design of the device; (c) procedures of dip-coating; and (d) cross-section of a typical dip-coated fibre cantilever.

Cantilever Measurement

Measurements of resonant frequency were made as follows. The dip-coated cantilever was mounted on a PT, with the excitation direction indicated in Figure 3.14(c). The excitation frequency is swept while the fibre cross-section is observed under a microscope. When the cantilever is driven at its resonant frequencies, the fibre reaches its maximum displacement, which is identified by the length of the motion-induced blur. While this method produces an inaccuracy of less than 0.5% due to inevitable boundary definition uncertainty of the blur, it is sufficient to find an approximate resonant frequency to excite the fibre cantilever within the capture range.

Figure 3.16 shows the performance of the dip-coating method and the frequency response of the fibre cantilever. Figure 3.16(a) shows the variation of the resonant frequency ratio with the coater voltage, confirming that values close to $r = 2$ can be achieved. Figure 3.16(b) shows the corresponding variation of the integer parameter n estimated from these measurements. From this data, samples with $n = 31$ were identified as the most suitable for further experiments. The solid curves in Figure 3.16(c) show the amplitude responses of the two vibration modes for a selected cantilever, used in later experiments. By comparing these results with the theoretical response (dashed lines) based on Eqn. (2.10), the experimental resonant frequencies and damping ratios were obtained as $f_{l0} = 131.5Hz$, $f_{h0} = 267.25Hz$ (yielding $r = 2.0323$), $\zeta_l = 0.01$ and $\zeta_h = 0.004$. The experimental damping ratios were produced by changing

the damping ratios of the theoretical response until it overlapped with the experimental line. The shaded region indicates the range of high-mode frequencies within the capture range. Based on these measurements, the achievable range of n is approximately 19 to 61. In later experiments, values of 21, 41 and 61 were used to demonstrate programmable control of the scan-line density.

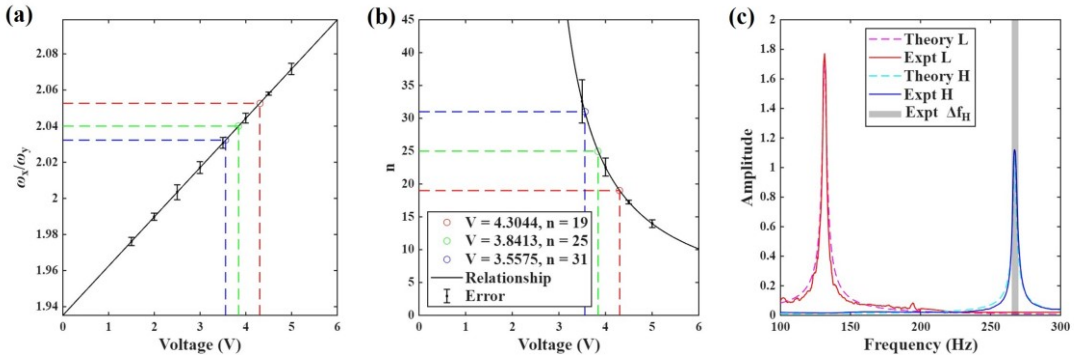


Fig. 3.16 Variation of the (a) resonant frequency ratio and (b) n as functions of motor voltage; and (c) comparison of theoretical and experimental response for orthogonal modes of the dual-core cantilever.

Figure 3.17(a) shows the normalised amplitude responses of the two vibration modes. The damping ratios are intentionally set to $\zeta_l = 0.05$ and $\zeta_h = 0.03$ to make the behaviour easier to see. When the low mode operates at its resonant frequency, the bandwidth of the high mode (blue dashed lines), defined by the threshold level (black dashed line), can be identified. The vertical dashed lines (cyan, magenta, and green) correspond to high-mode frequencies for $n = 21$, 41 and 61, respectively. The intersection points indicate the corresponding amplitude and phase responses at these values of n. Figure 3.17(b) shows the frequency response. The results confirm that the high mode is non-resonant, as predicted earlier, and that changing n allows the scan-line density and the frame rate to be programmed. Compared with Figure 3.16(c), larger damping ratios are used here, which indicates that the practical scanner will have a reduced range of programmability.

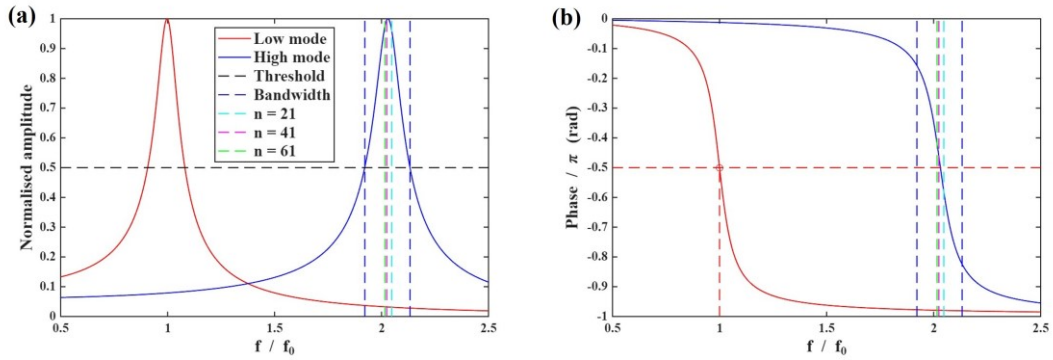


Fig. 3.17 Simulated (a) amplitude and (b) phase response of a dual-core fibre cantilever. ($f_x = 203Hz$, $f_y = 100Hz$, $\zeta_x = 0.03$, $\zeta_y = 0.05$)

3.4 Experiment Setup

In this section, the experimental setup for the scanner and its real-time controller is described. The circuit designs for the five subsystems are illustrated, and the individual electronic components are listed, with selected elements discussed in further detail. Figure 3.18 explains the overall operation of the scanner and its controller.

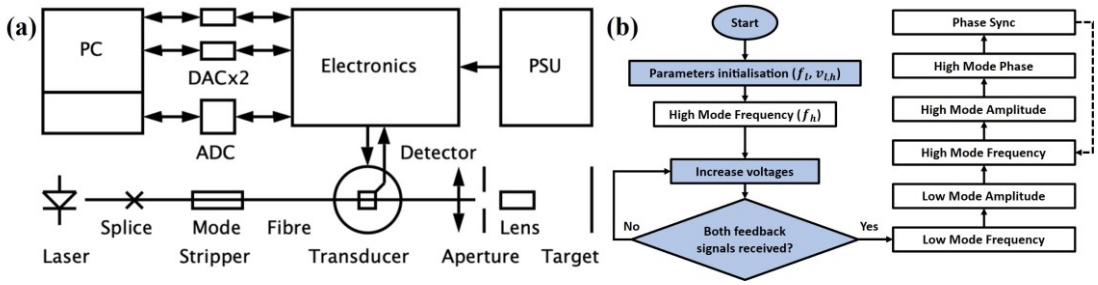


Fig. 3.18 Scanner controller: (a) schematic and (b) initialisation flowchart.

Figure 3.18(a) shows the complete experimental system. The scanner operates as a dual NA confocal microscope and uses a dip-coated fibre cantilever driven by a single PT. The transducer excites the fibre into 2D motion in front of a lens, which projects a moving image of the guided optical mode onto the target. Backscattered light is collected from the fibre cladding using mode-stripping PD. Intermittent optical feedback is generated by an aperture placed between the fibre tip and the lens. The controller consists of a PC connected to an electronic control module through digital-to-analogue (DAC) and analogue-to-digital (ADC) converters, allowing signals to be exchanged between the control electronics and the scanner drive and detection units. Figure 3.18(b) shows the operational flowchart, which includes two stages: software

initialisation and hardware locking. During the software initialisation stage, both vibration modes are driven close to their estimated resonant frequencies under PC control. The driving amplitudes are gradually increased until feedback is detected, after which the aperture and lens are adjusted to centre the optical system. In the hardware-locking stage, the controller operates autonomously to lock the frequencies and amplitudes, enabling stable 2D scanning.

Figure 3.19 shows the high-level structure of the controller, which has un-clocked (NI USB-6009, National Instruments) and clocked (NI my DAQ, National Instruments) DACs, a USB scope (2206B, Picoscope) acting as an ADC, and a level trigger separating the low and high mode feedback. The controller performs 6 main operations:

1. Locking the low-mode frequency to its resonant frequency.
2. Setting the low-mode scan amplitude to a suitable value.
3. Generating the high-mode drive in a fixed frequency ratio to the low-mode drive.
4. Equalising the high-mode scan amplitude.
5. Estimating the high-mode phase.
6. Correcting the relative phase of the two modes.

The first two processes will be performed once; the last four are repeated whenever different Lissajous figures are selected. All operations involve control loops except #3.

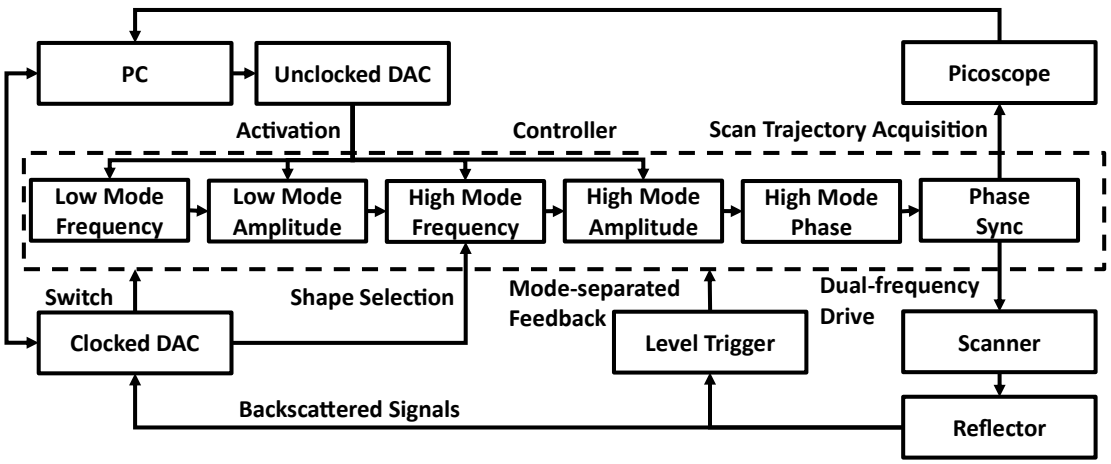


Fig. 3.19 High-level block diagram for circuit design.

Figure 3.20 shows the circuit block diagram of the low-mode frequency lock subsystem, which contains 12 sub-circuits. Moving clockwise around the loop, these include a differential amplifier, a VCO, an RC filter, an analogue multiplier, a non-inverting amplifier, a window comparator, a second analogue multiplier, a Butterworth LPF, an operational amplifier (op-amp) integrator, and an analogue switch. Two additional sub-circuits are also included: a differential amplifier for amplitude control and a summing amplifier used to add the high-mode drive. These will be discussed later. All sub-circuits, except for the analogue multipliers and the analogue switch, are built using operational amplifiers (LM324-N, Texas Instruments), resistors, capacitors, and an NPN transistor (2N3903, Onsemi). The analogue multiplier (AD633, Analog Devices) and the analogue switch (DG201A, Analog Devices) are COTS components. Simplified circuit diagrams explaining their operation are shown in Figure 3.21.

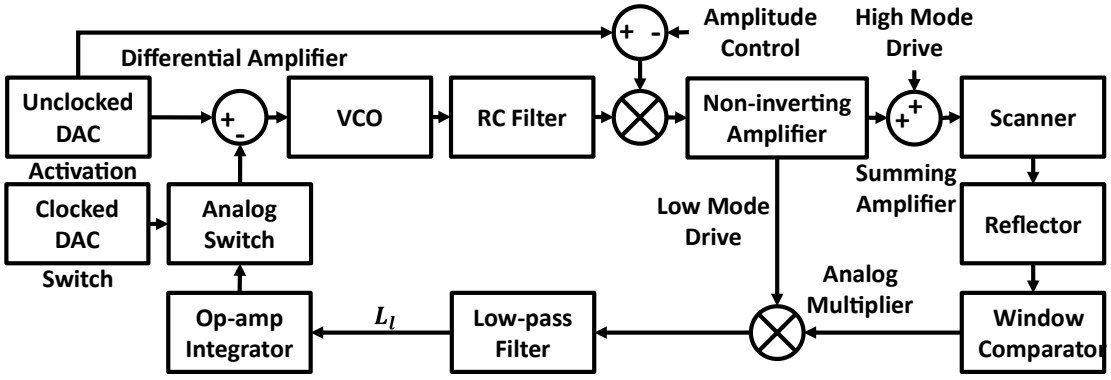


Fig. 3.20 Circuit design for low-mode frequency lock.

Figure 3.21(a) shows a differential amplifier configured as a unity-gain op-amp for signal subtraction. It is connected to the un-clocked DAC to provide an initial voltage to start the control loop. When the analogue switch is off, the other input is grounded. Figure 3.21(b) shows the VCO, which works by changing the control voltage applied to an NPN transistor. This changes the charging and discharging speed of a capacitor and therefore adjusts the oscillation frequency. The VCO produces frequencies from 75 Hz to 300 Hz for control voltages between 0.05 V and 0.65 V. Figure 3.21(c) shows the RC filter, which consists of a five-stage RC ladder and an additional capacitor to remove DC offset. It has a cutoff frequency of 159 Hz and a 5^{th} roll-off. The analogue multiplier

uses a Gilbert-cell structure to generate an output equal to the product of its two differential inputs. This multiplier is connected to the un-clocked DAC to allow amplitude adjustment during system start-up. Figure 3.21(d) shows a non-inverting amplifier, where the gain is chosen to set the overall loop gain. Figure 3.21(e) shows a window comparator, which compares the input signal with two preset thresholds and indicates whether the signal lies within this range. These thresholds are calibrated using the reflectivity of the feedback signal to ensure reliable operation. The feedback signal is then multiplied by the driving signal using another analogue multiplier. Figure 3.21(f) shows a Butterworth LPF. It is a second-order filter with a cutoff frequency of 2 Hz. Figure 3.21(h) shows an op-amp integrator, with a DC cutoff and a first-order roll-off. Finally, the analogue switch uses two MOSFETs controlled by a digital input to switch the signal on or off. This switch is connected to the clocked DAC to allow synchronised control.

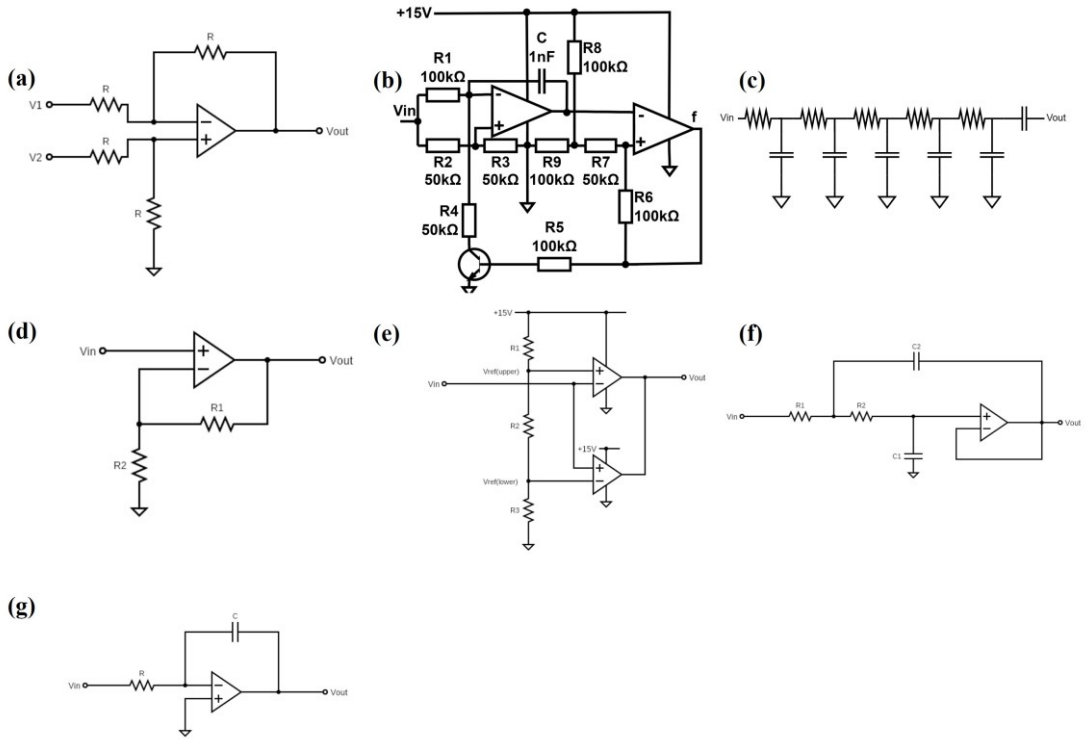


Fig. 3.21 Circuit components of the block diagram of Figure 3.20: (a) differential amplifier, (b) voltage-controlled oscillator, (c) RC filter, (d) non-inverting amplifier, (e) window comparator, (f) Butterworth low-pass filter, and (g) op-amp integrator.

Figure 3.22 shows the circuit block diagram of the high-mode frequency generation subsystem, which consists of 6 sub-circuits: two analogue multipliers, a summing amplifier, a VCO, an RC filter, and a non-inverting amplifier. Two additional differential amplifiers are included for activation and amplitude control in later stages. The analogue multipliers are identical to those described in the previous section. Figure 3.23 shows the summing amplifier, which is a unity-gain op-amp circuit used to add signals. Both the analogue multiplier and the summing amplifier are connected to the un-clocked DAC. The DAC provides control voltages that set the high-mode frequency based on a fixed relationship with the low-mode frequency. These voltages can be changed by programming the DAC, allowing the Lissajous pattern to be adjusted. The VCO uses the same circuit design as described earlier. The RC filter also has the same structure, but with a higher cutoff frequency of 318 Hz to suit the high-mode frequency range. Finally, a non-inverting amplifier increases the amplitude of the driving signal to provide sufficient excitation for the scanner.

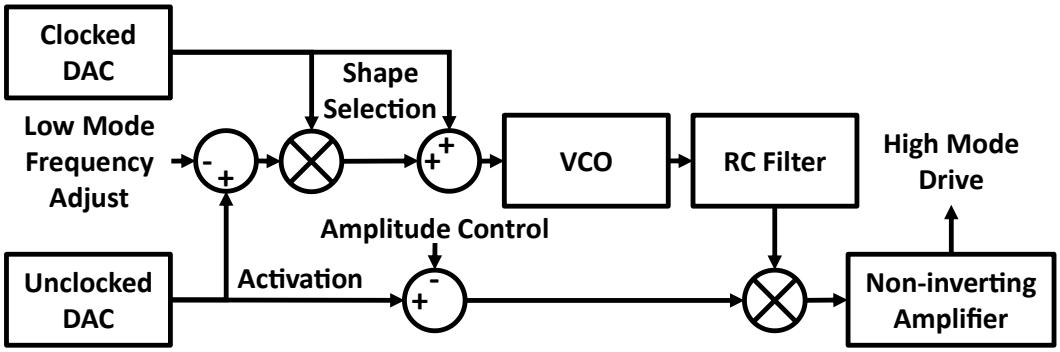


Fig. 3.22 Circuit design for high-mode frequency generation.

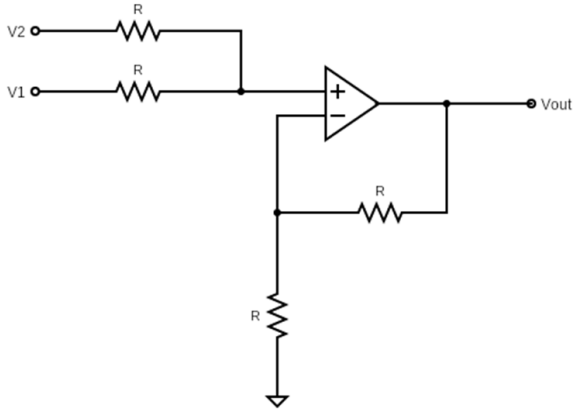


Fig. 3.23 Circuit diagram of the summing amplifier block diagram of Figure 3.22.

Figure 3.24 shows the circuit block diagram of the high-mode displacement estimation subsystem, consisting of 10 sub-circuits arranged clockwise: a non-inverting amplifier, a multiplier, a Butterworth LPF, an integrator, a switch, a differential amplifier, a VCPS, a second integrator, a DC blocker, and an inverting amplifier. A small initial voltage, denoted as v_{int1}, is applied in the circuit to start the control loop. The summing amplifier located at the top-left corner provides the feed-in for the high-mode driving signal. Figure 3.25(a) shows the non-inverting comparator, which compares an input voltage with a reference voltage and outputs a high or low level depending on the comparison result. The reference voltage is set using the reflectivity calibrator to ensure reliable feedback detection. Except for the VCPS, the DC blocker, and the inverting amplifier, all other sub-circuits are the same as those described earlier. Figure 3.25(b) shows the VCPS, which is implemented using all-pass filters. The phase shift is controlled by changing the resistance, which is realised using a bypassed junction field-effect transistor (JFET; LSK389, Linear Systems). This allows the phase to be adjusted using a control voltage. Figure 3.25(c) shows the DC blocker, which combines a Butterworth LPF with a differential amplifier to remove DC offset without introducing additional phase shift. Finally, Figure 3.25(d) shows the inverting amplifier, which is a unity-gain op-amp circuit used to invert the input signal.

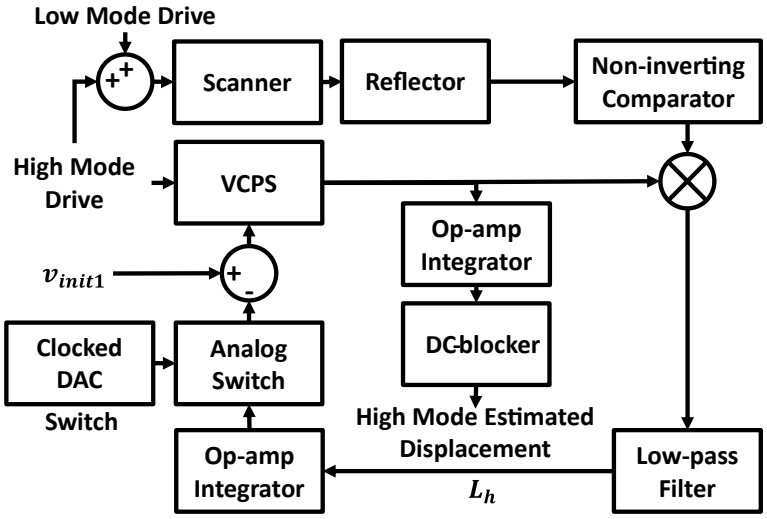


Fig. 3.24 Circuit design for high-mode displacement estimation.

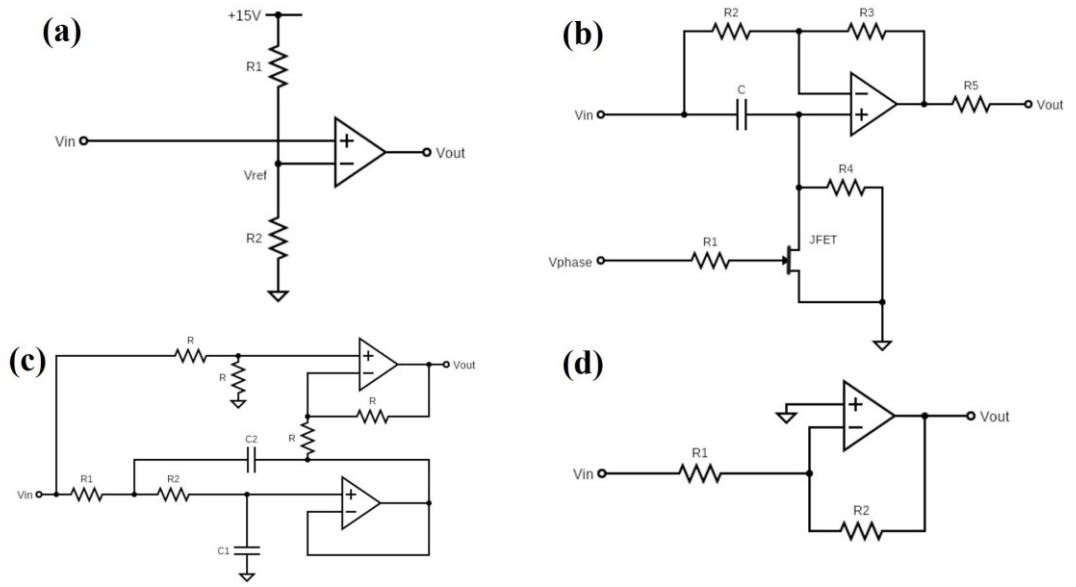


Fig. 3.25 Circuit components of the block diagram of Figure 3.24: (a) non-inverting comparator, (b) voltage-controlled phase shifter, (c) DC-blocker and (d) inverting amplifier.

Figure 3.26 shows the circuit block diagram of the phase synchronisation subsystem. The circuit contains 14 sub-circuits, including a non-inverting comparator, three analogue switches, a VCPS, an inverting amplifier, divide-by-N circuits, two op-amp integrators, a DC blocker, an analogue multiplier, a differential amplifier, and a Butterworth LPF. Figure 3.27 shows the additional supporting sub-circuits used in this subsystem. A Picoscope is connected to the circuit to record and monitor the synchronised scanning trajectories.

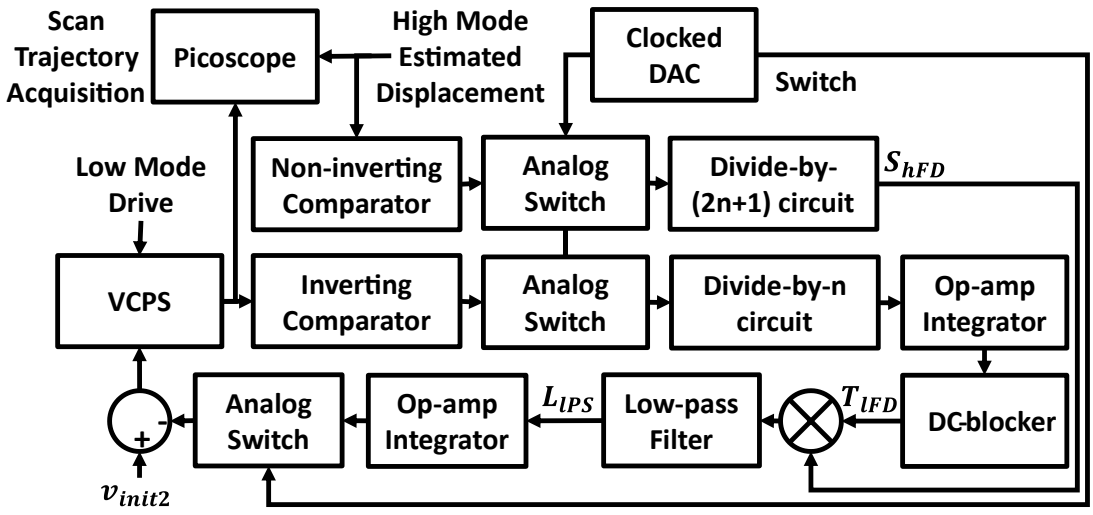


Fig. 3.26 Circuit design for phase synchronisation.

The non-inverting comparator uses the same circuit as described earlier, except that the reference voltage is set to zero. Figure 3.27(a) shows the inverting comparator, which compares the input voltage with a reference voltage and outputs a low level when the input is higher than the reference. In this case, the reference voltage is also set to zero. Figure 3.27(b) shows the integral divide-by-N circuit, which uses binary counters (TC74HC4040AP, Toshiba) to generate periodic signals that reset automatically. The counters are connected to the digital outputs of the DACs to set the reset values. In a binary system, the values of n and $2n+1$ differ only in the last two bits, so both values can be set using a single DAC channel. JK FFs (CD74HC73E, Texas Instruments) are used to halve the frequency, and an XOR gate (CD4070BE, Texas Instruments) produces a divide-by-N output with a 50% duty cycle.

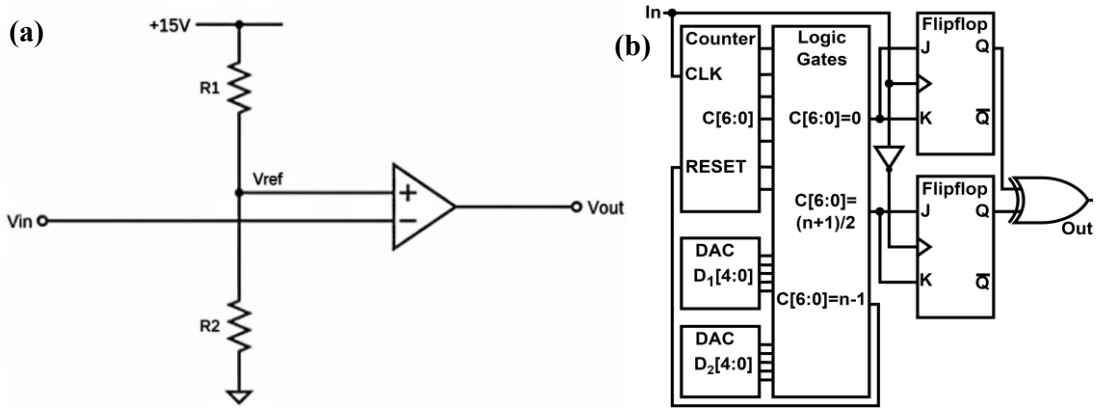


Fig. 3.27 Circuit components of the block diagram of Figure 3.26: (a) inverting comparator and (b) divide-by-N circuit.

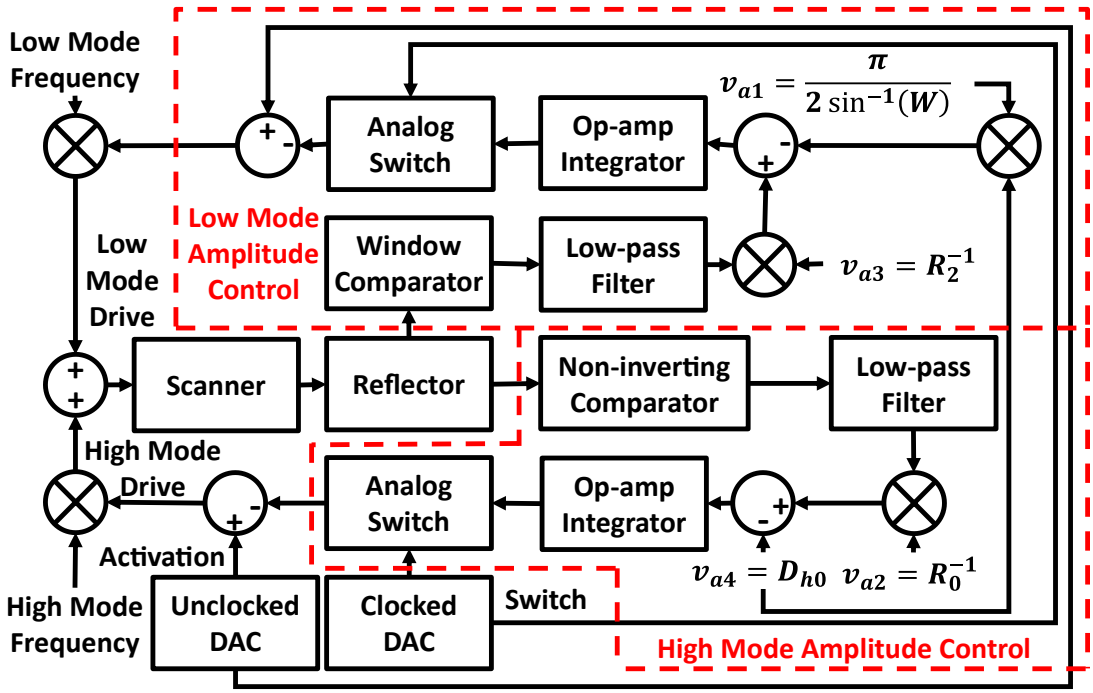


Fig. 3.28 Block diagram of the amplitude control sub-system.

Figure 3.28 shows a block diagram of the amplitude control subsystem. The circuit consists of several analogue and op-amp sub-circuits arranged in rows, including analogue multipliers, differential amplifiers, analogue switches, op-amp integrators, window comparators, Butterworth LPFs, summing amplifiers, and non-inverting comparators. All these sub-circuits have been described in earlier sections. In this subsystem, the duty cycles of the feedback signals are controlled to reach a target value v_{a4}, with a fixed ratio set by v_{a1}. This ensures equal vibration amplitudes and produces a square FOV. The feedback signals are extracted using the same method as in the previous subsystems. The duty cycles are obtained using LPFs, and the effect of reflectivity is removed using analogue multipliers with inputs v_{a2} and v_{a3}. The difference between the measured and target duty cycles is integrated, and the resulting control voltage is compared with the activation amplitude from the un-clocked DAC to form a negative feedback amplitude control loop. The analogue switches are controlled by the clocked DAC to ensure synchronised operation. Finally, the two driving signals are combined using a summing amplifier to excite the scanner. All reference voltages are generated within the circuit.

Figure 3.29 shows the experimental setup of the controller circuit and its connections to the associated hardware. The central part of the setup includes the breadboard circuit, the control PC (ThinkPad, Lenovo), and two DACs used to set the scan parameters and initialise the different control loops. The Picoscope, located on the right, is used to record the backscattered signals. The un-clocked DAC provides analogue outputs from 0 V to +5 V with 12-bit resolution. The clocked DAC includes clocked input and output channels, and provides digital outputs up to +5 V and analogue outputs in the range of ±10 V, with a maximum update rate of 200 kS/s. The Picoscope used in this system is a 20 MHz digital storage oscilloscope. Communication and data acquisition are carried out through USB connections, and the system is controlled using MATLAB. The breadboard circuit contains all sub-circuits shown in Figure 3.19, and the power supply lines are decoupled using capacitors to reduce noise and interference.

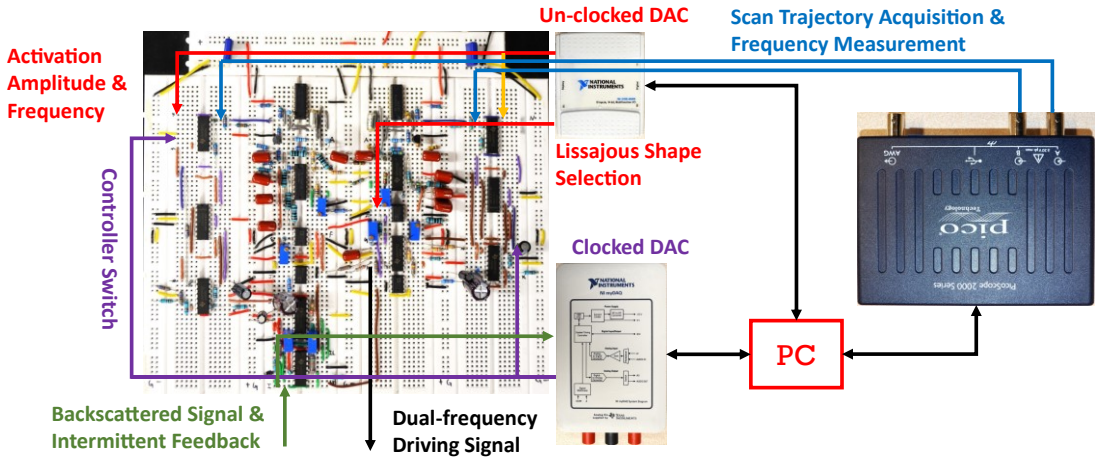


Fig. 3.29 Experimental controller circuit and its connection to additional units

3.5 Performance

In this section, the performance of the subsystems is analysed using the simulation models and the experimental circuit designs. The theoretical open-loop responses introduced in Chapter 2 are compared with both simulation and experimental results. The closed-loop system is modelled using NDDEs [130-131] to account for the nonlinear open-loop behaviour and the delays introduced by the LPFs. Key parameters, such as the critical gain and transient response time, are extracted and compared with the corresponding simulation and experimental results.

Low-Mode Frequency Lock

The open-loop response of the low-mode frequency lock subsystem, derived from the LPF output, is described by Eqn. (2.19). This term is used in the feedback loop that locks the driving signal to the resonant frequency. However, L_l varies periodically with ϕ_l, so there is a limited range near $\phi_l = -\pi/2$ (pull-in range) for a successful lock. Here, we may assume that ϕ_l varies linearly with the frequency deviation $\Delta f_l = f_l - f_{l0}$, following Eqn. (2.12). If Δf_l is also small, $L_l \approx Q_l \Delta f_l$, in which:

$$Q_l = \frac{R_2 A_l D_b}{\pi \zeta_l f_{l0}} \sin(D_a \pi) \tag{3.5}$$

Assuming additional feedback gain k_l and aggregate time delay τ_l introduced by the filters in the loop, the NDDE governing the loop can be written as:

$$\dot{f_l} = -k_l Q_l \Delta f_l (t - \tau_l) \tag{3.6}$$

Considering the equilibrium point $f_l = f_{l0}$, small perturbation near resonance is:

$$\lambda f_l = f_{l0} + \rho e^{\lambda t}, (\rho \ll 1) \tag{3.7}$$

Substituting this into Eqn. (3.6) yields the characteristic equation:

$$\lambda = k_l L_l'(f_{l0}) e^{-\lambda \tau_l} \tag{3.8}$$

Stability condition changes when the real part crosses the imaginary axis. Substituting $\lambda = -i\beta$ into Eqn. (3.8) and separating real and imaginary parts gives the critical gain:

$$k_l = \frac{\pi^2 \zeta_l f_{l0}}{2\tau_l R_2 A_l D_b \sin(D_a \pi)} \tag{3.9}$$

For small and constant $k_l Q_l$ within the stability limit (below the critical gain), the solution is a decaying exponential:

$$\Delta f_l(t) = \Delta f_l(0) e^{-k_l Q_l} \tag{3.10}$$

Convergence is accelerated by increasing k_l; however, when the gain exceeds the critical value, the system exhibits oscillatory behaviour due to the inherent delay τ_l.

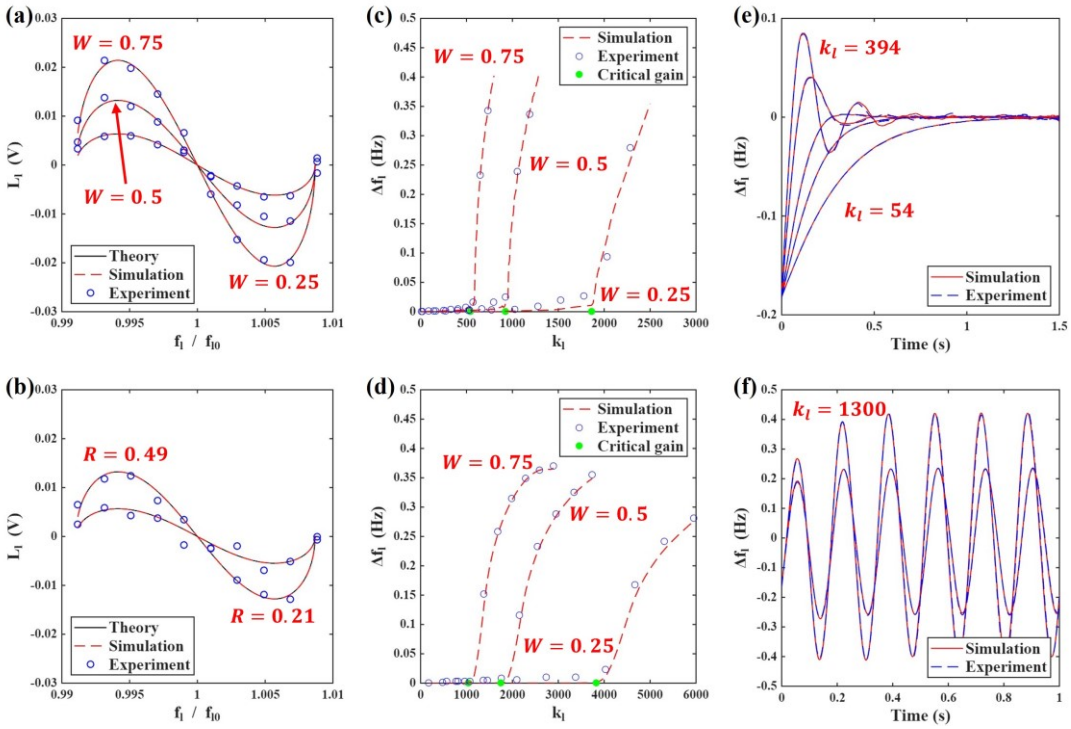


Fig. 3.30 Low mode: variation of open-loop LPF output L_l with f_l for (a) different W and (b) different R; variation of closed-loop frequency error Δf_l with k_l for (c) $R = 0.49$ and (d) $R = 0.21$ for different W; closed-loop trajectories for $R = 0.49$, $W = 0.5$ and different k_l, showing (e) convergence and (f) oscillation.

Figure 3.30(a-b) shows the open-loop response L_l of the low-mode LPF output as a function of frequency f_l for different values of width W and reflectivity R. The black and red dashed lines correspond to the theoretical prediction from Eqn. (2.19), and the SIMULINK simulation results, respectively. In all cases, L_l varies quasi-sinusoidally with frequency, while its amplitude depends strongly on both W and R. For a given set of W and R, the convergence behaviour is governed by the feedback gain k_l: as k_l increases, convergence accelerates until oscillations emerge at the critical gain k_{lC}. Figure 3.30(c-d) shows the variation of the steady-state frequency error Δf_l as a function of k_l for $R = 0.49$ and $R = 0.21$ with different W values. The errors remain zero below the critical gain k_{lC} predicted by Eqn. (3.9) (green points), while the SIMULINK results (red dashed lines) exhibit a sharp rise beyond these thresholds. Figure 3.30(e-f) shows simulated trajectories for $R = 0.49$, $W = 0.5$, and various k_l values, showing (e) progressively faster convergence and eventual

overshoot as k_l approaches k_{lC}, and (f) sustained oscillations as k_l exceeds k_{lC}. Under critical damping conditions, the settling time is approximately 300 ms.

High-Mode Displacement Estimation

Figure 3.31(a) shows the measured relationship between the VCO output frequency and the control voltage. The frequency varies linearly with the applied voltage and follows:

$$f_V = 0.3529 v_{DC} + 68.94 \tag{3.11}$$

Based on this relationship, the voltages applied to the two VCOs for $n = 31$ satisfy:

$$v_{hV} = 2.03 v_{lV} + 400 \tag{3.12}$$

Figure 3.31(b) shows the open-loop output L_h of the high-mode LPF output as a function of the phase error $\phi_{hPS} - \phi_h - \pi/2$, where ϕ_{hPS} and ϕ_h are the phases of the VCPS output and the high-mode feedback. The variation is sinusoidal, and L_h is zero when $\phi_{hPS} - \phi_h - \pi/2 = 0$. Figure 3.31(c) shows the high-mode displacement estimation signals: the driving signal (red solid line) is phase-shifted (red dashed line) to align with the feedback signal (black solid line), providing an accurate estimation of the high-mode displacement.

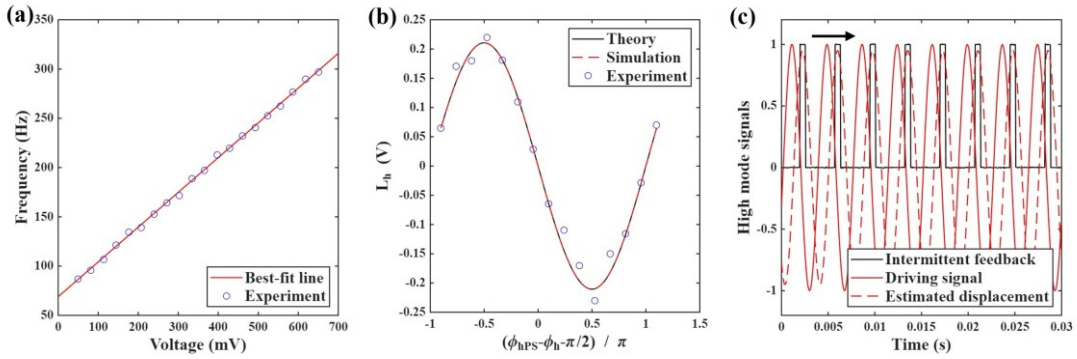


Fig. 3.31 (a) VCO output frequency versus input voltage; (b) variation of open-loop LPF output L_h with $\phi_{hPS} - \phi_h - \frac{\pi}{2}$; and (c) signals of high mode displacement estimation.

The control loop also includes delays introduced by the LPFs, resulting in similar dynamic behaviour to that observed in Figure 3.30. Figure 3.32(a) shows the peak variation of error ΔL_h with loop gain k_h; errors are again low below the critical gain k_{hC} (green point) and rise rapidly thereafter. Figure 3.32(b-c) show predicted trajectories for values of k_h as indicated, showing (b) convergence and then overshoot

as k_h approaches k_{hC} and (c) steady and then growing oscillation as k_h rises above k_{hC}. For critical damping, the settling time is approximately 100 ms.

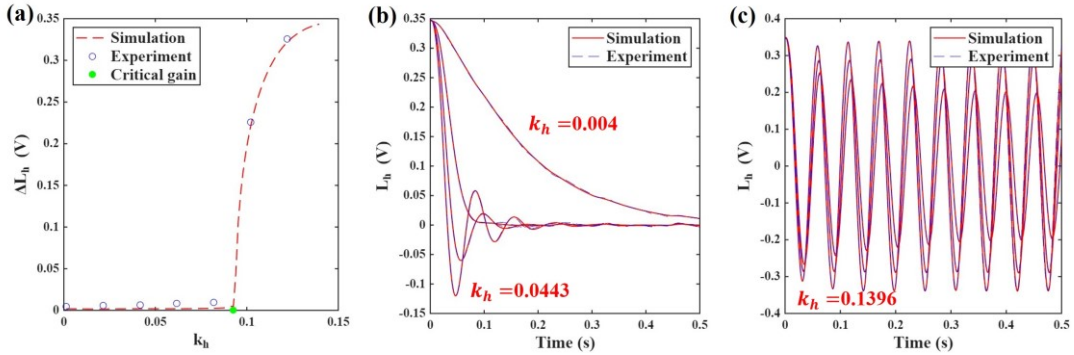


Fig. 3.32 (a) Variation of closed-loop LPF output error L_h with k_h; and closed-loop trajectories for different k_h, showing (b) convergence and (c) oscillation.

Phase Synchronisation

Figure 3.33(a) shows input and output signals for the low and high modes for $n = 31$. The input signals are square waves with different frequencies. After division, the outputs have CFs and have been phase-locked by the phase synchronisation loop. Figure 3.33(b) shows the variation of the open-loop output L_{lPS} of the LPF output with the phase error $\Delta\phi_C$ between the two CF signals. Because of frequency division, the possible phase error is much smaller here, and the variation over the range shown is very linear. Figure 3.33(c) shows examples of the high mode square wave and the low mode triangular wave before and after closed-loop operation; the latter has clearly been driven into phase-lock with the square wave. The control loop also introduces delays from LPFs, leading to behaviour like that observed in Figure 3.30. Figure 3.34(a) shows the peak variation of the phase error ΔL_{lPS} as a function of the loop gain k_{lPS}. The errors remain minimal below the critical gain k_{lPSC} (green point) but increase sharply once this threshold is exceeded. Figure 3.34(b-c) shows the predicted trajectories for the indicated values of k_{lPS}: (b) shows convergence followed by overshoot as k_{lPS} approaches k_{lPSC}, while (c) shows stable oscillations that grow as k_{lPS} rises above k_{lPSC}. Under critical damping conditions, the settling time is around 500 ms.

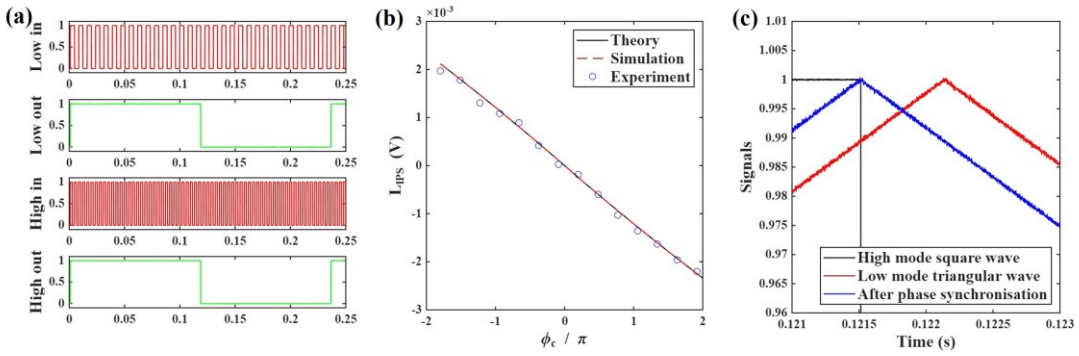


Fig. 3.33 (a) Experimental demonstration of frequency division with $n = 31$; (b) variation of open-loop LPF output L_{lPS} with ϕ_c; and (c) alignment of signals.

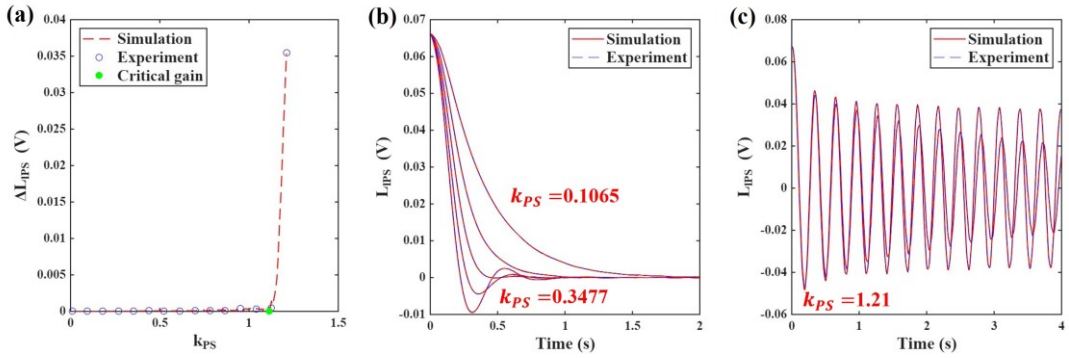


Fig. 3.34 (a) Variation of closed-loop LPF output error L_{hPS} with k_{hPS}; and closed-loop trajectories for different k_{hPS}, showing (b) convergence and (c) oscillation.

Amplitude Control

Figure 3.35(a) shows how the duty cycle varies with vibration amplitude for both modes. For the low mode, results are shown for different reflector widths W. A width of $W = 0.5$ is used in the experiments, and for this value the ratio between the high- and low-mode duty cycles is 3. Figure 3.35(b-c) shows the steady-state traces of the simulated and experimental feedback signals. The matching widths of all four feedback pulses confirm correct amplitude equalisation. The black dashed lines indicate the thresholds used to distinguish feedback signals. The amplitude control loop also includes delays. Figure 3.36(a) shows the peak variation of the error ΔD_h as a function of the loop gain k_a. The error remains small below the critical gain k_{aC} (green point) and increases rapidly when this value is exceeded. Figure 3.36(b-c) shows the predicted trajectories for different values of k_a: (b) shows convergence followed by overshoot as k_a approaches k_{aC}, while (c) shows oscillations that grow as k_a increases beyond k_{aC}. Under critically damped conditions, the settling time is approximately 300 ms.

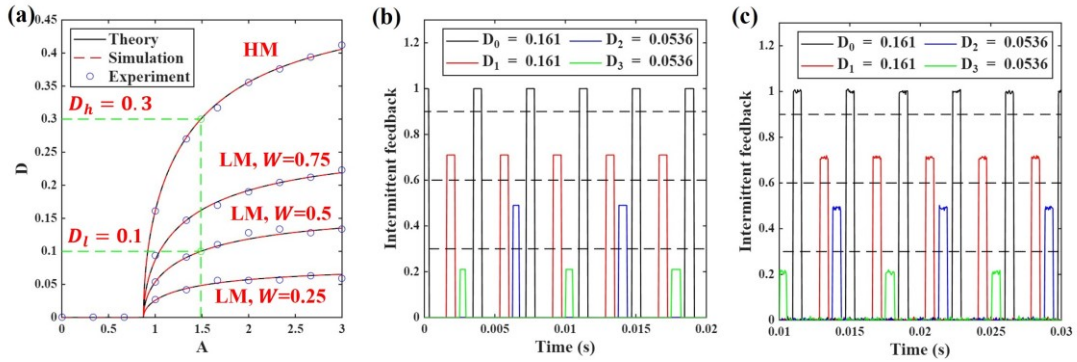


Fig. 3.35 (a) Open-loop response of duty cycle D with A and closed-loop variation of feedback signals from (b) simulation and (c) experiment.

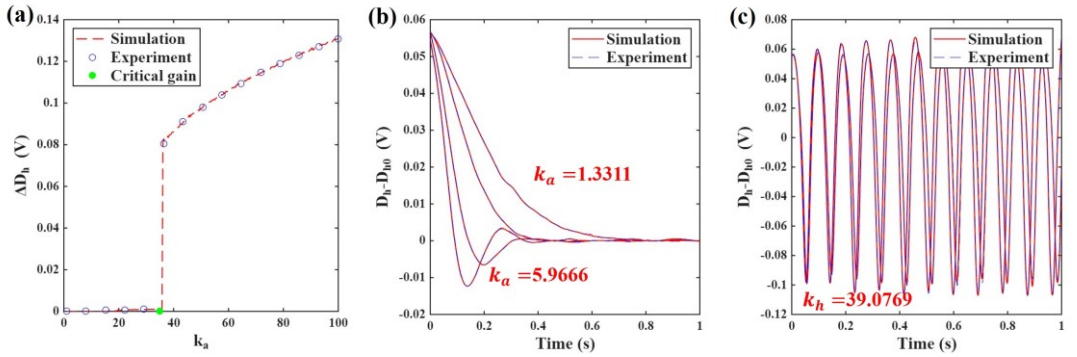


Fig. 3.36 (a) Variation of closed-loop duty cycle error D_h with k_a; and closed-loop trajectories for different k_a, showing (b) convergence and (c) oscillation.

Overall, the control electronics performed as expected. The discrete data points in Figures 3.30-3.36 show experimental results with good agreement to the simulations. This close match is mainly due to the low operating frequencies of the system, which reduce the effects of parasitic circuit elements and other non-ideal behaviour.

3.6 Conclusion

The design, simulation, and experimental implementation of a real-time controller for a 2D Lissajous fibre scanner have been presented. A dip-coating method was modified to fabricate a dual-core fibre cantilever with a continuously adjustable resonant frequency ratio. This process produces a frequency ratio close to 2, which enables the generation of a symmetric Lissajous scanning pattern. The dip-coating method was optimised to achieve stable and reproducible dual-core fibre structures. Based on the theoretical analysis in Chapter 2, five control subsystems were designed. Each was first described using a theoretical block diagram and then implemented in SIMULINK to

verify its operation. The simulation results showed stable behaviour, confirming that frequency and amplitude locking can be achieved with predictable dynamics governed by NDDEs. The controller was then implemented experimentally, and its performance was found to agree well with both theory and simulation. The open- and closed-loop behaviours were analysed to study the effects of gain and delay, revealing clear critical gains and settling times that match the NDDE predictions. Overall, the system achieves stable dual-frequency operation, accurate phase synchronisation, and automatic amplitude equalisation, enabling reliable real-time control of the scanner. The complete scanning system operating under this controller will be presented in a later chapter, where its imaging performance will be evaluated. Future work could examine the robustness of the controller and study its response to external disturbances.

Chapter 4: 2D Lissajous Fibre Scanning System

In this chapter, the complete 2D Lissajous fibre scanning system is presented, based on a dual NA confocal detection scheme [52]. An amplitude-coded reflecting aperture is introduced to generate distinguishable optical feedback signals, followed by a description of the scanner setup, which shows how the optical and electronic systems are integrated. The real-time controller is used to drive the 2D Lissajous fibre scanner, producing symmetric scan trajectories with a square FOV. Photographs of the scan lines obtained for different aperture widths and values of n are presented. The system is then calibrated to correct for reflector tilt, alignment errors, and phase offsets. These effects are derived theoretically and evaluated using reconstructed images. The use of Delaunay triangulation [132-133] for 2D interpolation during image reconstruction is discussed. The sampling conditions required to sample at Padua points [134] are also analysed to optimise image resolution. Finally, image reconstruction is demonstrated under both transient and steady-state conditions. The transient results show system behaviour during parameter changes, while the steady-state results show reconstructed images obtained from the stabilised Lissajous fibre scanner.

4.1 Scanning System Setup

The scanning system is based on a dual NA confocal detection mechanism [52]. It consists of two main parts: the controller and the scanner. The controller was described in Chapter 3. In this chapter, the configuration of the scanner is presented.

Scanner

Figure 4.1 shows the schematic of the scanner setup, and Figure 4.2 shows the corresponding experimental arrangement. The scanner was assembled on an optical bench (Photon Control), and all components were aligned using XYZ micro-positioners (Photon Control). The optical source was a pigtailed 5 mW semiconductor laser operating at a wavelength of 635 nm (Seven Stage Optics), which was butt-coupled to one of the two fibre cores. A mode stripper, consisting of a neutral-density filter and index-matching liquid, was used to suppress cladding modes. Imaging was performed

using a 0.23-pitch gradient-index rod lens (GRIN2306A, Thorlabs) with an anti-reflection coating optimised for 635 nm. The apertures used for the real-time controller are described later. An aperture was mounted on a micro-positioner (Photon Control) with rotational adjustment. A 30 mm long fibre cantilever was attached using index-matching epoxy to a surface-mount silicon photodiode (SFH2430, ams-OSRAM AG), which was mounted at 45° on a disc PT (RS Pro 1587433, RS Components). The PT was selected so that its self-resonance is far away from the resonance of the fibre cantilever. The controller circuit generated the dual-frequency driving signal, while the backscattered optical signal, combined with the intermittent feedback, was collected by the real-time controller through the photodiode. The controller was interfaced with two DACs for communication and programming via a PC.

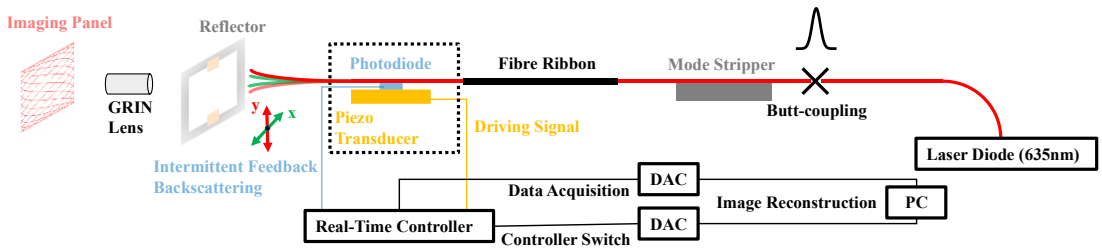


Fig. 4.1 Schematic setup of the 2D Lissajous fibre scanner.

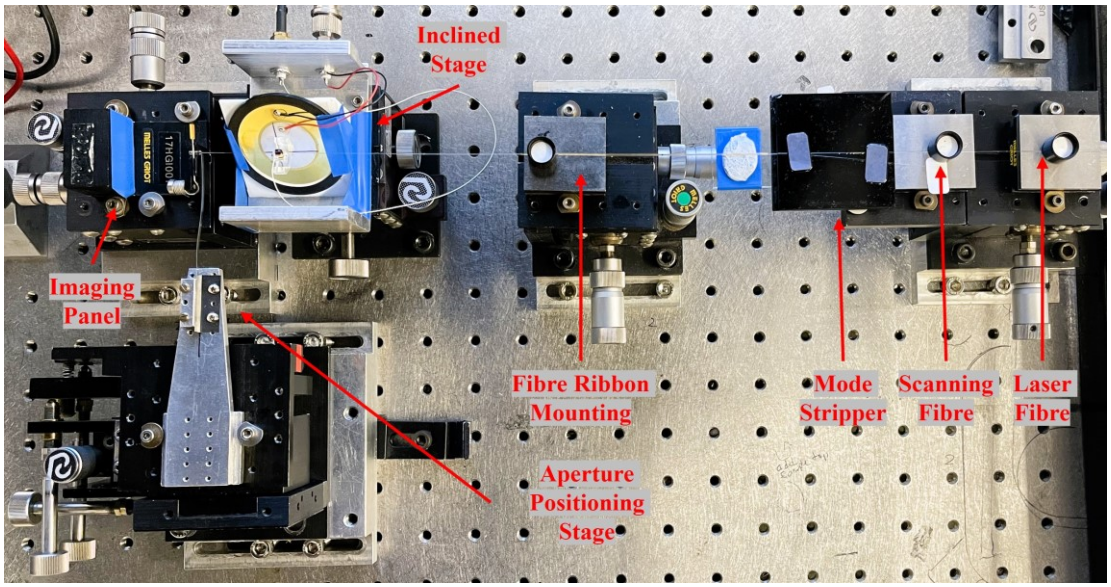


Fig. 4.2 Experimental setup of the 2D Lissajous fibre scanner.

Figure 4.3 shows the experimental fibre cantilever mounted on an inclined stage and the schematic front view. To align the Lissajous scanning trajectory with the

horizontal and vertical axes, the PT was mounted on an inclined platform with a 45° slope. A V-block, highlighted in blue in the figure, was fabricated using 3D printing. The fibre was placed at the centre of the V-groove and fixed using optical adhesive. An additional 3D-printed lid was used to provide temporary mechanical fixing. When assembled, the lid and the V-block formed a clamp, ensuring stable and repeatable mounting of the fibre during measurements. For permanent use, the optical adhesive with a refractive index higher than the cladding is used to mount the fibre and to couple the light from the cladding to the photodiode.

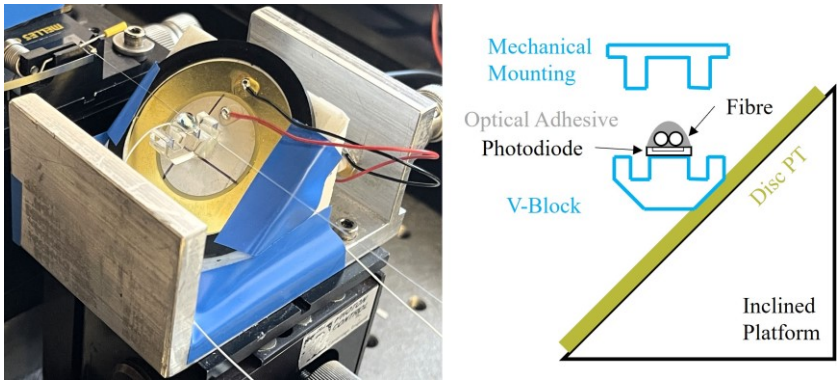


Fig. 4.3 Photo and schematic front view of fibre mounting.

Aperture

Apertures were formed from 50 µm thick photoetched stainless steel (Qualitech). Amplitude coding of feedback signals was achieved by adjusting their reflectivity at 635 nm using ink from commercial highlighter pens (Stabilo Boss, Schwan-Stabilo). Figure 4.4(a) shows the measured reflectivity for different ink colours, normalised to uncoated stainless steel. The results cover a useful range and allow reflectivity to be precisely controlled. The colours selected for this experiment were 501 neon green, 201 neon red, 23 neon pink, and bare stainless steel. Figure 4.4(b) shows a close-up of the optical arrangement, including the cantilever tip, the coded aperture, and the GRIN lens.

Figure 4.5(a-c) show the different aperture layouts investigated. Each aperture has a length of 2.25 mm and a width of 1.75 mm. To study the effect of aperture geometry, apertures with widths of 0.5 mm, 1.0 mm, and 1.5 mm were used, corresponding to normalised width values of 0.25, 0.5, and 0.75, respectively. Figure 4.5(d-f) show the

coated apertures after coating with the selected colours. In these apertures, the high-mode feedback is generated by reflectors with $R_0 = 1$ and $R_1 = 0.71$, while the low-mode feedback is generated using reflectors with $R_2 = 0.49$ and $R_3 = 0.21$.

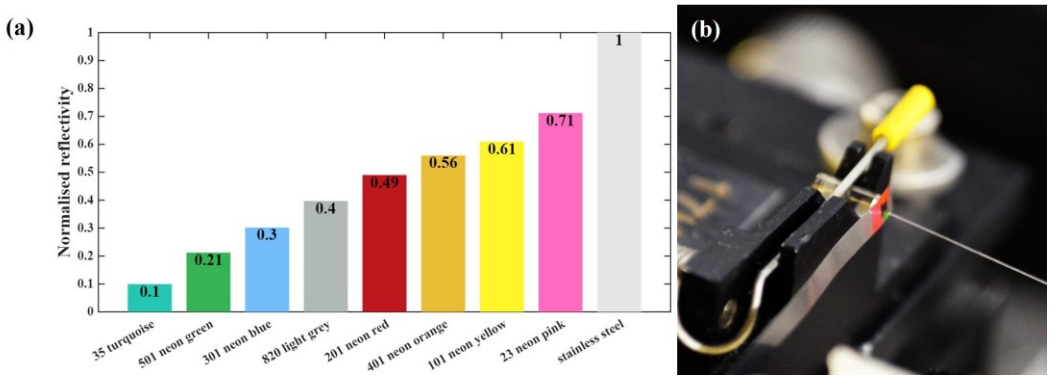


Fig. 4.4 (a) Normalised reflectivities using example pens and (b) photo of fibre tip.

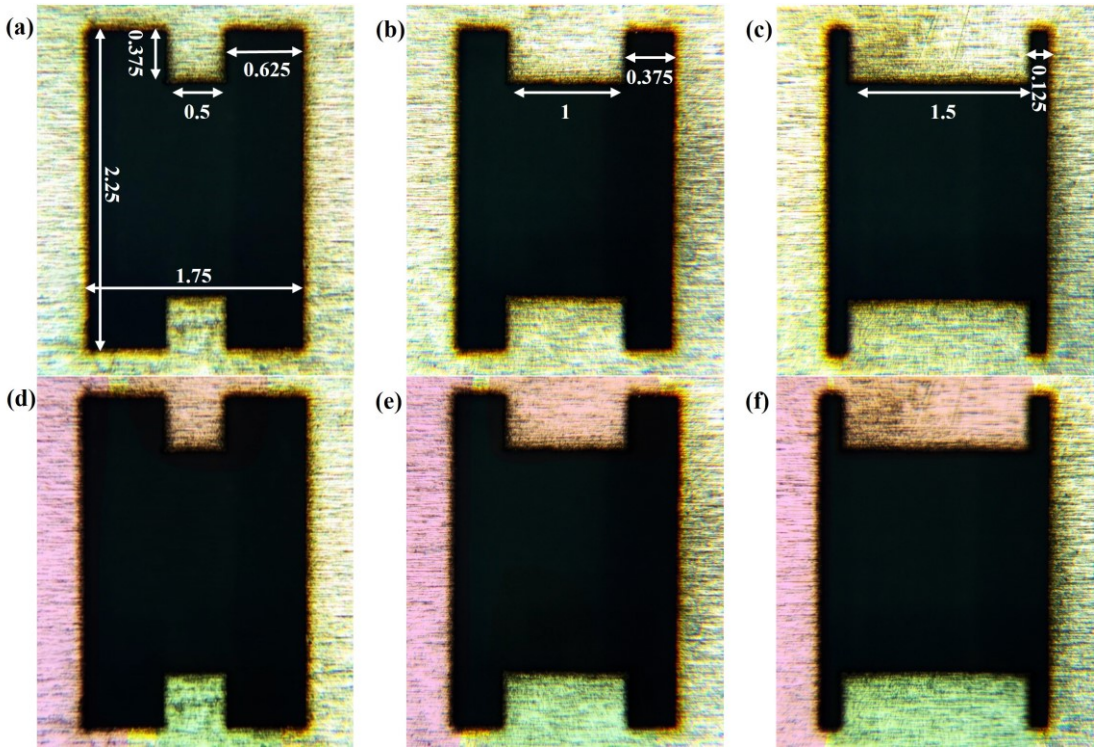


Fig. 4.5 Etched aperture for (a, d) $W = 0.25$, (b, e) $W = 0.5$ and (c, f) $W = 0.75$ (a-c) before and (d-f) after coating.

4.2 Experimental Scan Lines

Optical components were mounted on micro-positioners, and scan patterns were recorded using a camera. The parameter n was found to be tuneable over the range from 19 to 63. Outside this range, no feedback was obtained due to the low damping of

the cantilever and the limited drive voltage of the PT (±15 V). Wider tuning could be achieved by increasing the maximum drive voltage or by reducing the aperture size.

Figure 4.6 shows Lissajous figures obtained using an aperture with $W = 0.25$, assuming (a) $n = 21$, (b) $n = 41$ and (c) $n = 61$. In each case, the pattern is created automatically, and the scan line density increases monotonically from (a) to (c). The figures are all closed, and the scan amplitudes have been adjusted so that only small regions (black) are cropped by the reflecting aperture. Figures 4.7 and 4.8 show similar results obtained using apertures with $W = 0.5$ and $W = 0.75$, respectively.

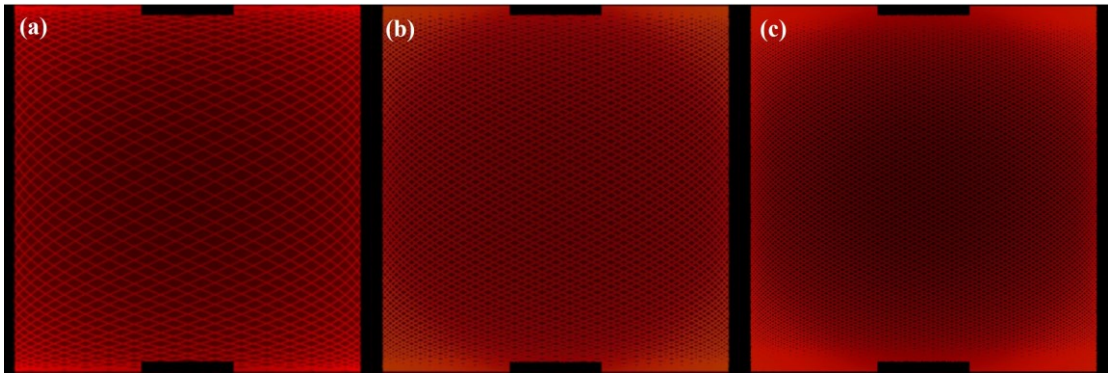


Fig. 4.6 Lissajous scans for $W = 0.25$ and n values of (a) 21, (b) 41 and (c) 61.

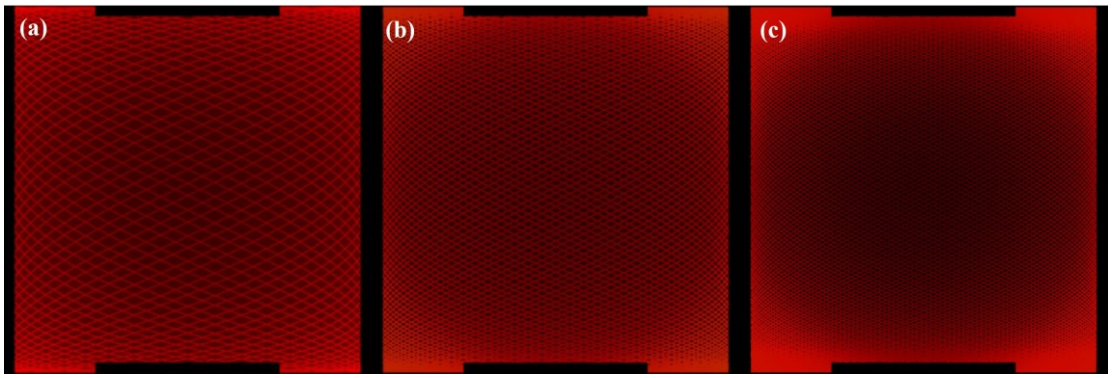


Fig. 4.7 Lissajous scans for $W = 0.5$ and n values of (a) 21, (b) 41 and (c) 61.

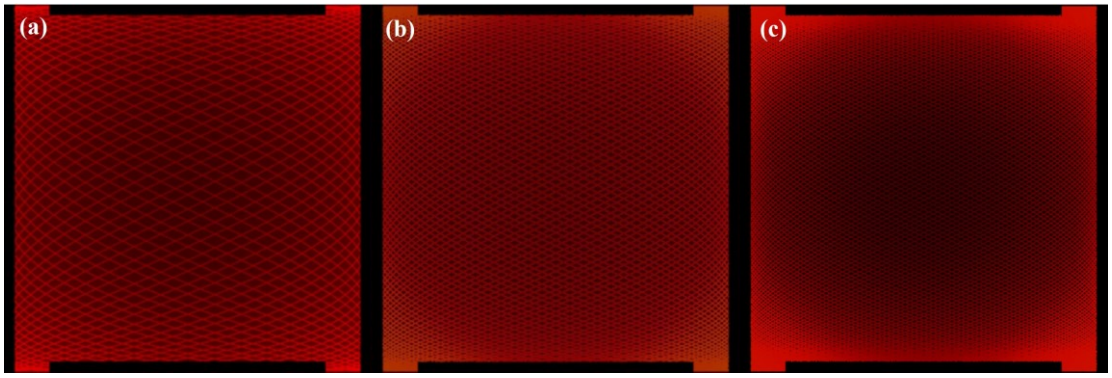


Fig. 4.8 Lissajous scans for $W = 0.75$ and n values of (a) 21, (b) 41 and (c) 61.

4.3 System Calibration

When the scanner is operating, two types of error may occur: setup errors and controller errors. Setup errors are caused by imperfections in the physical alignment of the system, such as reflector tilt or optical misalignment. Controller errors arise from unequal displacement amplitudes, which produce a non-square FOV, and from phase offsets, which cause mismatches between the backscattered signal and the position data.

4.3.1 Setup Error

During the scanner setup, two main types of error may occur: reflector tilt and fibre misalignment. In this section, these errors are identified and corrected by manually adjusting the micro-positioners. If the real-time controller operates ideally, both errors can be detected using the measured reflectivities $R_{0,1,2,3}$ and the corresponding duty cycles $D_{0,1,2,3}$ of the intermittent feedback signals.

Tilt Reflector

A tilted reflector changes the optical path lengths of the feedback beams reflected from the four sides of the aperture, which affects the measured reflectivities. As a result, the amplitudes of the pulse trains differ from the calibrated reflectivity values. Figure 4.4(a) shows the reference reflectivity values used for calibration. In this experiment, the expected reflectivity ratio from the four reflectors was $R_0 : R_1 : R_2 : R_3 = 1 : 0.71 : 0.49 : 0.21$, based on the selected colour coatings. Figure 4.9(a) shows that the measured reflectivity R_0 from the right side is lower, while the corresponding reflectivity R_1 from the left side is higher than the reference ratio. This indicates a rotation of the aperture about its vertical axis. In contrast, the top and bottom reflectivities R_2 and R_3 follow the expected reference ratio, indicating correct alignment in the vertical direction.

Misalignment

Misalignment between the fibre tip and the reflector leads to unequal duty cycles in the feedback signals. Assuming a positional offset of $[\Delta x, \Delta y]$, the thresholds for

generating intermittent feedback from the four reflectors become $T - \Delta x$, $T + \Delta x$, $T - \Delta y$ and $T + \Delta y$, respectively. As a result, the high-mode duty cycles are :

$$D_{0,1} = \frac{1}{\pi}\cos^{-1}\left(\frac{T \mp \Delta x}{B_h}\right) \tag{4.1}$$

From Eqn. (4.1), equal duty cycles occur only when $\Delta x = 0$. Since the feedback signals are pulse trains, their duty cycles can be measured directly using an oscilloscope or obtained from the amplitude control subsystem. For the top and bottom reflectors, the duty cycles are more complex due to the finite aperture width, and are given by:

$$D_{2,3} = \frac{1}{\pi^2}\cos^{-1}\left(\frac{T \mp \Delta y}{B_l}\right)\left[\sin^{-1}\left(\frac{W + \Delta x}{B_h}\right) - \sin^{-1}\left(\frac{-W + \Delta x}{B_h}\right)\right] \tag{4.2}$$

Equal duty cycles in this case occur only when both $\Delta y = 0$ and $\Delta x = 0$. Figure 4.9(b) shows the measured feedback signals, where the black and red traces correspond to the high-mode feedback and exhibit equal duty cycles of approximately 0.16. In contrast, the low-mode feedback signals show unequal duty cycles, indicating a vertical misalignment between the fibre tip and the reflector.

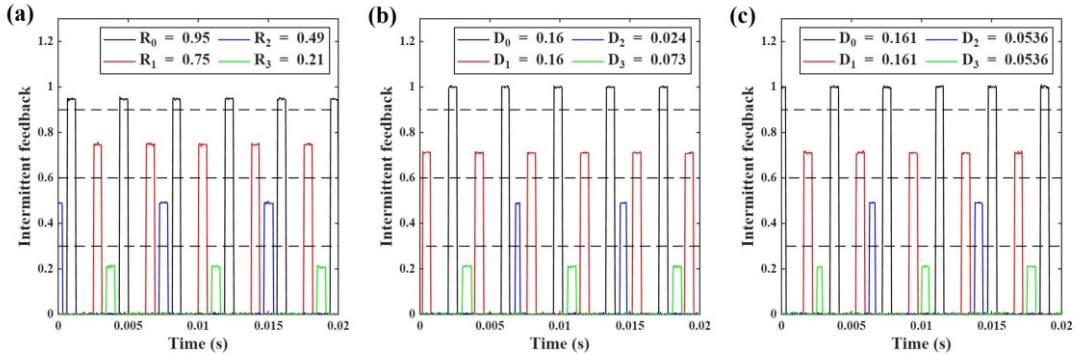


Fig. 4.9 Feedback signals for (a) tilt reflector, (b) misalignment and (c) unequal amplitude.

4.3.2 Controller Error

Controller errors occur when the controller does not operate correctly. Two types of error can arise: amplitude error and phase error. Amplitude error leads to unequal displacement, which produces a non-square FOV and distorts the reconstructed image. Phase error causes a mismatch between the image data and their corresponding position.

The unequal displacement of the two modes was analysed theoretically and investigated experimentally. Figure 4.9(c) shows the effect of this amplitude imbalance on the measured duty cycles. Although the duty cycles from the two modes appear aligned, their ratio differs from the value predicted by Eqn. (2.48). This confirms the presence of unequal displacement amplitudes between the two scanning modes.

The phase error cannot be obtained directly from the feedback signals and must be evaluated using the reconstructed image of a known target. To study this effect, a test target is designed. Assuming a perfect two-dimensional Lissajous trajectory with unit side length, the time-dependent coordinates (x, y) are given by:

$$\begin{bmatrix} x \\ y \end{bmatrix} = \begin{bmatrix} \sin(r\omega t) \\ \cos(\omega t) \end{bmatrix} \tag{4.3}$$

where r is the frequency ratio between two vibration modes. Phase errors in the horizontal and vertical directions arise from imperfect control of the fibre scanner. In this case, the actual trajectory becomes:

$$\begin{bmatrix} x' \\ y' \end{bmatrix} = \begin{bmatrix} \sin(r\omega t + \phi_x) \\ \cos(\omega t + \phi_y) \end{bmatrix} \tag{4.4}$$

where ϕ_x and ϕ_y represents the phase errors in the horizontal and vertical directions, respectively. Expanding and rearranging using trigonometric identities gives:

$$\begin{bmatrix} x' \\ y' \end{bmatrix} = \begin{bmatrix} x\cos(\phi_x) \pm \sqrt{1-x^2}\sin(\phi_x) \\ y\cos(\phi_y) \pm \sqrt{1-y^2}\sin(\phi_y) \end{bmatrix} \tag{4.5}$$

Eqn. (4.5) shows that the reconstructed image of the target is split, with the separation and offset determined by the phase errors and the original target position. Figure 4.10(a) shows the calibration target designed to measure and analyse the phase error.

The effect of phase errors is analysed under the assumption that the entire target lies within the FOV. The nominal target position is defined by the centre coordinate (x_0, y_0) of the cross. After reconstruction, Figure 4.10(b) shows that the target appears divided into four parts. The central coordinates of the four reconstructed crosses are denoted as (x_{LU}, y_{LU}), (x_{RU}, y_{RU}), (x_{LL}, y_{LL}) and (x_{RL}, y_{RL}). Since these centres are

difficult to locate, they are calculated from the measured positions of the horizontal and vertical strips.

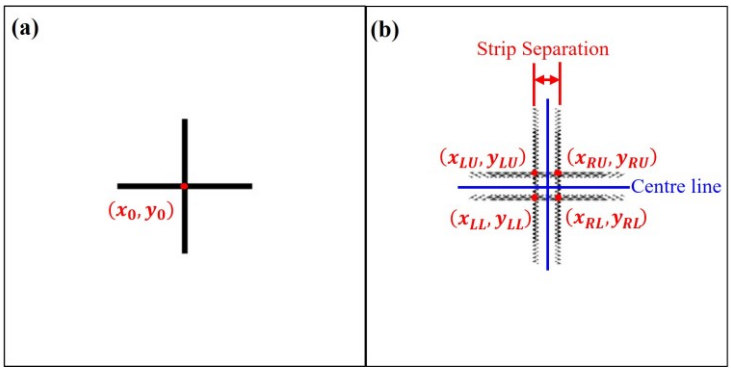


Fig. 4.10 (a) Calibration target and (b) simulated reconstructed target with phase errors.

The central positions and strip separations can be derived from Eqn. (4.5). Assuming a small phase error, the small-angle approximation can be applied, giving:

$$\begin{bmatrix} \frac{x_{LU} + x_{RU}}{2} \\ \frac{y_{LU} + y_{LL}}{2} \end{bmatrix} = \begin{bmatrix} x_0 \cos(\phi_x) \\ y_0 \cos(\phi_y) \end{bmatrix} \approx \begin{bmatrix} x_0 \\ y_0 \end{bmatrix} \tag{4.6}$$

$$\begin{bmatrix} x_{LU} - x_{RU} \\ y_{LU} - y_{LL} \end{bmatrix} = \begin{bmatrix} 2\sqrt{1 - x_0^2}\sin(\phi_x) \\ 2\sqrt{1 - y_0^2}\sin(\phi_y) \end{bmatrix} \approx \begin{bmatrix} 2\sqrt{1 - x_0^2}\phi_x \\ 2\sqrt{1 - y_0^2}\phi_y \end{bmatrix} \tag{4.7}$$

The left-hand sides of Eqns. (4.6) and (4.7) can be measured from the reconstructed images, allowing the phase errors ϕ_x and ϕ_y to be determined. Since the sine function is monotonic within the range $-\pi/2 < \phi < \pi/2$, a unique solution exists.

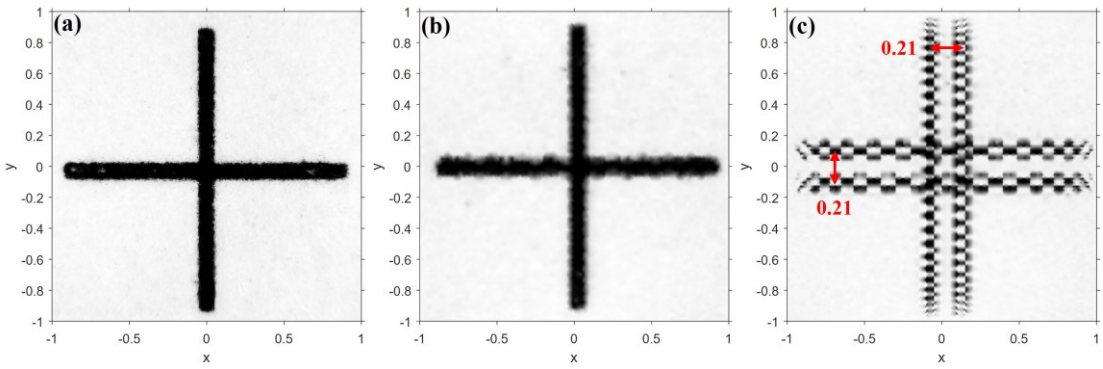


Fig. 4.11 Microscopic image and image reconstruction (a) with and (b) without phase error.

The theoretical analysis of the phase error effect on image reconstruction was verified experimentally. Figure 4.11 shows the results. Figure 4.11(a) shows the original

reference image acquired using a microscope. When the target is imaged using the fibre scanner with a correctly operating controller, phase errors are removed, and an accurate reconstruction is obtained, as Figure 4.11(b) shows. A phase offset of 6° was then introduced in both scanning directions. The resulting reconstructed image is shown in Figure 4.11(c). The measured strip separations in this image are approximately 0.21, which corresponds to a 6° phase error, as predicted by Eqn. (4.7).

4.4 Image Reconstruction

In this section, the image reconstruction process is described after both the imaging data and positional data have been collected. The reconstruction links the image intensity values, obtained from the backscattered signal to their corresponding spatial positions. This allows the intensity of the full target to be reconstructed beyond the sampled points. Theoretical aspects of Lissajous scanning and sampling are then introduced to support the reconstruction method. Computational techniques used in the reconstruction, including Delaunay triangulation [132-133] and Padua points [134], are also discussed. Finally, reconstructed images obtained when the real-time controller operates in both transient and steady-state conditions are presented and analysed.

4.4.1 Sampling

We first derive some properties of the Lissajous curve, extending the introduction in Chapter 1. A Lissajous curve is formed when two non-degenerate vibration modes oscillate sinusoidally at different frequencies. The displacements are defined in Eqn. (4.3). If the motion along the x-axis oscillates at a higher frequency, the frequency ratio is given in Eqn. (1.24). The periods T_x and T_y of the x- and y-motions are:

$$\begin{bmatrix} T_x \\ T_y \end{bmatrix} = \begin{bmatrix} n/f \\ 1/f \end{bmatrix} \tag{4.8}$$

The common period of the two motions is the least common multiple, which is n/f. This shows that the Lissajous trajectory is continuous and periodic. To examine whether the trajectory is smooth, the first derivatives of the displacements are calculated as:

$$\begin{bmatrix} \frac{dx}{dt} \\ \frac{dy}{dt} \end{bmatrix} = \begin{bmatrix} 2\pi rf \times \cos(2\pi rft) \\ -2\pi f \times \sin(2\pi ft) \end{bmatrix} \tag{4.9}$$

The zero-crossings of these derivatives are $[(2k+1)/4rf\,, k/2f]$, where k is a non-negative integer. For even values of n, some values of $t_{x,y}$ coincide, which momentarily stops the motion and creates a discontinuity in the trajectory. Therefore, n must be an odd integer to ensure a smooth and continuous Lissajous scanning pattern.

Figure 4.12 shows the distribution of Padua points and the corresponding Delaunay triangulation for different values of m. Figure 4.12(a) shows the Padua points, indicated by red dots, located at the self-intersection points of the Lissajous trajectory [134]. During triangulation, Figure 4.12(b) shows how these points are connected to form non-overlapping triangles. Within each triangle, the intensity values are interpolated from the values at the three vertices [132-133]. This allows a non-Cartesian 2D map to be reconstructed onto a regular Cartesian grid. When m increases from 2 to 3, Figure 4.12(c) shows that the triangles change from equilateral to more isosceles shapes. This reduces the uniformity of the interpolation and lowers the overall accuracy. In summary, the best reconstruction performance is achieved when $m = 2$ and n is a positive odd integer. In this section, the theory for sampling at Padua points is extended to the general case where m is any positive integer.

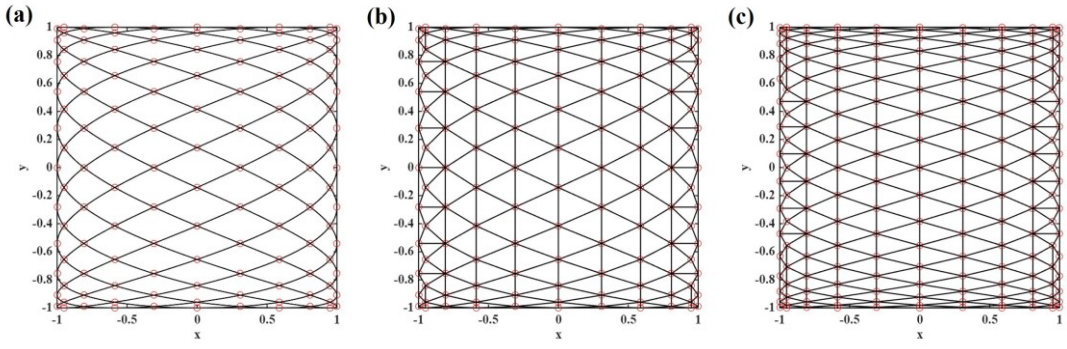


Fig. 4.12 (a) Lissajous curve and Padua points and (b) Delaunay triangulation with $m = 2$; and (c) Delaunay triangulation with $m = 3$.

We now discuss how to sample at the Padua points. From Eqn. (4.3), let the Lissajous trajectory reach a Padua point at time t_i, where i is an integer index. Since

Padua points are located at the self-intersections of the trajectory, the curve passes through each point at least twice, separated by a time interval Δt_i. Rearranging Eqn. (4.3) gives the coordinates of the Padua points as:

$$\begin{bmatrix} x_i \\ y_i \end{bmatrix} = \begin{bmatrix} \sin(2\pi r f t_i) \\ \cos(2\pi f t_i) \end{bmatrix} = \begin{bmatrix} \sin(2\pi r f t_i + 2\pi r f \Delta t_i) \\ \cos(2\pi f t_i + 2\pi f \Delta t_i) \end{bmatrix} \tag{4.10}$$

Expanding and rearranging Eqn. (4.10) gives two sets of solutions in the x-direction:

$$\Delta t_i = \frac{nj}{f(mn+1)} \tag{4.11}$$

$$\Delta t_i = \frac{n(2l+1)}{2f(mn+1)} - 2t_i \tag{4.12}$$

where j and l are integers. Similarly, two sets of solutions are obtained in y-direction:

$$\Delta t_i = p/f \tag{4.13}$$

$$\Delta t_i = q/f - 2t_i \tag{4.14}$$

where p and q are integers. To find values of t_i, for which both the x- and y-coordinates coincide, four possible cases are considered.

Case 1

Equating Eqn. (4.11) and Eqn. (4.13) gives:

$$nj = p(mn+1) \tag{4.15}$$

Since n and $(mn+1)$ are coprime, the solutions are $j = k(mn+1)$ and $p = kn$, where k is an integer. Substituting gives

$$\Delta t_i = \frac{kn}{f} \tag{4.16}$$

When $k = 0$, $\Delta t_i = 0$ (stationary). For $k \geq 1$, $\Delta t_i = kn/f$, corresponding to integer multiples of the cycle period. Hence, these do not represent Padua points.

Case 2

Equating Eqn. (4.11) and Eqn. (4.14) gives:

$$t_i = \frac{q}{2f} - \frac{nj}{2f(mn+1)} = \frac{1}{2f(mn+1)}[q(mn+1) - nj] \tag{4.17}$$

Let $s = q(mn+1) - nj$. Since q, m, n, j are integers, s is also an integer. If $q = n + s$ and $j = qm + 1 = mn + sm + 1$, Eqn. (4.17) is satisfied. The corresponding solutions are:

$$\Delta t_i = \left[\frac{mn^2 + smn + n}{f(mn+1)}\right]_{\frac{n}{f}} = \frac{n}{f}\left(\frac{sm}{mn+1}\right) \tag{4.18}$$

$$t_i = \frac{s}{2f(mn+1)} \tag{4.19}$$

Here s must not be zero or a multiple of $mn + 1$ to describe Padua points. In this case, the minimal time interval between passing through a Padua point is $nm/[f(mn+1)]$, and the regular spacing between consecutive Padua points is $1/[2f(mn+1)]$. These values determine the minimum sampling rate and the required starting point for the fibre trajectory to pass through all Padua points in this case.

Case 3

Equating Eqn. (4.12) and Eqn. (4.13) gives:

$$t_i = \frac{n(2l+1)}{4f(mn+1)} - \frac{p}{2f} = \frac{1}{4f(mn+1)}[n(2l+1) - 2p(mn+1)] \tag{4.20}$$

Since n, l, p, m are integers, the term $n(2l+1) - 2p(mn+1)$ is also an integer. The term $n(2l+1)$ is odd, while $2p(mn+1)$ is even, so their difference must be odd. We therefore define $2u + 1 = n(2l+1) - 2p(mn+1)$ where u is an integer. If $p = (n - 1 - 2u)/2$ and $l = pm$, then Eqn. (4.20) is satisfied. The solutions are:

$$\Delta t_i = \frac{n - 1 - 2u}{2f} \tag{4.21}$$

$$t_i = \frac{2u+1}{4f(mn+1)} \tag{4.22}$$

In this case, $u \neq [(2v+1)n - 1]/2$. The minimum time interval is $\Delta t_{i,min} = 1/f$, and the regular spacing between consecutive Padua points is $1/[4f(mn+1)]$.

Case 4

Equating Eqn. (4.12) and Eqn. (4.14) gives:

$$\frac{n(2l+1)}{2f(mn+1)} = \frac{q}{f} \tag{4.23}$$

Simplifying this expression gives:

$$n(2l+1) = 2q(mn+1) \tag{4.24}$$

The left-hand side of Eqn. (4.24) is always odd, while the right-hand side is always even. Therefore, this equation has no valid solution.

Summary

Combining all cases, the trajectory passes through the Padua points at times:

$$t_i = \frac{i}{4f(mn+1)} \tag{4.25}$$

subject to the following restrictions:

$$\begin{cases} i \neq 0 \\ i \neq [(2w+1)n-1]/2 \\ i \neq w(mn+1) \end{cases} \tag{4.26}$$

where w is an integer. In practice, since the sampling rate of the acquisition system is uniform, it is not possible to skip the time points specified in Eqn. (4.26). To ensure that all Padua points are captured, the sampling interval must be smaller than both the minimum time interval between consecutive Padua points and $\Delta t_{i,min}$. For simplicity, the sampling sequence used for the Lissajous fibre scanner is selected as

$$t_s = 0{:}\frac{1}{4f(mn+1)}{:}\frac{n}{f} \tag{4.27}$$

This guarantees complete coverage of all Padua points within a single cycle.

4.4.2 Transient and Steady-State Imaging

Optical imaging was performed using a nickel electroplated micro-actuator with anchors, suspended beams, and comb electrodes as the target, kindly loaned by Prof. A.S. Holmes of the Optical and Semiconductor Devices Group. The nominal minimum feature size of the structure is approximately 10 μm, although additional surface granularity caused by the electroplating process is visible. Figure 4.13(a) shows the reconstructed image obtained using a Lissajous scan pattern with a sampling rate defined in Eqn. (4.27), corresponding to the scan in Figure 4.7(a). Figure 4.13(b-d) shows intermediate images acquired during the transition from $n = 21$ to $n = 41$.

The initial state corresponds to the stable image in Figure 4.13(a), while Figure 4.13(b-c) shows transient images captured before the high-mode amplitude correction, high-mode displacement estimation, and phase-synchronisation loops have fully converged. As the control loops stabilise, the reconstructed image gradually becomes clearer, and the final steady-state image is shown in Figure 4.14(a). Figures 4.14(b-d) show intermediate images during the transition from $n = 41$ to $n = 61$, with the final steady-state image shown in Figure 4.15(a). To the best of our knowledge, these results show the first demonstration of dynamically programmable fibre scanning. During this process, the frame rate is reduced by a factor of three, from 6.26 FPS to 2.16 FPS, showing the trade-off between resolution and frame rate when varying the scan pattern.

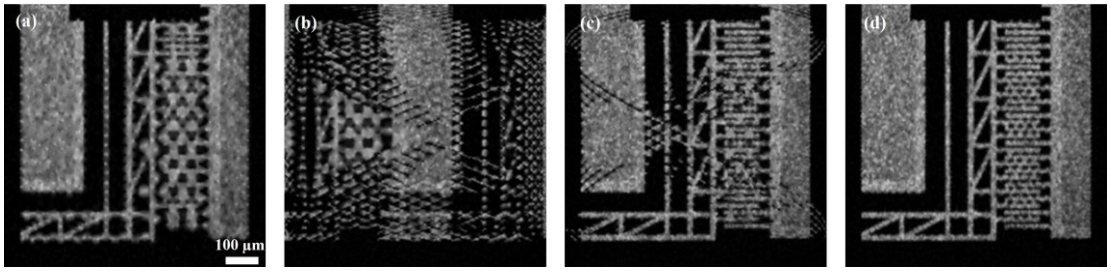


Fig. 4.13 Reconstructed images for $W = 0.5$ during switching from stable imaging with (a) $n = 21$ to $n = 41$ via (b) high mode amplitude correction, (c) high mode displacement estimation, and (d) phase synchronisation. Nickel plated MEMS object courtesy Prof. A.S. Holmes, Imperial College London.

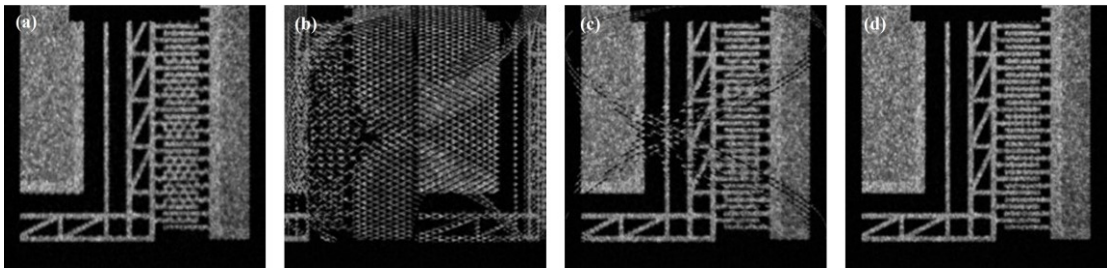


Fig. 4.14 Reconstructed images for $W = 0.5$ during switching from stable imaging with (a) $n = 41$ to $n = 61$ via (b) high mode amplitude correction, (c) high mode displacement estimation, and (d) phase synchronisation

Figure 4.15(b) shows an enhanced-resolution image obtained by combining signals acquired from $n = 21$ to $n = 61$ in steps of 20. By merging images from multiple Lissajous scan patterns, the characteristic Lissajous zigzag artefact is effectively reduced. Figure 4.15(c) shows an over-sampled reconstruction in which the sampling

rate is doubled. However, the Lissajous artefact is still visible, showing that over-sampling alone does not provide additional benefit for suppressing this artefact. Figure 4.15(d) shows the original microscopic image of the target for reference.

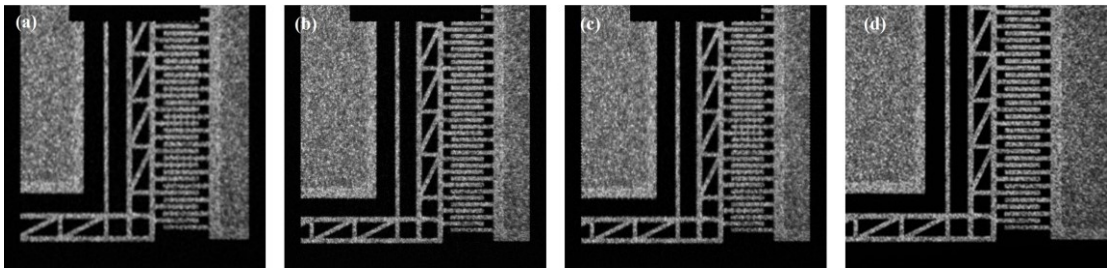


Fig. 4.15 Reconstructed images for $W = 0.5$ with (a) $n = 61$, (b) enhanced resolution, (c) over-sampling and (d) microscopic image.

4.4.3 Other Samples

Figure 4.16(a) shows the microscopic image of a micro-turbine structure composed of multiple straight edges, again kindly loaned by Prof. Holmes. Figure 4.16(b-c) show the reconstructed images obtained using different Lissajous scan settings. In these images, a similar Lissajous zigzag artefact is observed for values of n from 21 to 61, which agrees with the observations in the previous section. Figure 4.16(d) shows that the Lissajous artefact is significantly reduced in the enhanced-resolution reconstruction.

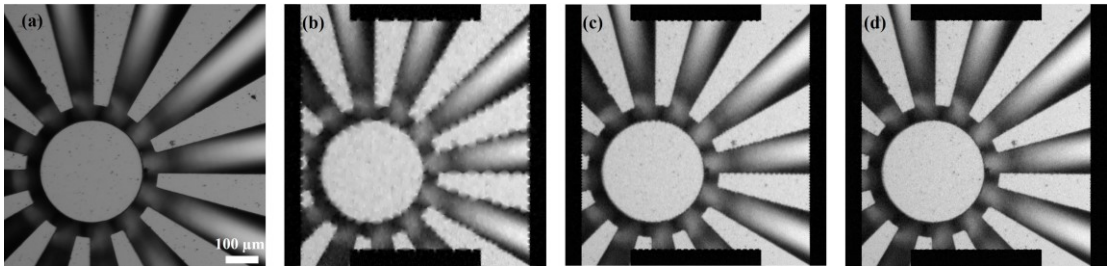


Fig. 4.16 (a) Original microscopic image; reconstructed images with $W = 0.5$ and (b) $n = 21$, (c) $n = 61$, and (d) enhanced resolution of a micro-turbine. Micro-turbine courtesy Prof. A.S. Holmes, Imperial College London.

Figure 4.17(a) shows the microscopic image of a prepared slide of a honeybee worker leg composite (Set B, United Scope LLC). Figure 4.17(b-d) show the reconstructed images for $n = 21$, $n = 61$, and the enhanced-resolution case. These reconstructions achieve good spatial resolution, as the biological structures do not have sharp edges like MEMS devices, making resolution improvement more apparent.

However, for biological specimens, colour is important for distinguishing structural features. When fluorescent or histological dyes are used, coloured image reconstruction becomes necessary for visual clarity and for rapidly identifying regions of interest.

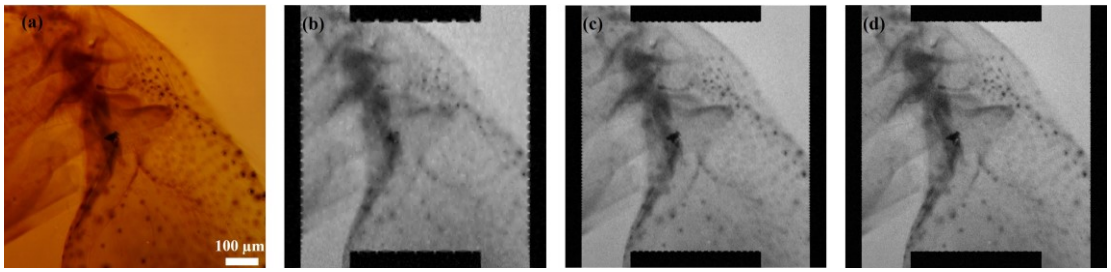


Fig. 4.17 (a) Original microscopic image; reconstructed images with $W = 0.5$ and (b) $n = 21$, (c) $n = 61$, and (d) enhanced resolution of a prepared slide of honeybee worker leg-composite.

4.5 Conclusion

In this chapter, the complete 2D Lissajous fibre scanning system was demonstrated. The full system configuration, including the amplitude-coded reflecting aperture, imaging optics, and fibre mounting, was presented together with the real-time controller described in Chapter 3. Photographs of the scan trajectories confirmed that symmetric, square fields of view can be achieved. Setup-related errors, such as reflector tilt and fibre misalignment, were identified using measured reflectivities and duty cycles, and corrected using micro-positioners. Controller-related errors, including amplitude imbalance and phase offsets, were analysed both theoretically and experimentally. This chapter also introduced the theory of Lissajous sampling, including the derivation of Padua point locations and the use of Delaunay triangulation to reconstruct images from non-uniform samples. During dynamic reprogramming of the scan parameters, intermediate images showed how the control loops converge. Under steady-state operation, the scanner produced high-quality images, and enhanced-resolution reconstructions were obtained by combining data from multiple scan patterns.

Chapter 5: Multi-Wavelength Lissajous Fibre Scanner using Photonic Crystal Fibres

In this chapter, a Lissajous fibre scanner based on PCFs [121-122] with mode-stripping and multi-wavelength, dual NA confocal detection [52] is presented. The PCFs are dip-coated in polymer to form a dual-cylindrical structure that supports two non-degenerate, orthogonal bending modes. During fabrication, the fibres are held parallel using silicon V-grooves, and the open ends are sealed with UV-curing epoxy. This coating process is repeatable and controllable, allowing dense and stable Lissajous scan patterns to be generated under piezoelectric excitation. Compared with the earlier dip-coating method [69], the modified procedure allows dual-core structures to be fabricated using holey fibres. The performance of mode-stripping detection of the PCFs is characterised using a monochromator and a multi-channel PD, with SMFs used as a reference. A 2D Lissajous fibre scanner is then built using the coated PCF and RGB laser sources. Coloured coatings on a metal aperture provide wavelength-selective, amplitude-coded optical feedback, allowing the x- and y-motions to be distinguished under either monochromatic blue illumination or multiplexed RGB operation. This enables real-time switching between fluorescence imaging and full-colour imaging. Fluorescence imaging is demonstrated using test objects and biological specimens (a USAF 1951 resolution target, and spinach tissue soaked in ethanol). Full-colour imaging is achieved by calibrating the multi-channel PD responses using a ColorChecker, producing reconstructed images that closely match those obtained with a microscope. The overall system performance is further validated by imaging a similar range of target objects (stamps, banknotes and a mounted biological microscope specimens).

5.1 Fibre Fabrication

The density of the Lissajous pattern is determined by the ratio between the resonant frequencies of two orthogonal fibre bending modes. Let the non-degenerate resonant frequencies along the x- and y-axes be denoted as ω_x and ω_y, respectively. If $\omega_x > \omega_y$, the frequency ratio can be expressed as $\omega_x/\omega_y = m + 1/n$, where m and n are

two positive integers. While $m = 2$ is sufficient to decouple the modes, a large and odd value of n improves the scanning density.

5.1.1 Theoretical Resonant Frequency Ratio

Figure 5.1 shows the cross-sections and resonant frequency ratios of dual-core PCFs with different fibre orientations before dip-coating. The cross-sections are based on a COTS PCF (LMA-8, NKT Photonics). The resonant frequency ratio of two identical cylindrical fibres is calculated in Eqns. (3.2-3.3). The contribution from the air holes is calculated by applying the parallel axis theorem to the coordinates of each hole centre. Figure 5.1(a) shows the cross-section of two fibres oriented at 0° without dip-coating. For the PCF cantilever, the resulting value is $n = 5$, which is higher than that obtained for bare SMFs ($n = 3$). This difference arises because, unlike the circular cladding of an SMF, the PCF contains a hexagonal array of airholes forming the inner cladding.

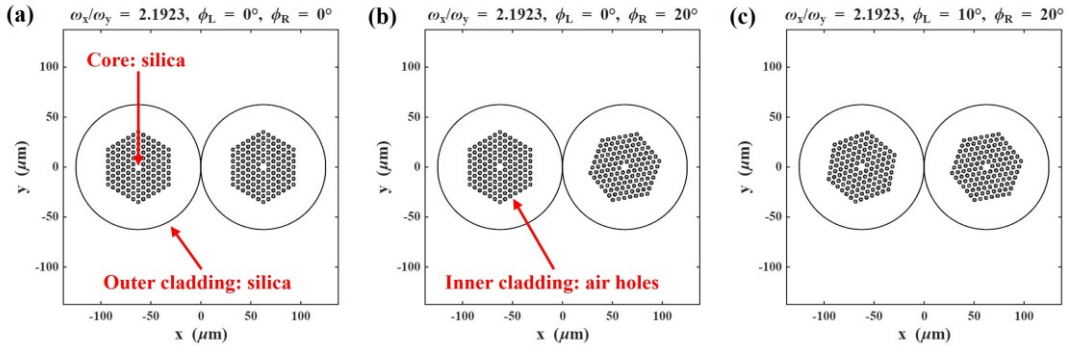


Fig. 5.1 Theoretical cross-sections and resonant frequency ratios of dual-core PCFs with (a) no core, (b) a single core, and (c) both cores oriented prior to dip-coating with a polymer fillet.

Figure 5.1(b) and Figure 5.1(c) show the effect of fibre orientation on the resonant frequency ratio. The ratio remains unchanged with rotation, owing to the rotational symmetry of the structure about its centroid. This result can be shown analytically and numerically for the hexagonal lattice used here, and it also applies to any regular polygonal hole arrangement. Because the fibres themselves have circular outer claddings, the PMMA fillet formed during dip-coating is symmetric about the principal axes and therefore does not affect the frequency ratio. As a result, rotation of the fibres about their axes has no influence on the resonant behaviour, which greatly simplifies the fabrication process. After dip-coating with polymethyl methacrylate (PMMA; 950

PMMA A6, MicroChem), Figure 5.2 shows the polymer forms a fillet. This reduces the resonant frequency ratio to below 2, indicating that large values of n can be achieved.

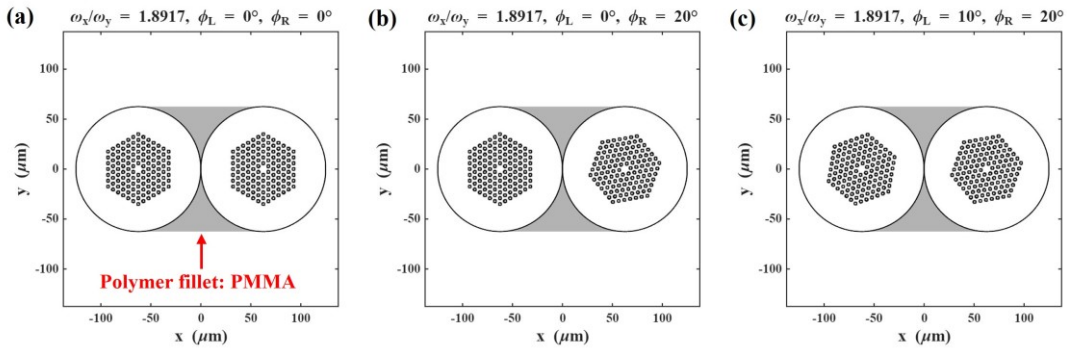


Fig. 5.2 Theoretical cross-sections and resonant frequency ratios of dual-core PCFs with (a) no core, (b) a single core, and (c) both cores oriented after dip-coating with a polymer fillet.

Orientation independence of second moments for PCF

Here we provide a mathematical proof that the angular orientation of the regular air-hole lattice in a PCF has no effect on its second moment of area. The contribution from the air holes can be evaluated using the parallel axis theorem. Since all holes have identical cross-sectional areas, their total contribution depends only on the sum of their squared distances from the centre coordinates to the principal axes under different orientations. Because the air hole positions can be separated into multiple regular hexagons, we provide the following general proof for a regular polygon.

Let α denote the distance from the centre of a regular polygon to its vertices. A regular N-sided polygon can be split into N isosceles triangles with vertex angle:

$$\theta = \frac{2\pi}{N} \tag{5.1}$$

For a polygon rotated by an angle β, the coordinates of n-th vertex are:

$$\begin{bmatrix} x_n \\ y_n \end{bmatrix} = \alpha \begin{bmatrix} \cos\left(\beta + \frac{2n\pi}{N}\right) \\ \sin\left(\beta + \frac{2n\pi}{N}\right) \end{bmatrix}_{n=0.1\ldots,N-1} \tag{5.2}$$

Using trig. identities, the total squared distance of all vertices to the principal axes are:

$$\sum_{n=0}^{N-1} x_n^2 = \alpha^2 \sum_{n=0}^{N-1} \cos^2\left(\beta + \frac{2n\pi}{N}\right) = \frac{n\alpha^2}{2} + \frac{\alpha^2}{2} \sum_{n=0}^{N-1} \cos\left(2\beta + \frac{4n\pi}{N}\right) \tag{5.3}$$

$$\sum_{n=0}^{N-1} y_n^2 = \alpha^2 \sum_{n=0}^{N-1} \sin^2\left(\beta + \frac{2n\pi}{N}\right) = \frac{n\alpha^2}{2} - \frac{\alpha^2}{2} \sum_{n=0}^{N-1} \cos\left(2\beta + \frac{4n\pi}{N}\right) \tag{5.4}$$

Applying the trigonometric angle-sum identity yields:

$$\sum_{n=0}^{N-1} \cos\left(2\beta + \frac{4n\pi}{N}\right) = \cos(2\beta) \sum_{n=0}^{N-1} \cos\left(\frac{4n\pi}{N}\right) - \sin(2\beta) \sum_{n=0}^{N-1} \sin\left(\frac{4n\pi}{N}\right) \tag{5.5}$$

Using Lagrange's trigonometric identity for equally spaced angles [135] gives:

$$\sum_{n=0}^{N-1} \cos\left(\frac{4n\pi}{N}\right) = \frac{-\sin\left(\frac{2\pi}{N}\right) + \sin\left(4\pi - \frac{2\pi}{N}\right)}{2\sin\left(\frac{2\pi}{N}\right)} + \cos(0) = 0 \tag{5.6}$$

$$\sum_{n=0}^{N-1} \sin\left(\frac{4n\pi}{N}\right) = \frac{\cos\left(\frac{2\pi}{N}\right) - \cos\left(4\pi - \frac{2\pi}{N}\right)}{2\sin\left(\frac{2\pi}{N}\right)} = 0 \tag{5.7}$$

Substituting Eqns. (5.6-5.7) into Eqns. (5.3-5.4) gives:

$$\sum_{n=0}^{N-1} x_n^2 = \frac{n\alpha^2}{2} \tag{5.8}$$

$$\sum_{n=0}^{N-1} y_n^2 = \frac{n\alpha^2}{2} \tag{5.9}$$

Thus, the total squared distance from the vertices of a regular polygon to the principal axes is independent of rotation. This result therefore applies directly to the hexagonal air-hole structure of the PCF. The upper text captions in Figures 5.1 and 5.2 show numerical simulation results that confirm this invariance: changing the orientation of the PCF cross-section does not affect the second moment of area.

5.1.2 Dip-Coating

Because the air holes in PCFs can be filled by capillary action, the previous dip-coating procedure [69] was modified. Figure 5.3(a) shows a step-by-step schematic of the revised method, and Figure 5.3(b-f) show photographs of the key stages. In step (i), the two fibres are stripped, cleaved, and mounted in an etched silicon V-groove array.

Figure 5.3(b) shows a top view of the mounted fibres and a side view of the grooved substrate. The substrate size is kept small (3 mm × 6 mm) to reduce its effect on later coating steps. The fibres are placed in triangular grooves (width: 0.4 mm, gap: 0.2 mm, depth: 0.3 mm) to ensure horizontal alignment and are fixed in place using epoxy. Figure 5.3(c) shows the aligned fibre tips. In step (ii), the fibre tips are sealed using a UV-curing epoxy (NOA 71, Edmund Optics). The epoxy volume is kept to a minimum while still fully covering the tip without forming beads. Figure 5.3(d) shows the sealed tips before curing. The epoxy is cured only after the fibre tips are aligned under a microscope. In step (iii), the fibres are coated while being withdrawn from the polymer solution, and capillary forces maintain their alignment. Figure 5.3(e) shows the coated fibre tip, which exhibits minimal disturbance from the blocking epoxy. In step (iv), the coated fibre is cleaved to produce a smooth, flat end face. Figure 5.3(f) shows the final fibre tip after cleaving. Figure 5.4(a) shows the cross-section of a PCF before dip-coating. Figure 5.4(b) shows the cross-section of a dip-coated dual-core PCF with a PMMA fillet and unblocked air holes produced using this procedure.

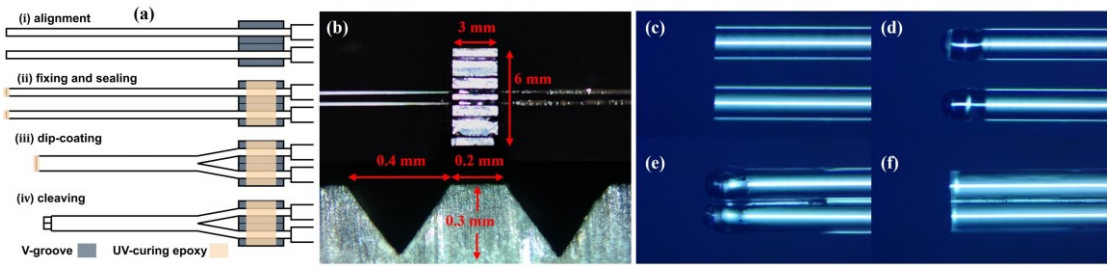


Fig. 5.3 (a) Dip-coating procedure for fabricating a dual-core PCF; (b) top view of dual fibres on the V-groove at step i and side view of the V-groove; (c-f) top views of the fibre tip at steps i-iv.

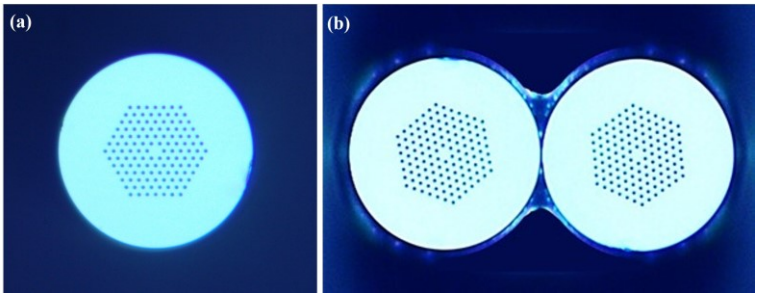


Fig. 5.4 Cross-section of a (a) single-core PCF and (b) a dual-core PCF after dip-coating

Figure 5.5(a-b) show experimental results from the dip-coating process. Coating speed is determined by the motor voltage. Figure 5.5(a) shows a linear relationship between

the resonant frequency ratio and this voltage, while Figure 5.5(b) shows the corresponding values of n. The black solid line represents the best-fit curve based on experimental samples at different voltage levels. Twenty sets of dip-coating process are conducted at each voltage, and the error bars represent the standard deviation of the resulting resonant frequency ratios and the values of n. Values of n from 21 to 51 are indicated by coloured data points. Higher voltages result in thinner PMMA layers and lower values of n. However, this relationship is valid only for voltages above 4.5 V. Although the theoretical model suggests an unbounded upper limit for n, the coating process becomes unreliable at lower voltages and the error increases. With current equipment, cantilevers with $n = 51$ can be reliably fabricated.

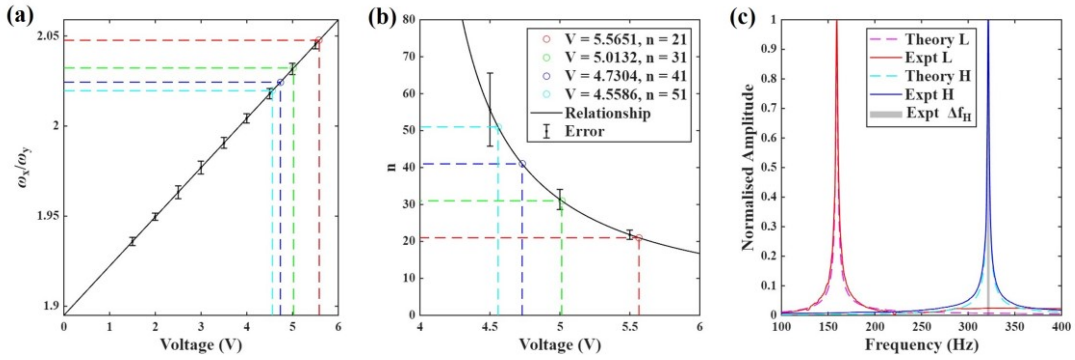


Fig. 5.5 (a) Dip-coating procedures for fabricating a dual-core PCF; (b) top view of dual fibres on the V-groove at step i and side view of the V-groove; (c-f) top views of the fibre tip at steps i-iv.

As previously discussed, the twin fibre fabrication process yields a uniform cross-section, allowing cantilevers of any length. A length of 3 cm was selected to generate resonant frequencies and scan amplitudes matching the performance of our real-time controller. Figure 5.5(c) shows the normalised frequency response of this cantilever (solid lines), together with theoretical fits (dotted). The low-mode and high mode resonances are $f_{l0} = 159.2Hz$ and $f_{h0} = 321.5Hz$, and the corresponding damping ratios are $\zeta_l = 0.0054$ and $\zeta_h = 0.0025$, equating to Q-factors of $Q_l = 92.6$ and $Q_h = 200$. The latter values determine the range of Lissajous figures that can be generated before scan amplitudes reduce so far that optical feedback is lost. The aim here was to optimise this range and hence maximise the frame rate for rapid image acquisition and the line density for high-resolution scanning. The values chosen allow

operation over n values from 35 to 93, corresponding to an approximate 3-fold range in scan density. The frame rate f_{l0}/n then also has an approximate 3-fold range.

Clearly, any fibre cantilever fabrication process that yields the same resonant frequency ratio and damping factors must allow the same performance. The advantage of the twin-fibre process over methods involving D-shaped cross-sections [64-65] or mechanical assembly [66-68] is that minimisation of surface energy of the liquid coating generates the correct ratio automatically from many available fibre types. The process is easily scalable to batch fabrication, and a continuous coating process analogous to that used for forming ribbon fibre is entirely conceivable.

5.2 Multi-wavelength Mode-Stripping Detection Measurement

We characterise the multi-channel PDs for mode-stripping detection with 3 objectives:

1. To compare the responses from direct detection and mode-stripping detection.
2. To verify that the cladding mode can traverse the absorption layers of the PDs.
3. To analyse the effect of PD configurations on the mode-stripping response.

Figures 5.7-5.9 show the performance of multi-wavelength mode-stripping detection using SMFs (SM600, Thorlabs) and PCFs.

Light Source Calibration

To measure the spectral response of the PDs, an illuminator (MI-150, Dolan-Jenner Industries) is used as a broadband light source, and a monochromator (M300, Bentham) is used to select individual wavelengths. A spectrometer (USB2000+, Ocean Optics) measures the spectra at both the input and output of the monochromator to account for its non-linear spectral response. The input spectrum is measured by aligning the spectrometer directly with the illuminator. Figure 5.6(a) shows the experimental setup used to measure the monochromator output spectra for different light sources. The selected source is coupled into the monochromator, which is controlled by a PC through an IEEE-488 interface. The output slit is set to a narrow width so that the monochromator is set to a high spectral resolution. The monochromator is programmed

to sweep across the visible wavelength range from 400 nm to 700 nm, and the spectrometer records the spectra and sends the data to the PC for analysis. Figure 5.6(b) shows the relationship between the output wavelength and the dial number of the monochromator. The measured data (red line) closely follows the best-fit line (black dashed line), confirming accurate and repeatable wavelength control. Figure 5.6(c) shows the normalised spectra of the illuminator (solid line) and the monochromator output (dashed line). A small shift in the peak wavelength is observed due to the spectrally varying reflectivity of the diffraction grating. The monochromator spectrum is used later for spectral calibration.

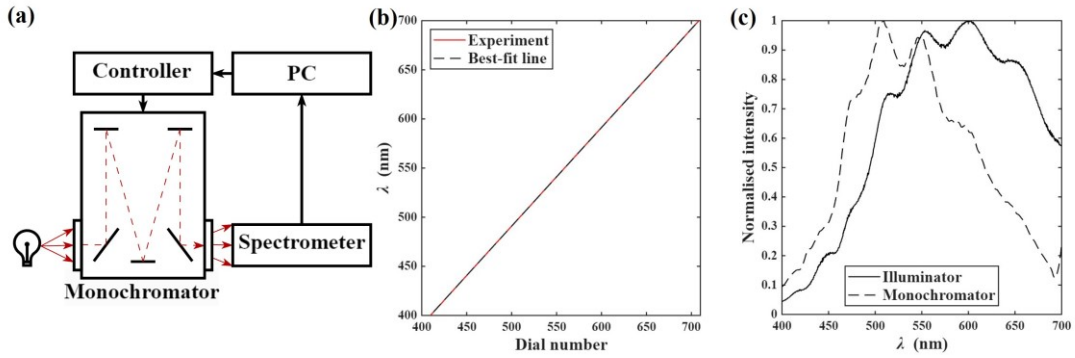


Fig. 5.6 (a) Experimental setup for measuring the monochromator output. (b) Measured wavelength as a function of the monochromator dial number. (c) Measured spectra of the illuminator and the monochromator output.

Direct Detection

Figure 5.7(a) shows the setup used to measure the response of the multi-channel PD (S9702, Hamamatsu) for mode-stripping detection. The PD has dimensions of 3 mm × 4 mm with a thickness of 1.3 mm. The PD has three effective segments of 0.3 mm^2, each with a different absorption layer, which allows simultaneous detection of red, green, and blue light. An objective lens (45×/0.65, Beck) is placed at the output of the monochromator to focus the light onto a selected PD segment. The PD output is connected to a transimpedance amplifier that converts the photocurrent into a voltage. The monochromator is controlled by a PC, and the amplifier output is sampled using a clocked DAC. Figure 5.7(b) shows the photo response of the three PD channels as a function of wavelength. Distinct peaks at 467 nm, 539 nm, and 616 nm show that the absorptive coatings on the PD can separate the incoming light into its RGB components.

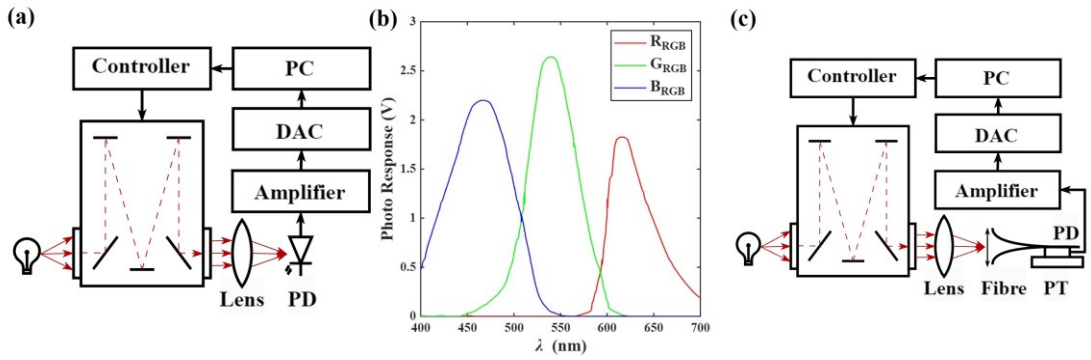


Fig. 5.7 (a) Setup for measuring RGB photodiode responses; (b) RGB photodiode responses after spectral calibration; and (c) Setup for measuring cladding mode response using RGB photodiodes.

Modulated Mode-Stripping Detection

Because the cladding-mode signal is sensitive to background light, scanned-fibre collection is used to modulate the PD response and hence allow phase-sensitive detection. Figure 5.7(c) shows this approach. A 5 cm fibre cantilever with a resonant frequency of 44 Hz is used. The fibre is mounted directly above the PD, and the PD is fixed to PT. Light from the monochromator is coupled into the fibre, which is driven at its resonant frequency to generate a modulated signal. The output is recorded using the clocked DAC and processed in MATLAB using a fast Fourier transform (FFT) to extract the signal at the resonance frequency. Figure 5.8 shows the spectral variation in the PD response across the visible wavelength range for different fibre configurations, as indicated by the insets. Brighter traces are obtained using PCFs, while dimmer traces correspond to SMFs. The SMF produces a higher response because its cladding area is larger than the PCF by 34%, improving the light-collection intensity.

Among the configurations tested, Figure 5.8(a) shows the most uniform spectral response, while Figure 5.8(b) and Figure 5.8(c) show enhanced green and blue responses, respectively. These configurations can be chosen based on the imaging application. If the spectral response is known, signal calibration can also be used to correct any imbalance. Figure 5.8(a) is suitable for full-colour imaging because the balanced responses of the three colour channels lead to improved colour reconstruction. In contrast, Figure 5.8(b) is more suitable for fluorescence imaging, where blue and green wavelengths are typically used for excitation and emission. In this case, blue light is used by the real-time controller and is mainly reflected rather than backscattered, so

only a low sensitivity is required. Green light, by contrast, is backscattered with lower intensity, and a stronger PD response improves fluorescence detection.

In conclusion, the cladding mode light is sufficiently strong and well spread to traverse the colour-selective absorption layers, allowing multi-channel PDs to act as a three-channel parallel spectrometer for cladding modes.

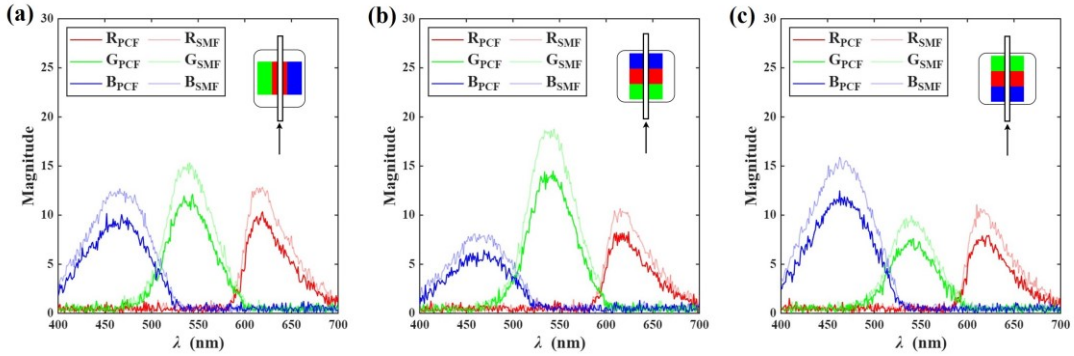


Fig. 5.8 Photodiode responses obtained in three configurations indicated by the insets after spectral calibration.

5.3 Scanning System

The scanning system follows the dual-NA confocal detection scheme [52] and is based on the setup shown in Figures 4.1-4.2, with modifications to enable multi-wavelength operation. These changes include adding optical components to support multi-wavelength illumination and applying coatings to the aperture to extract the required feedback signals. In addition, PCFs are used to guide the broadband light needed for multi-wavelength operation [121-122].

5.3.1 Scanner Setup

Figure 5.9 shows the multi-wavelength fibre scanner built using a dual-core PCF and mode-stripping detection. Light from red, green, and blue lasers is combined to generate broadband illumination for full-colour imaging, while the blue laser alone is used as a monochromatic source for fluorescence imaging. Figure 5.11(a) shows the spectra of the three individual laser sources together with the combined spectrum measured using a spectrometer. The red source is an SMF-pigtailed laser diode (Seven Stage Optics) emitting at 637 nm (red line). The green source is a diode-pumped solid-state (DPSS)

laser (DJ532-10, Thorlabs) pumped at 808 nm, with a front-window filter that transmits only the 531 nm output (green line). The blue source is an SMF-pigtailed laser diode (LP488-SF20G, Thorlabs) operating at 488 nm (blue line). The red and blue lasers are connected to a WDM (RGB46HF, Thorlabs) using mating sleeves (ADAFC2, Thorlabs). The free-space output of the DPSS laser is coupled into the green port of the WDM, which is mounted on a fibre adaptor plate (SM1FC, Thorlabs), using an objective lens (95×/1.3, Cooke). Each laser is driven by an independent driver (LD-S1, Seven Stage Optics; LDC2000, Thorlabs; LDC200C, Thorlabs) and modulated using a single arbitrary waveform generator (AWG; TG5011, Thurlby Thandar Instruments Ltd.) under PC control. The driver currents are adjusted to equalise the optical powers of the three sources. Figure 5.11(a) shows the resulting WDM output spectrum as a black dashed line, with peaks aligned to those of the individual lasers.

Light from the WDM is butt-coupled into one core of the dual-core PCF. Cladding modes are suppressed using a mode stripper made from a neutral density filter and index-matching oil (Series A, Cargille). The fibre cantilever is mounted on the PD using UV-curing epoxy. Figure 5.8(a) shows this PD configuration. A cantilever length of 3 cm is used, and Figure 5.5(c) shows its frequency response. The PD is fixed to a PT at 45°, which allows excitation in both directions and generates the Lissajous scan pattern. Optical feedback for the real-time controller is collected at the extremes of the fibre motion using an aperture coated with four inks (Textsurfer classic 364, Staedtler). To support both fluorescence and full-colour imaging, the system uses feedback from the blue channel. An achromatic doublet (AC050-008-A, Thorlabs) with a 400-700 nm anti-reflection coating is placed in front of the fibre to image the target and reduce focal-length variation across the visible range. Backscattered cladding-mode signals are detected by the corresponding PD segments and sent to the controller for processing.

The controller follows the design described in Chapter 3. As before, it consists of three parts: an analogue circuit (CKT), a 16-bit clocked DAC, and an un-clocked 12-bit DAC. The DACs provide low-frequency control voltages to the circuit, which drives the scanner using a dual-frequency signal generated by two phase-locked voltage-

controlled oscillators. The controller adjusts the drive in real time using optical feedback to produce a square FOV. The convergence speed of the control loops is mainly set by the cut-off frequencies of the low-pass filters in the loops, while stability is determined by the steady-state error, which depends on the loop gain. A PC connection allows the scan density to be adjusted programmatically. The scan trajectory is generated by the controller and recorded using a PicoScope. Backscattered signals from the three channels are extracted using the oscilloscope's internal level trigger and recorded using a second oscilloscope (DSO1024A, Keysight Technologies). The data are then transferred to the PC for image reconstruction.

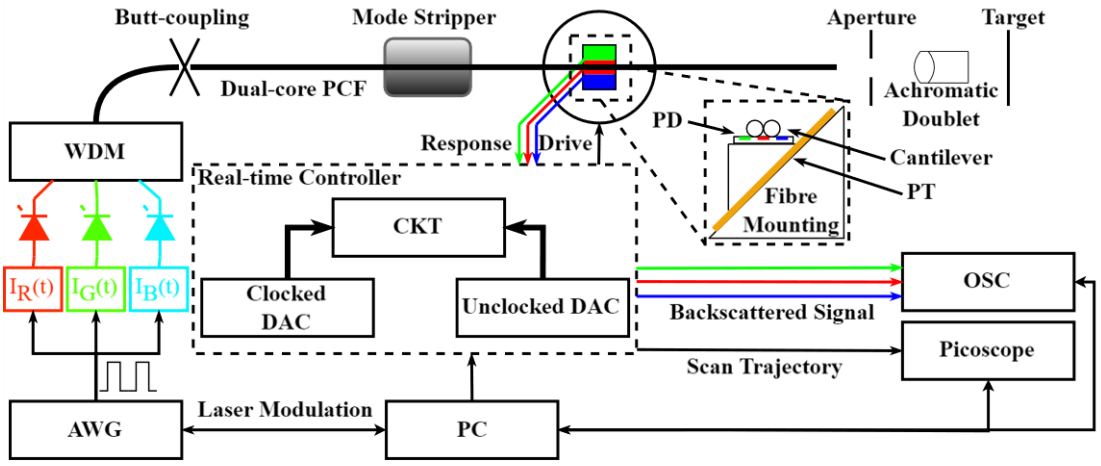


Fig. 5.9 Experimental setup for the multi-wavelength scanner with inset showing the fibre mounting.

Figure 5.10(a-c) shows the normalised reflectivity of the coatings measured by the red, green, and blue channels under illumination from the individual lasers. Figure 5.10(d-f) shows the corresponding results under broadband illumination. The coatings are chosen so that the reflectivities at the four edges fall within the required thresholds (dashed lines) for both monochromatic blue light and white-light operation. Under red and green illumination, the reflectivities are negligible, allowing the scanner to switch between fluorescence and full-colour imaging using only laser-diode programming. Among the three channels, only the blue channel meets the threshold requirements for all coatings, while the red and green channels do not. However, alternative approaches to signal coding such as surface-etched stainless steel might allow broadband operation.

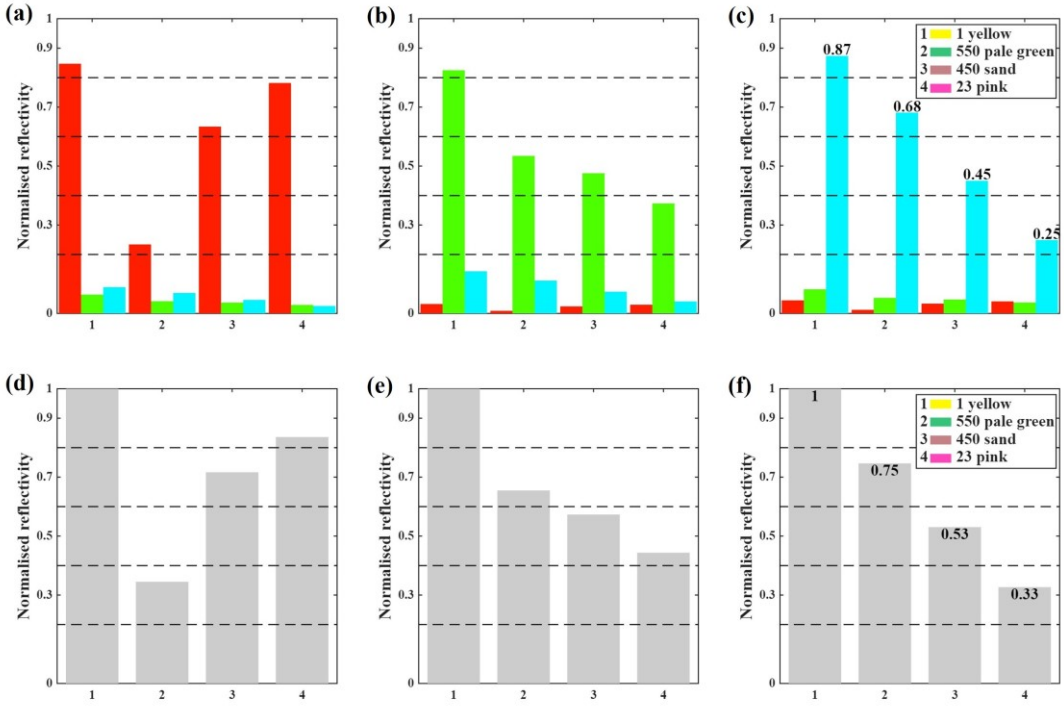


Fig. 5.10 Reflectivity of the colour-coded aperture under (a-c) RGB laser illumination and (d-f) multiplexed white light illumination, measured by the red, green, blue photodiodes.

To judge potential imaging performance, we now briefly revisit the question of scan-limited resolution. We define the central resolution using Δx and Δy of the central rhombus in the Lissajous pattern. Figure 5.11(b) shows this definition. If the FOV has a width h, the central resolution for $m = 2$ can be written as:

$$[\Delta x, \Delta y] = h\left[sin\left(\frac{1}{2n}\right), cos\left(\frac{n\pi}{2n+1}\right)\right] \tag{5.10}$$

Figure 5.11(b) shows the theoretical central resolution of the scanner for values of n from 31 to 101, calculated using Eqn. (5.10). The imaging lens is adjusted to give a large FOV (3 mm × 3 mm) and a small FOV (0.8 mm × 0.8 mm). These two FOVs are used later for different targets. For the large FOV, the central resolution decreases from 152 µm to 47 µm (red solid line) and from 75 µm to 23 µm (blue solid line) as n increases. For the small FOV, the central resolution decreases from 41 µm to 12 µm (red dashed line) and from 20 µm to 6 µm (blue dashed line). The Abbe resolution limit is given by Eqn. (1.29). Figure 5.11(b) shows this limit as a grey band for wavelengths between 400 nm and 700 nm for the PCF, ranging from 3.83 µm to 2.21 µm. This limit

lies below the theoretical central resolution for all values of n. Therefore, the current scanner does not operate at the diffraction limit.

Figure 5.11(c) shows the Lissajous scan pattern at $n = 91$, generated using white light obtained by setting the three lasers to equal power. A magnified view of the central region of the scan line confirms its symmetry, which demonstrates that the real-time controller effectively corrects phase errors. Figure 5.12 shows the corresponding Lissajous scan lines obtained using the individual monochromatic light sources. The Lissajous scans have the FOV of 5 mm × 5 mm and the fibre tip displacement is 1.4 mm, giving the magnification of 3.57.

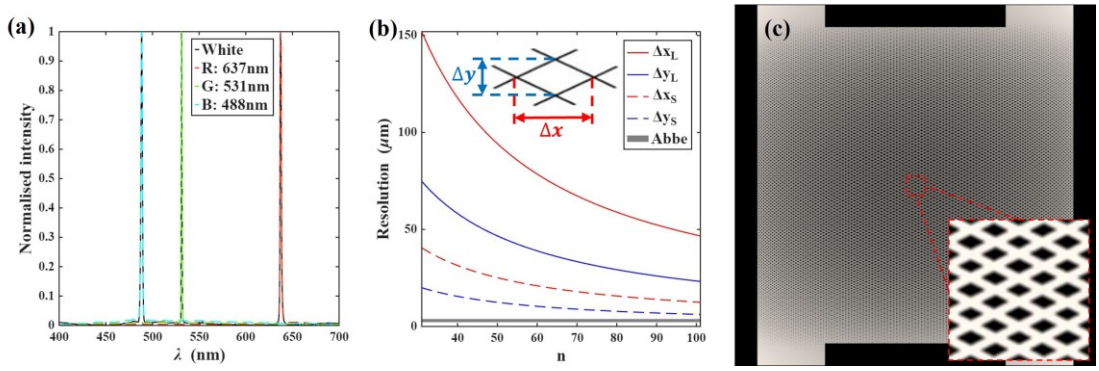


Fig. 5.11 (a) Spectra of the red, green, and blue laser sources, along with the multiplexed white-light spectrum (black dashed line); (b) central resolution of the scanner under large (3 mm × 3 mm) and small (0.8 mm×0.8 mm) fields-of-view (FOVs), compared with the Abbe resolution limit; and (c) experimental Lissajous scanning pattern from multiplexed white source with $n = 91$.

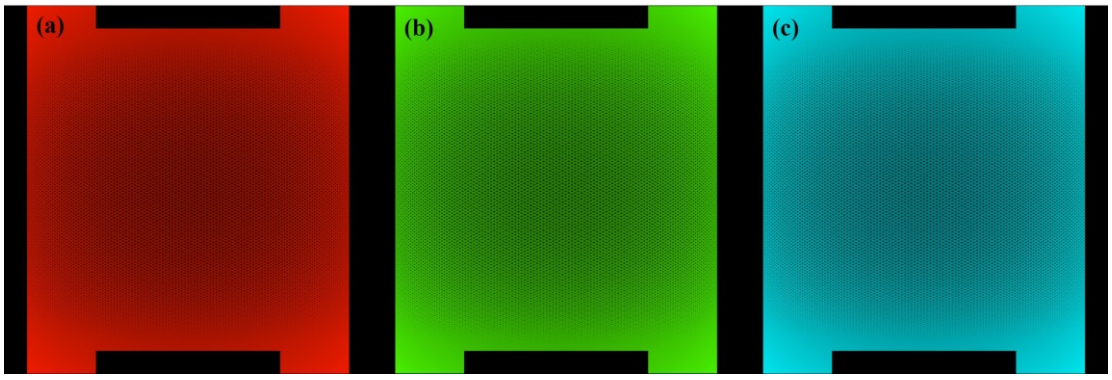


Fig. 5.12 Experimental Lissajous scan line from (a) red, (b) green and (c) blue sources with $n = 91$.

5.4 Multi-Wavelength Image Reconstruction

To demonstrate imaging performance, we now compare two applications, fluorescence imaging and full-colour imaging. Both are performed using exactly the same hardware

and control settings, confirming the flexibility and strong development potential of the colour scanning system.

5.4.1 Fluorescence Imaging

Fluorescence imaging was initially demonstrated using commercially available fluorescence test objects. For example, Figure 5.13(a-b) show photographs of a fluorescing disk (VRC3D05, Thorlabs) placed on white paper under daylight and under blue-light illumination. Under blue excitation, the disk appears red. Figure 5.13(c) shows the time variation of scattered signals obtained from the disk and the surrounding paper using a modulated blue laser. The blue PD signal decreases over the fluorescing disk (blue traces), while an additional modulated signal at the same frequency appears in the red channel (red traces), confirming the fluorescence response in the photographs.

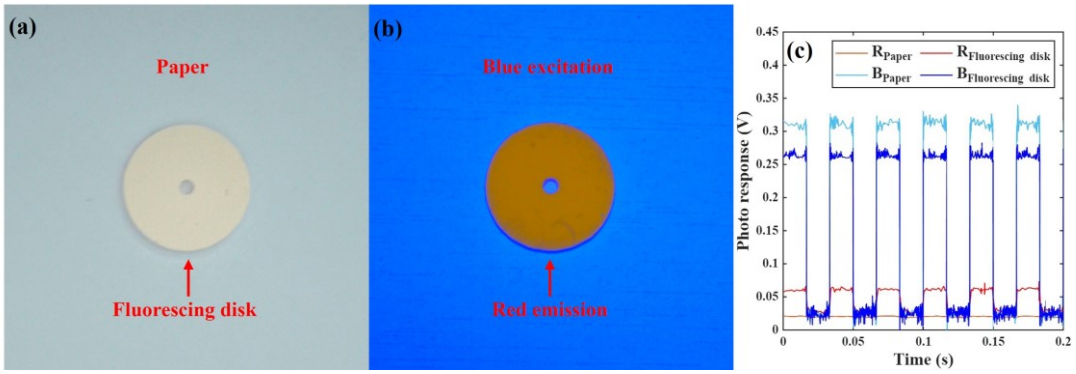


Fig. 5.13 (a) Conventional and (b) fluorescence images of a paper sheet under a fluorescent disk; and (c) photo responses at excitation (blue) and emission (red) wavelengths from the same sample.

Similarly, Figure 5.14(a) shows a reference image of a negative fluorescent USAF 1951 resolution target (57-792, Edmund Optics) taken using a conventional microscope. The white regions correspond to reflective chrome, while the grey regions correspond to fluorescent fused silica with a peak emission wavelength of 550 nm. The numbers at the top of each column indicate the group number, and the numbers along the sides indicate the element number. The resolution of the scanner is evaluated in terms of line pairs per millimetre. Figure 5.14(b-c) show reconstructed images obtained under blue excitation with detection from the green PD channel for $n = 41$ and $n = 91$, respectively. The corresponding frame rates, given by f_{l0}/n, are 3.9 FPS and 1.8 FPS. Figure 5.14(d) shows an enhanced-resolution image obtained by combining

backscattered signals from scans with n ranging from 41 to 91 in steps of 10. The optical aperture appears as black regions along all four edges in each reconstructed image. The reconstructed images show a zigzag artefact in the line pairs, which is characteristic of Lissajous scanning. Figure 5.11(b-c) show that the resolving power is higher for horizontal lines than for vertical lines, and this difference arises from the unequal scan frequencies along the two axes. In Figure 5.14(b), Group 5 Element 6 is resolved at $n = 41$, corresponding to a resolution of 8.8 μm. In Figure 5.14(c), Group 6 Element 6 is resolved at $n = 91$, corresponding to a resolution of 4.4 μm. Both resolutions are above the Abbe limit. Figure 5.14(d) shows that combining different scan patterns removes the Lissajous artefact. Lines at Group 7 Element 6 are now resolved, corresponding to a resolution of 2.2 μm, which lies below the Abbe limit.

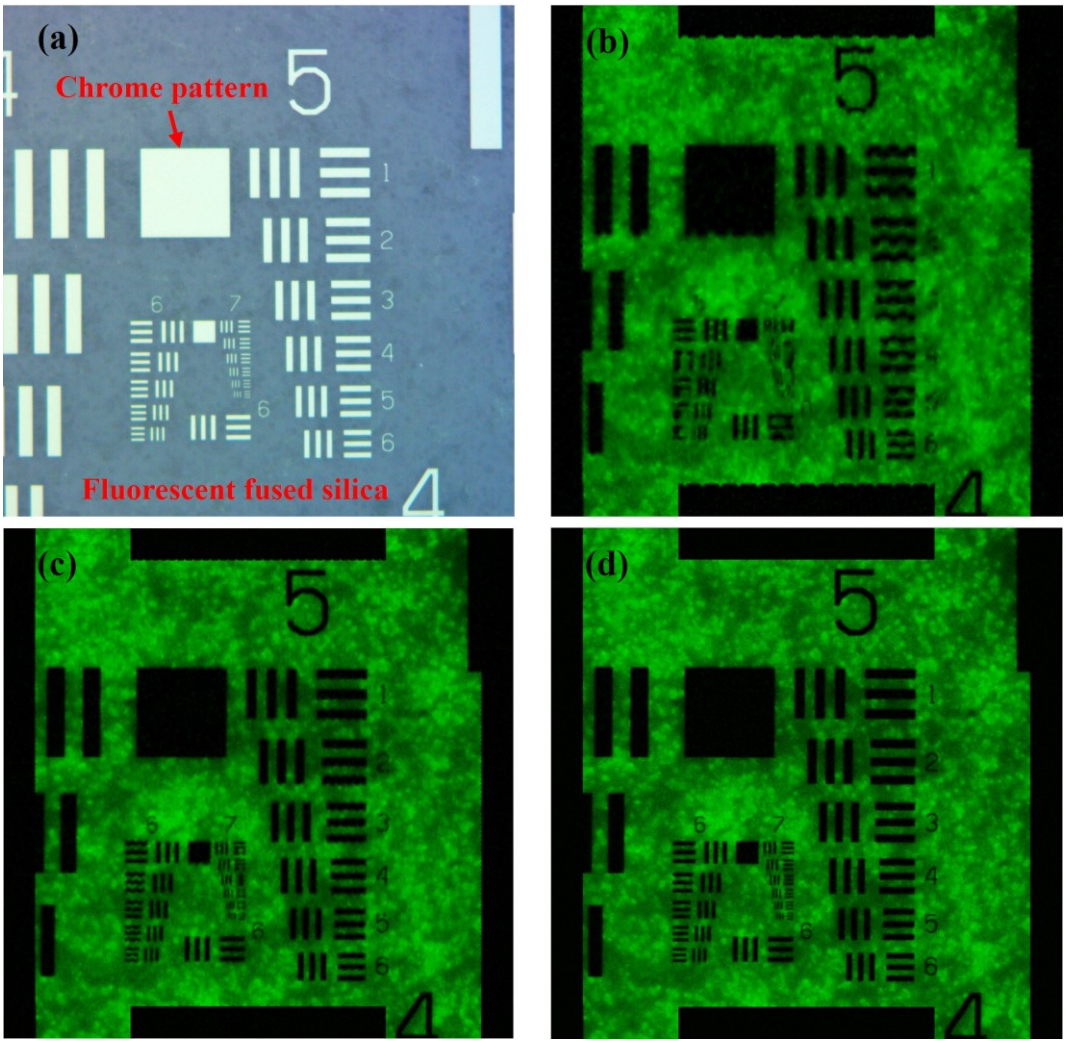


Fig. 5.14 (a) Original microscopic image; reconstructed images with (b) $n = 41$, (c) $n = 91$, and (d) enhanced resolution of a fluorescent USAF 1951 target.

Fluorescence imaging is a key tool in biomedical imaging and was also demonstrated using biological specimens. For example, Figure 5.15(a) shows a microscope image of a spinach leaf soaked in ethanol [136-138]. The ethanol extracts chlorophyll from the leaf, making it fluorescent under blue excitation. The leaf texture is visible, and air bubbles appear as bright circular features. Figure 5.15(b-d) shows reconstructed fluorescence images obtained under blue laser illumination for $n = 41$, $n = 91$, and the enhanced-resolution case, respectively. Under blue excitation, the leaf emits red fluorescence. Chlorophyll dissolved in ethanol accumulates along the grooves of the leaf texture, causing these regions to fluoresce, while the surrounding areas remain dark. The air bubbles remain clearly visible due to their reflective surfaces. Figure 5.15(b-c) show that the fluorescent grooves within the dashed white box become progressively sharper as n increases. Fine dust features become visible at $n = 91$ and are clearly resolved in the enhanced-resolution image.

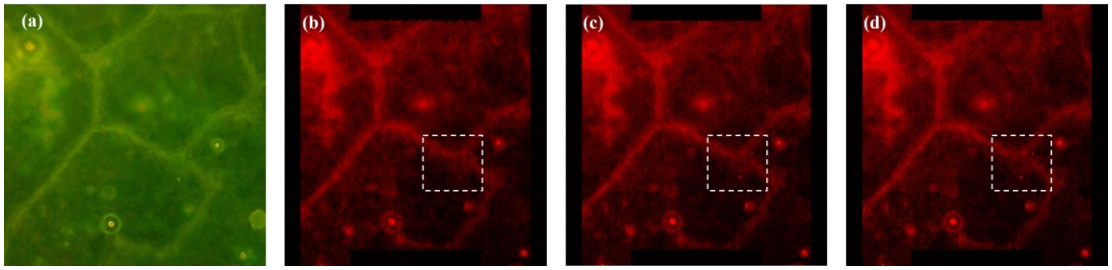


Fig. 5.15 (a) Original microscopic image; reconstructed images with (b) $n = 41$, (c) $n = 91$, and (d) enhanced resolution of a fluorescent spinach leaf soaked in ethanol.

5.4.2 Full-Colour Imaging

Full-colour imaging requires careful colour calibration. Figures 5.16-5.19 show the results of full-colour imaging using broadband illumination. Figure 5.16(a) shows the colour calibration process, which adjusts the reconstructed colours so that they match the true colours of a reference ColorChecker (MSCCMN-RET, X-Rite Inc.). Each colour patch of the ColorChecker is scanned, and the RGB outputs from the PD are used as the reconstructed RGB values (left column). The corresponding true RGB values from the ColorChecker specification are used as the reference colours (right

column). Calibration is performed by finding a transformation matrix C that maps the reconstructed RGB values to the true RGB values:

$$C = pinv(M) \times [R_t \quad G_t \quad B_t]^T \tag{5.11}$$

Here, M is a 10×1 matrix with linear terms (R, G, B), quadratic terms (R^2, G^2, B^2), cross terms (RG, RB, GB) and offset term of the reconstructed RGB values before calibration. R_t, G_t, B_t are the true RGB values, and $pinv$ is the Moore-Penrose pseudo-inverse [139-140], which provides the minimum-norm least squares solution. Eqn. (5.11) incorporates only four terms to prevent overfitting. Figure 5.16(a) shows that, after calibration, the reconstructed colours (middle column) closely match the true colours [141].

Colour imaging was initially carried out using a UK postage stamp, because of its high level of detail and colour contrast. Figure 5.16(b-c) show reconstructed images of the stamp under a large field of view, before and after calibration. Figure 5.16(c) shows a more vivid image, with the green colour cast removed and a colour balance that closely matches visual observation.

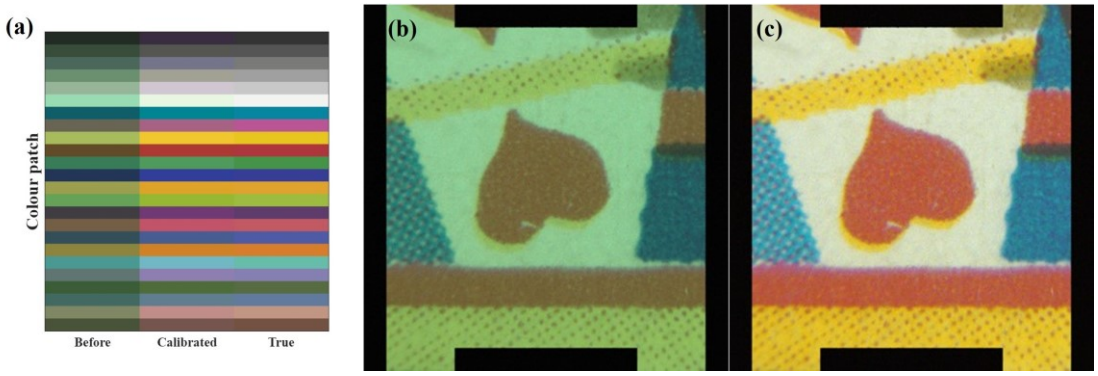


Fig. 5.16 (a) Scanned colour-patch images before and after colour calibration, shown alongside reference values from the ColorChecker; reconstructed full-colour image (b) before and (c) after colour calibration of a UK postage stamp.

Coloured biological specimens were also imaged. For example, Figure 5.17(a) shows the true-colour microscope image of a prepared slide (Set B, United Scope LLC) of a Zea grass stem cross-section. Figure 5.17(b) shows the reconstructed image after colour calibration at $n = 41$. At this scan density, many speckle artefacts are present due to the Delaunay triangulation applied to the sparse sampling pattern. The guard

cells can be identified, but the edges appear blurred. Figure 5.17(c) shows the reconstructed image at $n = 91$. The speckle density is reduced, and finer cellular features become visible. Figure 5.17(d) shows the enhanced-resolution image. Speckle artefacts are largely removed, and the edges and internal structures are consistent with the original microscope image. A slight yellow colour cast remains, which arises from residual calibration error in Eqn. (5.11).

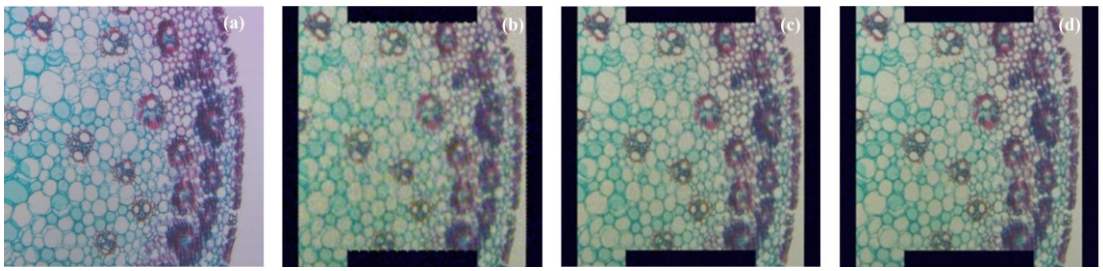


Fig. 5.17 (a) Original true colour image; reconstructed images with (b) $n = 41$, (c) $n = 91$, and (d) enhanced resolution after colour calibration, of a prepared slide of Zea grass stem section.

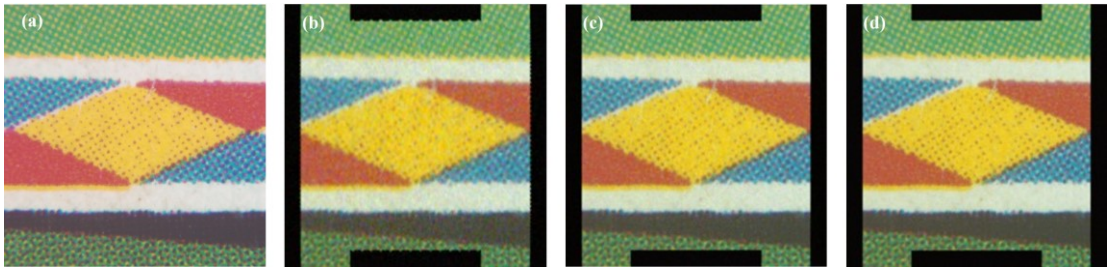


Fig. 5.18 (a) Original true colour image; reconstructed images with (b) $n = 41$, (c) $n = 91$, and (d) enhanced resolution after colour calibration, of a UK postage stamp.

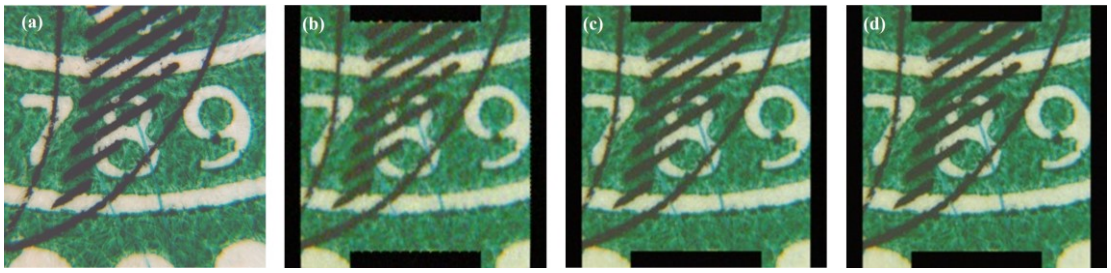


Fig. 5.19 (a) Original true colour image; reconstructed images with (b) $n = 41$, (c) $n = 91$, and (d) enhanced resolution after colour calibration, of a USD banknote.

Finally, Figures 5.18 and 5.19 show two additional reconstructed images, one of a different UK postage stamp and one of a USD banknote. Similar trends are observed: the resolution increases and the images become sharper as n increases, and the colour

fidelity improves after colour calibration. In each case, the enhanced-resolution reconstructions provide the highest level of detail.

5.5 Conclusion

We have presented a multi-wavelength confocal fibre scanner based on PCFs and RGB mode-stripping detectors. Source scanning is achieved using a dual-fibre cantilever mounted on a piezo transducer at 45°, enabling 2D motion under dual-frequency excitation. The cantilever is fabricated using a modified dip-coating technique suitable for holey fibres. The spectral response of mode-stripping detection using PCF and SMF claddings has been characterised in different configurations. Multiplexing of RGB laser sources was achieved using a WDM. While the current PD is limited to RGB channels, off-the-shelf detectors with increased channel numbers could provide improved spectral resolution. Optical feedback was realised via selective coating of a metal aperture, enabling real-time switching between imaging modes. Although demonstrated here with RGB lasers, this method is in principle extendable to other spectral bands. Compared with previously demonstrated colour scanners, high detection sensitivity, high resolution and high colour fidelity have all been achieved using an extremely simple optical architecture.

Chapter 6: Summary and Future Work

6.1 Summary

In this thesis, a programmable controller for a 2D Lissajous fibre scanner has been demonstrated. The source motion is generated using a fibre cantilever fabricated by dip-coating two fibres to form a composite section with non-degenerate mechanical properties. The low damping ratio allows the two orthogonal bending modes to be excited independently using a single PT. The optical system is an efficient dual NA confocal microscope, in which the fibre core is used for illumination and the cladding is used for detection. Because there is no direct electrical sensing of the fibre motion, optical feedback is provided by reflection from a shaped aperture. Amplitude-coded reflectivity and window detection allow timing signals to be separated from backscattered data while using a single PD. Although the feedback is intermittent, it enables continuous estimation and control of both frequency and phase.

The controller design combines analytical theory with numerical simulation in SIMULINK, and key parameters, including the stability limit and convergence rate, have been analysed. Excellent agreement is obtained between theory, simulation, and experiment. The controller is programmable and allows the selection of Lissajous trajectories with different scan densities. This flexibility is useful for applications that require rapid target acquisition followed by detailed inspection, and it could be further improved if a wider range of scan line densities is achieved. The same control principles are also applicable at slow video rates. While the current implementation uses discrete electronics, the control algorithms could be implemented on a DSP. The control approach may also be transferable to other Lissajous-based scanning systems.

A multi-wavelength fibre scanner based on PCFs and mode-stripping dual NA confocal detection has also been demonstrated. The fibre cantilever is fabricated using a modified dip-coating process suitable for holey fibres. The spectral response of mode-stripping detection for the cladding of both PCFs and SMFs has been characterised under different configurations. Multiplexing of RGB laser sources is achieved using a

WDM. Although the current PD is limited to three channels, COTS PDs with more channels could provide improved spectral resolution. In addition, optical coatings on standard photodiodes could be used to extract specific wavelength bands. The approach can be extended to HC-PBG fibres to allow higher optical powers, enabling applications such as image writing or phototherapy. Optical feedback is implemented using a selectively coated metal aperture, which allows real-time switching between fluorescence imaging and full-colour reflectance imaging. Although demonstrated using RGB excitation, the method can in principle be extended to other wavelength bands, including the mid-infrared band used for medical imaging.

6.2 Further Work

In addition to the work presented here, several directions for further development remain, including phase-shifted Lissajous scanning, broadband optical feedback, dispersion-free reflective scanning systems, and the use of HC-PBG fibres.

Phase-shifted Lissajous Scanning

The Lissajous curve is sensitive to the phase terms, which shift the trajectory horizontally and vertically away from the ideal scan pattern. However, if the phase is precisely controlled, which can be achieved using the real-time controller, the phase shift can be used to generate denser scan lines and therefore improve spatial resolution. When phase shifts are applied, the Lissajous motion can be written as:

$$\begin{bmatrix} x \\ y \end{bmatrix} = \begin{bmatrix} sin(2\pi rft + \phi_x) \\ cos(2\pi ft + \phi_y) \end{bmatrix} \tag{6.1}$$

For the phase-shifted motion to produce the same trajectory as the ideal case, the curve must pass through at least one point on the original path. In addition, the direction of the two-dimensional motion must remain the same so that the curves overlap rather than intersect. For simplicity, the point [0,1] at time $t_0 = 0$ is chosen, and Eqn. (6.1) is required to pass through this point at $t_1 = t_0 + \Delta t$. Because the Lissajous curve is symmetric, the scan line remains unchanged if the trajectory passes through the points [0, ±1]. This gives:

$$\begin{bmatrix} 0 \\ \pm 1 \end{bmatrix} = \begin{bmatrix} \sin(2\pi r f t_1 + \phi_x) \\ \cos(2\pi f t_1 + \phi_y) \end{bmatrix} = \begin{bmatrix} \sin(2\pi r f t_0 + 2\pi r f \Delta t + \phi_x) \\ \cos(2\pi f t_0 + 2\pi f \Delta t + \phi_y) \end{bmatrix} \tag{6.2}$$

For Eqn. (6.2) to hold, the arguments of the sine and cosine functions must satisfy:

$$2\pi r f \Delta t + \phi_x = a\pi \tag{6.3}$$

$$2\pi f \Delta t + \phi_y = b\pi \tag{6.4}$$

where a and b are integers. Solving Eqns. (6.3-6.4), and expanding, gives:

$$(mn+1)\phi_y - n\phi_x = \pi[b(mn+1) - an] \tag{6.5}$$

Let $c = b(mn+1) - an$. Since m, n, a, b are integers, c is also an integer. If $b = n + c$ and $a = bm + 1$, Eqn. (6.5) becomes:

$$(mn+1)\phi_y - n\phi_x = c\pi \tag{6.6}$$

In summary, if the phase components satisfy Eqn. (6.6), the Lissajous trajectory recovers the same shape after one complete cycle. In the current fibre-scanner implementation, the horizontal phase component is assumed to be zero, so only the vertical phase is considered. Under this assumption, Eqn. (6.6) reduces to:

$$\phi_y = \frac{c\pi}{mn+1} \tag{6.7}$$

The derivatives of the ideal trajectory and the phase-shifted trajectory are identical when the condition in Eqn. (6.7) is satisfied, confirming that the motion direction is the same. The sampling at the Padua points of the ideal Lissajous curve can be written as:

$$\begin{bmatrix} x_s \\ y_s \end{bmatrix} = \left\{ \begin{matrix} sin\left[2\pi r f\left(0 : \frac{1}{4f(mn+1)} : \frac{n}{f}\right)\right] \\ cos\left[2\pi f\left(0 : \frac{1}{4f(mn+1)} : \frac{n}{f}\right)\right] \end{matrix} \right\} = \begin{bmatrix} sin\left(0 : \frac{\pi}{2n} : 2(mn+1)\pi\right) \\ cos\left(0 : \frac{\pi}{2(mn+1)} : 2n\pi\right) \end{bmatrix} \tag{6.8}$$

Since Eqn. (6.8) is periodic, the non-repeating sampling coordinates are:

$$\begin{bmatrix} x_s \\ y_s \end{bmatrix} = \left\{ \begin{matrix} \sin\left[-\frac{\pi}{2} : \frac{\pi}{2n} : \frac{\pi}{2}\right] \\ \cos\left[0 : \frac{\pi}{2(mn+1)} : \pi\right] \end{matrix} \right\} \tag{6.9}$$

The number of sampling groups in the x- and y-directions is therefore:

$$\begin{bmatrix} G_x \\ G_y \end{bmatrix} = \begin{Bmatrix} 2n+1 \\ 2(mn+1)+1 \end{Bmatrix} \tag{6.10}$$

This means that the sampling points form $2n+1$ vertical lines and $2mn+3$ horizontal lines in the original Lissajous pattern. Figure 6.1(a-d) show this sampling structure. From Eqn. (6.7), a phase shift larger than $\pi/(mn+1)$ is redundant. The phase range is therefore limited to $[-\pi/[2(mn+1)], \pi/[2(mn+1)]]$. Let N (an odd integer) denote the number of phase-shift steps. Figure 6.1(a) and (d) show that no phase shift is applied, and the sampling pattern is identical to the original case when $N = 1$. When $N > 1$, the phase-shift values are given by:

$$\phi_{ys} = \left[-\frac{\pi}{2(mn+1)} : \frac{\pi}{(N-1)(mn+1)} : \frac{\pi}{2(mn+1)}\right] \tag{6.11}$$

The resulting family of phase-shifted Lissajous curves can be written as:

$$\begin{bmatrix} x \\ y \end{bmatrix} = \begin{Bmatrix} \sin[2\pi r f t] \\ \cos\left[2\pi f t + \left(-\frac{\pi}{2(mn+1)} : \frac{\pi}{(N-1)(mn+1)} : \frac{\pi}{2(mn+1)}\right)\right] \end{Bmatrix} \tag{6.12}$$

The phase shifts insert $N-2$ additional scan lines into each gap, dividing the original gaps evenly into $N-1$ segments. This generates additional Padua points, and the sampling rate must be increased by a factor of $N-1$. The new sampling times are:

$$t_s = 0 : \frac{1}{4f(N-1)(mn+1)} : \frac{n}{f} \tag{6.13}$$

After removing overlapping points, the updated sampling coordinates are:

$$\begin{bmatrix} x_s \\ y_s \end{bmatrix} = \begin{Bmatrix} \sin\left[-\frac{\pi}{2} : \frac{\pi}{2n(N-1)} : \frac{\pi}{2}\right] \\ \cos\left[0 : \frac{\pi}{2(mn+1)(N-1)} : \pi\right] \end{Bmatrix} \tag{6.14}$$

The corresponding number of sampling groups is:

$$\begin{bmatrix} G_x \\ G_y \end{bmatrix} = \begin{Bmatrix} 2n(N-1)+1 \\ 2(N-1)(mn+1)+1 \end{Bmatrix} \tag{6.15}$$

Therefore, for an N-step phase-shifted Lissajous scan, the sampling points form $2n(N-1)+1$ vertical lines and $2(N-1)(mn+1)+1$ horizontal lines. Figure 6.1(b-c) and (e-f) show the resulting sampling patterns.

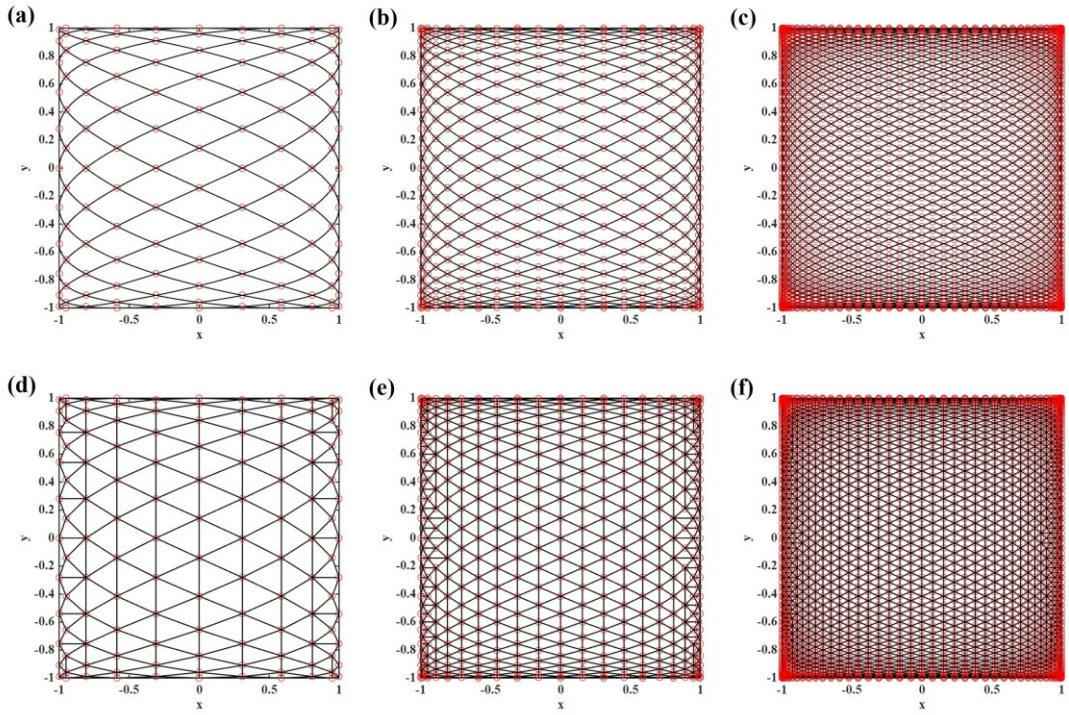


Fig. 6.1 (a-c) Lissajous curve with sampling at Padua points and (d-f) Delaunay triangulation with the phase-shift steps N from 1 to 5 with $n = 5$

In conclusion, phase-shifted Lissajous curves can be generated by introducing appropriate phase components. The additional Padua points lie on straight lines and therefore do not affect the Delaunay triangulation. This method allows the effective resolution to exceed the limit set by n, and it may approach the Abbe resolution limit. However, adding phase shifts requires the controller to settle to a new steady state, which slows the system response and reduces the achievable frame rate. A possible solution is to implement the controller on a DSP and use digital filtering techniques to speed up the transient response.

Broadband Optical Feedback

The aperture has been tailored and coated with different materials to distinguish the optical feedback associated with each mode. However, because the feedback is amplitude-modulated, the intensity of the returned signals must be calibrated using coatings that are appropriate for each illumination wavelength. In this thesis, when the illumination was changed from a monochromatic red laser to broadband white light, different sets of coatings were used to compensate for wavelength-dependent reflectivity. A useful improvement to the aperture design would be to modulate the

optical feedback to allow broadband operation. The possible approach is to etch periodic slots with different separation gaps and widths into the reflector surface. Figure 6.2(a) shows an example of such a grooved reflector. These structures would modify the pulse width, frequency, and interval of the feedback pulses, modulating the signal in the frequency domain. This would allow optical feedback from different reflectors to be distinguished using these properties rather than relying on pulse amplitude.

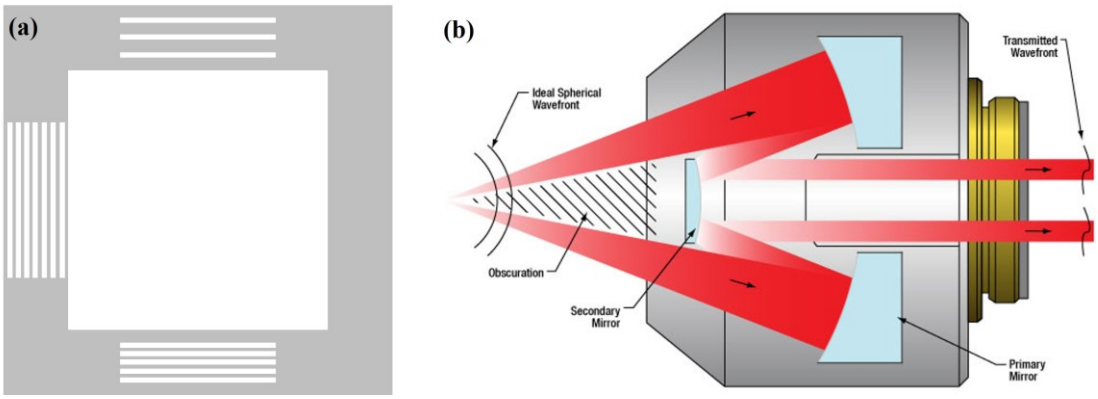


Fig. 6.2 (a) A proposed design for the broadband aperture and (b) the configuration of a reflective microscopic objective (Thorlabs).

Reflective Dispersion-Free Scanning Systems

In Chapter 5, the multi-wavelength scanning system uses an achromatic doublet to reduce focal shifts caused by chromatic dispersion. In refractive lenses, the effective refractive index depends on wavelength, so light at different wavelengths is focused at different axial positions. Although achromatic doublets and triplets reduce this effect, refractive systems always retain some residual dispersion. A possible solution is to replace refractive optics with reflective elements, which are inherently free from dispersion. Figure 6.2(b) shows the design of a reflective microscopic objective (Thorlabs). In this system, light from the sample is reflected by a primary mirror and then by a secondary mirror before being relayed to the detector. Such a configuration could be used in the multi-wavelength scanning system to eliminate chromatic dispersion. The main limitation of current COTS reflective objectives is their physical size, as they are typically designed for telescopes [142] or multi-pass spectroscopic absorption cells [143]. A possible improvement is to coat small lenses with reflective layers to create a compact, dispersion-free imaging system.

HC-PBG Fibres

The dip-coating method developed in this thesis has been adapted for fibres with air holes, which also makes it suitable for use with HC-PBG fibres. Figure 6.3 shows that the resonant frequency ratio decreases below 2 when a polymer fillet is added. This result indicates that HC-PBG fibres can be integrated into the current scanning system with only minor adjustments. Using HC-PBG fibres would further extend the capabilities of the system, enabling applications such as image writing or other biomedical functions that require high-power light beams.

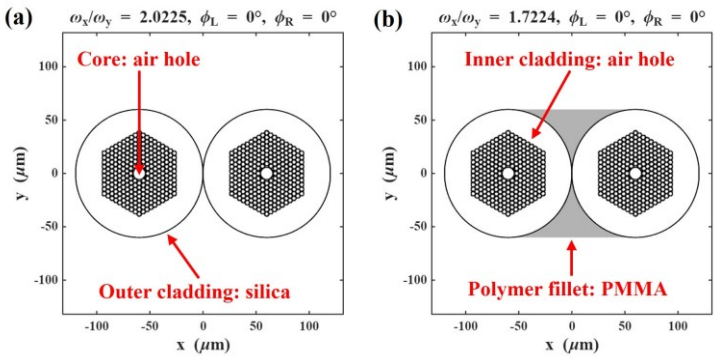


Fig. 6.3 Cross-sections of dual-core hollow core photonic bandgap fibres (a) without and (b) with polymer fillet.

References

[1] L. Giniunas, R. Juskaitis, S. V. Shatalin, “Scanning fibre-optic microscope,” Electron. Lett. 27(9), 724-726 (1991)

[2] S. Kimura, T. Wilson, “Confocal scanning optical microscope using single-mode fiber for signal detection,” Appl. Opt. 30, 2143-2150 (1991)

[3] D. L. Dickensheets, G. S. Kino, “Silicon-micromachined scanning confocal optical microscope,” J. Microelectromech. Syst. vol. 7, no. 1, pp. 38-47 (1998)

[4] H. Miyajima, N. Asaoka, T. Isokawa, et al., "A MEMS electromagnetic optical scanner for a commercial confocal laser scanning microscope," J. Microelectromech. Syst. vol. 12, no. 3, pp. 243-251 (2003)

[5] L. Giniūnas, R. Juškaitis, S. V. Shatalin, "Endoscope with optical sectioning capability," Appl. Opt. 32, 2888-2890 (1993)

[6] E. J. Seibel, Q. Y. J. Smithwick, C. M. Brown, et al., "Single-fiber flexible endoscope: general design for small size, high resolution, and wide field of view," Proc. SPIE 4158, 29-39 (2001)

[7] B. A. Flusberg, J. C. Jung, E. D. Cocker, et al., "In vivo brain imaging using a portable 3.9gram two-photon fluorescence microendoscope," Opt. Lett. 30, 2272-2274 (2005)

[8] A. Wartak, A. K. Kelada, P. A. L. Alarcon, et al., "Dual-modality optical coherence tomography and fluorescence tethered capsule endomicroscopy," Biomed. Opt. Express 12, 4308-4323 (2021)

[9] Y. H. Seo, H. C. Park, K. H. Jeong, "Electrothermal MEMS fiber scanner with Lissajous patterns for endomicroscopic applications," 2016 IEEE 29th International Conference on Micro Electro Mechanical Systems (MEMS), Shanghai, China, Jan. 24-28, pp. 367-370 (2016)

[10] M. J. Marques, M. R. Hughes, A. F. Uceda, et al., "Endoscopic en-face optical coherence tomography and fluorescence imaging using correlation-based probe tracking," Biomed. Opt. Express 13, 761-776 (2022)

[11] S. Moon, S. W. Lee, M. Rubinstein, et al., "Semi-resonant operation of a fiber-cantilever piezotube scanner for stable optical coherence tomography endoscope imaging," Opt. Express 18, 21183-21197 (2010)

[12] M. H. Kiang, O. Solgaard, R. S. Muller, et al., "Micromachined polysilicon microscanners for barcode readers," IEEE Photonics Technol. Lett. vol. 8, no. 12, pp. 1707-1709 (1996)

[13] M. Ikeda, H. Goto, H. Totani, et al., "Two-dimensional miniature optical-scanning sensor with silicon micromachined scanning mirror," Proc. SPIE 3008, 111-122 (1997)

[14] J. H. Leach, S. R. Chinn, L. Goldberg, et al., "Monostatic all-fiber rangefinder system," Appl. Opt. 54, 7687-7692 (2015)

[15] H. Urey, “Torsional MEMS scanner design for high-resolution display systems,” Proc. SPIE 4773, 27-37 (2002)

[16] R. C. Bryant, E. J. Seibel, C. M. Lee, et al., “Low-cost wearable low-vision aid using a handmade retinal light-scanning microdisplay,” J. Soc. Inf. Disp. 12: 397-404 (2004)
[17] W. C. Wang, C. L. Tsui, "Two-dimensional mechanically resonating fiber optic scanning display system," Opt. Eng. 49(9), 097401 (2010)
[18] R. Khayatzadeh, F. Civitci, O. Ferhanoglu, et al., "Scanning fiber microdisplay: design, implementation, and comparison to MEMS mirror-based scanning displays," Opt. Express 26, 5576-5590 (2018)
[19] T. Kuno, T. Nakamura, T. Matsuda, et al., “Fiber-scanning based ultra-compact near-eye display with a narrow-beam waveguide,” Opt. Rev. 28, 716-722 (2021)
[20] K. Petroz, E. Ollier, H. Grateau, et al., "A fully integrated micro-opto-mechanical steering device," Proc. MEMS 98. IEEE Eleventh Annual International Workshop on Micro Electro Mechanical Systems, Heidelberg, Germany, Jan. 25-29. pp. 105-109 (1998)
[21] K. Petroz, H. Grateau, E. Ollier, et al., “Integrated micro-optomechanical laser beam deflector,” Elect. Lett. 34, 881-882 (1998)
[22] H. Toshiyoshi, G. D. J. Su, J. LaCosse, et al., "A surface micromachined optical scanner array using photoresist lenses fabricated by a thermal reflow process," J. Lightwave Technol. 21, 1700-1708 (2003)
[23] G. Zhou, F. S. Chau, "Micromachined vibratory diffraction grating scanner for multiwavelength collinear laser scanning," J. Microelectromech. Syst. vol. 15, no. 6, pp. 1777-1788 (2006)
[24] K. E. Petersen, “Silicon torsional scanning mirror,” IBM J. Res. Develop. 24(5), 631–637 (1980)
[25] R. R. A. Syms, “Operation of a surface-tension self-assembled 3D micro-optomechanical torsion mirror scanner,” Elect. Lett. 35, 1157-1158 (1999)
[26] K. Petroz, E. Ollier, H. Grateau, et al., “Integrated silica micro-opto-electromechanical steering device for laser beam scanning,” Sens. Actuators A 73. 1-2: 117-121 (1999)
[27] E. Ollier, "Optical MEMS devices based on moving waveguides," IEEE J. Sel. Top. Quantum Electron. vol. 8, no. 1, pp. 155-162 (2002)
[28] Y. Wu, Y. Leng, J. Xi, et al., "Scanning all-fiber-optic endomicroscopy system for 3D nonlinear optical imaging of biological tissues," Opt. Express 17, 7907-7915 (2009)
[29] C. M. Lee, C. J. Engelbrecht, T. D. Soper, et al., “Scanning fiber endoscopy with highly flexible, 1 mm catheterscopes for wide-field, full-color imaging,” J. Biophoton. 3, 385-407 (2010)
[30] M. Kaur, P. M. Lane, C. Menon, “Scanning and actuation techniques for cantilever-based fiber optic endoscopic scanners: a review,” Sensors 21(1), 251 (2021)
[31] Y. S. Leong, M. H. H. Mokhtar, M. S. D. Zan, et al., "Optical-mechanical configuration of imaging operation for endoscopic scanner: a review," IEEE Access vol. 9, pp. 132705-132722 (2021)
[32] W. Thomson, “Theory of vibration with applications,” 4th edn., Chapman and Hall, London (2018)

[33] R. R. A. Syms, "Long-travel electrothermally driven resonant cantilever microactuators," J. Micromech. Microeng. 12, 211-218 (2002)
[34] P. M. Hagelin, O. Solgaard, "Optical raster-scanning displays based on surface-micromachined polysilicon mirrors," IEEE J. Sel. Top. Quantum Electron. vol. 5, no. 1, pp. 67-74 (1999)
[35] D. R. Rivera, C. M. Brown, D. G. Ouzounov, et al., “Compact and flexible raster scanning multiphoton endoscope capable of imaging unstained tissue,” Proc. Natl. Acad. Sci. U.S.A. 108(43), 17598-17603 (2011)
[36] H. Mansoor, H. Zeng, I. T. Tai, et al., "A handheld electromagnetically actuated fiber optic raster scanner for reflectance confocal imaging of biological tissues," IEEE Trans. Biomed. Eng. vol. 60, no. 5, pp. 1431-1438 (2013)
[37] D. Do, H. Yoo, D. G. Gweon, "Fiber-optic raster scanning two-photon endomicroscope using a tubular piezoelectric actuator," J. Biomed. Opt. 19(6), 066010-1-6 (2014)
[38] Y. Wang, Z. Li, X. Liang, et al., "Four-plate piezoelectric actuator driving a large-diameter special optical fiber for nonlinear optical microendoscopy," Opt. Express 24, 19949-19960 (2016)
[39] F. Akhoundi, Y. Qin, N. Peyghambarian, et al., "Compact fiber-based multi-photon endoscope working at 1700 nm," Biomed. Opt. Express 9, 2326-2335 (2018)
[40] C. Wang, H. Liu, J. Ma, et al., "Spiral scanning fiber-optic two-photon endomicroscopy with a double-cladding antiresonant fiber," Opt. Express 29, 43124-43135 (2021)
[41] H. Guan, W. Liang, A. Li, et al., "Multicolor fiber-optic two-photon endomicroscopy for brain imaging," Opt. Lett. 46, 1093-1096 (2021)
[42] H. C. Park, Y. H. Seo, K. H. Jeong, "Lissajous fiber scanning for forward viewing optical endomicroscopy using asymmetric stiffness modulation," Opt. Express 22, 5818-5825 (2014)
[43] L. He, X. Li, J. Yang, et al., "Super-simplified fiber scanner for cellular-resolution endoscopic imaging," Photon. Res. 11, 2020-2032 (2023)
[44] J. Dean, “XXXIV. Investigation of the apparent motion of the earth viewed from the moon, arising from the moon’s librations,” Mem. Am. Acad. Arts Sci. 3(2), 241 (1815)
[45] N. Bowditch, “On the motion of pendulum suspended from two points,” Mem. Am. Acad. Arts Sci. 3, 413-436 (1815)
[46] J. A. Lissajous, “Mémoire sur l’étude optique des mouvements vibratoires,” Ann. de Chimie et de Physique, 3rd series., 147–231 (1857)
[47] J. Lovering, “Anticipation of the Lissajous Curves,” Proc. of the Am. Acad. Arts Sci. 16, 292-298 (1880)
[48] T. Tuma, J. Lygeros, V Kartik, et al., “High-speed multiresolution scanning probe microscopy based on Lissajous scan trajectories,” Nanotechnol. 23, 185501 (2012)
[49] T. Tuma, J. Lygeros, A. Sebastian, et al., "Optimal scan trajectories for high-speed scanning probe microscopy," 2012 American Control Conference (ACC), Montreal, QC, Canada, 27-29 June, pp. 3791-3796 (2012)

[50] C. Kaethner, W. Erb, M. Ahlborg, et al., "Non-equispaced system matrix acquisition for magnetic particle imaging based on Lissajous node points," IEEE Trans. Med. Imaging vol. 35, no. 11, pp. 2476-2485 (2016)
[51] S. D. Marchi, W. Erb, F. Marchetti, "Lissajous sampling and spectral filtering in MPI applications: the reconstruction algorithm for reducing the Gibbs phenomenon," 2017 International Conference on Sampling Theory and Applications (SampTA), Tallinn, Estonia, 03-07 July, pp. 580-584 (2017)
[52] D. A. Roberts, R. R. A. Syms, A. S. Holmes, et al., "Dual numerical aperture confocal operation of a moving fibre bar-code reader," Electron. Lett. 35(19), 1656-1658 (1999)
[53] E. Abbe, "Beiträge zur Theorie des Mikroskops und der mikroskopischen Wahrnehmung," Archiv f. Mikrosk. Anatomie 9, 413-468 (1873)
[54] S. Turtaev, I. T. Leite, T. A. Boussac, et al., "High-fidelity multimode fibre-based endoscopy for deep brain in vivo imaging," Light Sci. Appl. 7, 92 (2018)
[55] M. Gu, C. J. R. Sheppard, X. Gan, "Image formation in a fiber-optical confocal scanning microscope," J. Opt. Soc. Am. A 8, 1755-1761 (1991)
[56] M. J. Li, X. Chen, K. Li, et al., "Optical fiber for 1310 nm single-mode and 850 nm few-mode transmission," Proc. SPIE 10945, Broadband Access Communication Technologies XIII, 1094503 (2019)
[57] S. Rashleigh, M. Marrone, "Polarization holding in elliptical-core birefringent fibers," IEEE J. Quantum Electron. vol. 18, no. 10, pp. 1515-1523 (1982)
[58] Z. Wang, J. Ju, W. Jin, "Properties of elliptical-core two-mode fiber," Opt. Express 13, 4350-4357 (2005)
[59] V. Ramaswamy, R. H. Stolen, M. D. Divino, et al., "Birefringence in elliptically clad borosilicate single-mode fibers," Appl. Opt. 18, 4080-4084 (1979)
[60] H. Li, X. Li, J. Wang, et al., "Ultra-high birefringence elliptical cladding polarization-maintaining fiber with superimposed geometric birefringence," Optik 247, 167854 (2021)
[61] M. Varnham, D. Payne, A. Barlow, et al., "Analytic solution for the birefringence produced by thermal stress in polarization-maintaining optical fibers," J. Lightwave Technol. vol. 1, no. 2, pp. 332-339 (1983)
[62] Y. Yang, Q. Mo, S. Fu, et al., "Panda-type elliptical core few-mode fiber," APL Photonics 4(2): 022901 (2019)
[63] R. Khayatzadeh, O. Ferhanoğlu, F. Çivitci, "Unwarped Lissajous scanning with polarization-maintaining fibers," IEEE Photonics Technol. Lett. vol. 29, no. 19, pp. 1623-1626 (2017)
[64] A. Kumar, V. Gupta, K. Thyagarajan, "Geometrical birefringence of polished and D-shaped fibres," Opt. Comm. 61, 195-198 (1987)
[65] D. A. Roberts, R. R. A. Syms, "1D and 2D laser line scan generation using a fiber optic resonant scanner," Proc. SPIE 4075, 62-73 (2000)
[66] T. Wu, Z. Ding, K. Wang, et al., "Two-dimensional scanning realized by an asymmetry fiber cantilever driven by single piezo bender actuator for optical coherence tomography," Opt. Express 17, 13819-13829 (2009)

[67] D. Y. Kim, K. Hwang, J. Ahn, et al., “Lissajous scanning two-photon endomicroscope for in vivo tissue imaging,” Sci. Rep. 9, 3560 (2019)
[68] J. Im, E. Jang, C. Song, "Analytical modeling and implementation of an imaging cantilever with a thermoplastic stiffener," IEEE/ASME Trans. Mechatron. vol. 29, no. 6, pp. 4320-4329 (2024)
[69] M. H. H. Mokhtar, R. R. A. Syms, "Tailored fibre waveguides for precise two-axis Lissajous scanning," Opt. Express 23, 20804-20811 (2015)
[70] Y. S. Leong, M. H. H. Mokhtar, A. A. Zukhri, et al., “Frequency-phase shift correction in interlaced Lissajous trajectories for precise imaging in endoscopic scanning microscopy,” Opt. Lasers Eng. 158, 107177 (2022)
[71] Q. Y. J. Smithwick, E. J. Seibel, P. G. Reinhall, et al., “Control aspects of the single-fiber scanning endoscope,” Proc. SPIE 4253, 176-188 (2001)
[72] Q. Y. J. Smithwick, J. Vagners, P. G. Reinhall, et al., “Modeling and control of the resonant fiber scanner for laser scanning display or acquisition,” SID Symposium Digest of Technical Papers, 34: 1455-1457 (2003)
[73] Q. Y. J. Smithwick, J. Vagners, R. S. Johnston, et al., “A hybrid nonlinear adaptive tracking controller for a resonating fiber microscanner,” J. Dyn. Sys., Meas., Control. 132(1): 011001 (2009)
[74] T. Wu, L. Zhang, J. Wang, et al., "Miniaturized precalibration-based Lissajous scanning fiber probe for high speed endoscopic optical coherence tomography," Opt. Lett. 45, 2470-2473 (2020)
[75] R. E. Kalman, “Lectures on controllability and observability,” Centro Internazionale Matematico Estivo (1968)
[76] R. Hermann, A. Krener, "Nonlinear controllability and observability," IEEE Trans. Autom. Control vol. 22, no. 5, pp. 728-740 (1977)
[77] B. H. W. Hendriks, W. C. J. Bierhoff, J. J. L. Horikx, et al., "High-resolution resonant and nonresonant fiber-scanning confocal microscope," J. Biomed. Opt. 16(2), 026007 (2011)
[78] I. L. Yeoh, P. G. Reinhall, M. C. Berg, et al., “Electromechanical modeling and adaptive feedforward control of a self-sensing scanning fiber endoscope,” J. Dyn. Sys. Meas. Control. 138(10), 101006 (2016)
[79] C. N. Coleal, W. A. Hudson, J. W. Wilson, "Sparse Lissajous scanning reflectance confocal microscope with an adjustable field of view and fast iterative Fourier filtering reconstruction," J. Opt. Soc. Am. A 40, 942-954 (2023)
[80] J. H. Leach, S. R. Chinn, L. Goldberg, "Monostatic all-fiber scanning LADAR system," Appl. Opt. 54, 9752-9757 (2015)
[81] M. H. H. Mokhtar, R. R. A. Syms, "Resonant fiber scanner with optical feedback," Opt. Express 22, 25629-25634 (2014)
[82] Y. S. Leong, M. T. Bahari, M. H. H. Mokhtar, "Optical fibre positioning and resonant frequency adjustment using intermittent optical feedback for pre-imaging calibration," Sens. Actuators A 379, 115967 (2024)
[83] J. J. Flokentin, “Partial observability and optimal control,” J. Electron. Control 13(3), 263-279 (1962)

[84] F. Lin, W. M. Wonham, "Supervisory control of timed discrete-event systems under partial observation," IEEE Trans. Autom. Control vol. 40, no. 3, pp. 558-562 (1995)
[85] T. Matsuda, S. Onoe, Y. Seo, et al., “Display unit using laser scanning device,” J. Soc. Inf. Display, 26, 631-640 (2018)
[86] M. Tekpınar, R. Khayatzadeh, O. Ferhanoğlu, "Multiple-pattern generating piezoelectric fiber scanner toward endoscopic applications," Opt. Eng. 58(2) 023101 (2019)
[87] R. C. Dorf, R. H. Bishop, “Modern control systems,” Prentice Hall, New York (2011)
[88] J. P. Costas, "Synchronous communications," Proc. IRE vol. 44, no. 12, pp. 1713-1718 (1956)
[89] G. C. Hsieh, J. C. Hung, "Phase-locked loop techniques. A survey," IEEE Trans. Ind. Electron. vol. 43, no. 6, pp. 609-615 (1996)
[90] R. E. Best, N. V. Kuznetsov, G. A. Leonov, et al., “Simulation of analog Costas loop circuits,” Int. J. Autom. Comput. 11, 571-579 (2014)
[91] J. I. Brown, "A digital phase and frequency-sensitive detector," Proc. IEEE vol. 59, no. 4, pp. 717-718 (1971)
[92] R. S. Sánchez, J. R. C. Piqueira, A. M. Bueno, “Comparing phase detectors in analog phase-locked loops,” Eur. Phys. J. Spec. Top. 230, 3609-3614 (2021)
[93] R. L. Miller, "Fractional frequency generators utilizing regenerative modulation," Proc. IRE. 27, 446-457 (1939)
[94] P. K. Basu, “Digital frequency dividers,” IETE J. Educ. 22, 143-151 (1981)
[95] P. Larsson, “High-speed architecture for a programmable frequency divider and a dual modulus prescaler,” IEEE J. Solid-State Circuits 31, 744-748 (1996)
[96] M. Arora, “Clock dividers made easy,” Application Note, ST Microelectronics Ltd (2002)
[97] P. Alfke, “Unusual clock dividers,” Application Note, Xilinx (1999)
[98] J. Noordanus, "Frequency synthesizers: a survey of techniques," IEEE Trans. Commun. Tech. vol. 17, no. 2, pp. 257-271 (1969)
[99] E. H. Armstrong, "A method of reducing disturbances in radio signaling by a system of frequency modulation," Proc. IEEE, vol. 72, no. 8, pp. 1042-1062 (1984)
[100] D. Messerschmitt, "A new PLL frequency synthesis structure," IEEE Trans. Commun. vol. 26, no. 8, pp. 1195-1200 (1978)
[101] E. J. Seibel, Q. Y. J. Smithwick, “Unique features of optical scanning, single fiber endoscopy,” Lasers Surg. Med. 30: 177-183 (2002)
[102] C. L. Zavaleta, E. Garai, J. T. C. Liu, et al., “A Raman-based endoscopic strategy for multiplexed molecular imaging,” Proc. Natl. Acad. Sci. U.S.A. 110 (25) E2288-E2297 (2013)
[103] C. M. Lee, J. E. Chandler, E. J. Seibel, "Wide field fluorescence imaging in narrow passageways using scanning fiber endoscope technology," Proc. SPIE 7558, Endoscopic Microscopy V, 755806 (2010)
[104] F. Helmchen, M. S. Fee, D. W. Tank, et al., “A miniature head-mounted two-photon microscope: high-resolution brain imaging in freely moving animals,” Neuron 31(6), 903-912 (2001)

[105] I. Gusachenko, M. Chen, K. Dholakia, "Raman imaging through a single multimode fibre," Opt. Express 25, 13782-13798 (2017)
[106] M. T. Myaing, D. J. MacDonald, X. Li, "Fiber-optic scanning two-photon fluorescence endoscope," Opt. Lett. 31, 1076-1078 (2006)
[107] L. Scolaro, D. Lorenser, W. J. Madore, et al., "Molecular imaging needles: dual-modality optical coherence tomography and fluorescence imaging of labeled antibodies deep in tissue," Biomed. Opt. Express 6, 1767-1781 (2015)
[108] E. J. Seibel, R. S. Johnston, C. D. Melville, "A full-color scanning fiber endoscope," Proc. SPIE 6083, 608303 (2006)
[109] E. J. Seibel, "1-mm catheterscope," Proc. SPIE 6852, 685207 (2008)
[110] Y. S. Leong, M. H. H. Mokhtar, M. S. D. Zan, et al., "Enhancement of in vitro cellular structure morphology imaging using multiwavelength confocal endoscopic scanner," Alexandria Eng. J. 97, 14-24 (2024)
[111] F. Légaré, C. L. Evans, F. Ganikhanov, et al., "Towards CARS Endoscopy," Opt. Express 14, 4427-4432 (2006)
[112] E. P. Severin, H. Bae, K. Reichwald, et al., "Multimodal nonlinear endomicroscopic imaging probe using a double-core double-clad fiber and focus-combining micro-optical concept," Light Sci. Appl. 10, 207 (2021)
[113] R. R. A. Syms, J. Cozens, "Optical guided waves and devices," McGraw-Hill, New York (1992)
[114] K. C. Kao, G. A. Hockham, "Dielectric-fibre surface waveguides for optical frequencies," Proc. Inst. Electr. Eng. vol. 113, no. 7. (1966)
[115] Y. S. Leong, M. H. H. Mokhtar, N. A. A. Nazri, et al., "Discriminative spatial localisation in confocal reflectance and carbon dots-based fluorescence imaging using mixed-mode endoscopic scanner," Int. J. Optomechatronics 18(1) 2347292 (2024)
[116] Y. S. Leong, N. A. B. Kebehi, M. H. H. Mokhtar, et al., "Multichannel confocal microscopy using mixed-mode fiber pair for cellular-resolution imaging," IEEE Photonics Technol. Lett. vol. 36, no. 18, pp. 1153-1156 (2024)
[117] P. M. Delaney, M. R. Harris, R. G. King, "Fiber-optic laser scanning confocal microscope suitable for fluorescence imaging," Appl. Opt. 33, 573-577 (1994)
[118] D. Bird, M. Gu, "Fibre-optic two-photon scanning fluorescence microscopy," J. Microsc. 208, 35-48 (2002)
[119] S. P. Tai, M. C. Chan, T. H. Tsai, et al., "Two-photon fluorescence microscope with a hollow-core photonic crystal fiber," Opt. Express 12, 6122-6128 (2004)
[120] A. Lombardini, V. Mytskaniuk, S. Sivankutty, et al., "High-resolution multimodal flexible coherent Raman endoscope," Light Sci. Appl. 7, 10 (2018)
[121] L. Fu, X. Gan, M. Gu, "Nonlinear optical microscopy based on double-clad photonic crystal fibers," Opt. Express 13, 5528-5534 (2005)
[122] C. J. Engelbrecht, R. S. Johnston, E. J. Seibel, et al., "Ultra-compact fiber-optic two-photon microscope for functional fluorescence imaging in vivo," Opt. Express 16, 5556-5564 (2008)
[123] J. C. Knight, T. A. Birks, P. S. J. Russell, et al., "All-silica single-mode optical fiber with photonic crystal cladding," Opt. Lett. 21, 1547-1549 (1996)

[124] T. A. Birks, J. C. Knight, P. S. J. Russell, "Endlessly single-mode photonic crystal fiber," Opt. Lett. 22, 961-963 (1997)
[125] J. C. Knight, T. A. Birks, P. S. J. Russell, et al., "Properties of photonic crystal fiber and the effective index model," J. Opt. Soc. Am. A 15, 748-752 (1998)
[126] J. C. Knight, J. Arriaga, T. A. Birks, et al., "Anomalous dispersion in photonic crystal fiber," IEEE Photonics Technol. Lett. vol. 12, no. 7, pp. 807-809 (2000)
[127] J. C. Knight, J. Broeng, T. A. Birks, et al., "Photonic band gap guidance in optical fibers," Science 282, 1476-1478 (1998)
[128] R. F. Cregan, B. J. Mangan, J. C. Knight, et al., "Single-mode photonic band gap guidance of light in air," Science 285, 1537-1539 (1999)
[129] T. Zentgraf, "Imaging the rainbow," Nat. Nanotechnol. 13, 179-180 (2018)
[130] M. Lakshmanan, D. Senthilkumar, "Linear stability and bifurcation analysis. In: Dynamics of nonlinear time-delay systems," Springer, Berlin (2011)
[131] K. Manal, W. Rose, "A general solution for the time delay introduced by a low-pass Butterworth digital filter: An application to musculoskeletal modeling," J. Biomech. 40(3), 678-681 (2007)
[132] B. Delaunay, "Sur la sphere vide. A la mémoire de Georges Voronoï," Bulletin de l'Académie des Sciences de l'URSS. Classe des Sciences Mathématiques et Naturelles 6, 793-800 (1934)
[133] S. Lertrattanapanich, N. K. Bose, "High resolution image formation from low resolution frames using Delaunay triangulation," IEEE Trans. Image Process. vol. 11, no. 12, pp. 1427-1441 (2002)
[134] W. Erb, C. Kaethner, M. Ahlborg, et al., "Bivariate Lagrange interpolation at the node points of non-degenerate Lissajous curves," Numer. Math. 133, 685-705 (2016)
[135] E. O. Muñiz, "A method for deriving various formulas in electrostatics and electromagnetism using Lagrange's trigonometric identities," Am. J. Phys. 21(2): 140-141 (1953)
[136] T. Cvetic, Z. Vucinic, "Fluorescent properties of spinach leaf plasma membranes and chloroplast envelopes," Ann. N. Y. Acad. Sci. 1048, 509-512 (2005)
[137] L. Donaldson, "Softwood and hardwood lignin fluorescence spectra of wood cell walls in different mounting media," IAWA Journal, 34(1), 3-19 (2013)
[138] L. Donaldson, "Autofluorescence in plants," Molecules 25(10), 2393 (2020)
[139] E. H. Moore, "On the reciprocal of the general algebraic matrix," Bull. AMS 26, 394-395 (1920)
[140] R. Penrose, "A generalized inverse for matrices," Math. Proc. Cambridge Philos. Soc. vol. 51, no. 3, pp. 406-413 (1955)
[141] I. Yilmaz, I. O. Bildirici, M. Yakar, et al., "Color calibration of scanners using polynomial transformation," XXth ISPRS Congress Commission V, Istanbul, Turkey, 12-23 July (2004)
[142] H. Jin, J. Lim, Y. Kim, et al., "Optical design of a reflecting telescope for CubeSat," J. Opt. Soc. Korea 17, 533-537 (2013)
[143] D. Kaur, A. M. d. Souza, J. Wanna, et al., "Multipass cell for molecular beam absorption spectroscopy," Appl. Opt. 29, 119-124 (1990)